ABSTRACT

Title of dissertation: DISTRIBUTED SENSING FOR FLEXIBLE

STRUCTURES USING A FIBER OPTIC SENSOR

SYSTEM

Christopher S. Baldwin, Doctor of Philosophy, 2003

Dissertation directed by: Assistant Professor Steven Buckley

Department of Mechanical Engineering

In this dissertation, a framework is developed and demonstrated for the use of a

new shape measurement system consisting of fiber Bragg grating (FBG) based strain

sensors, a shape determination algorithm based on Frenet frames, and a signal

processing algorithm based on modal analysis techniques. The system is

experimentally validated by using a long slender, aluminum cantilever structure

(65.625″×2.0″×0.125″) with eight serially multiplexed FBG sensors. The multiplexed

FBG sensors measure the bending strain distribution along the cantilever structure, and

this distribution is used to calculate the dynamic shape of the structure forced by a base

excitation. The structural shape data is processed by using modal analysis techniques to

determine the modal coefficients and the associated spatial modes that best represent the structure's vibration. The results obtained for the modal coefficients are found to compare well with results of Fourier transform analysis of signals recorded over time. Analysis by using the shape algorithm developed herein demonstrates the effectiveness of using a Frenet frame-based technique to determine the shape of the structure from recorded strain data. Sources of error due to factors such as the number of sensors and Taylor series approximation in the shape algorithm are examined.

The methodology discussed in this dissertation allows both static and dynamic monitoring of structural shape characteristics. This type of real-time analysis may be useful for applications in structural health monitoring where changes in the modal coefficients may lead to indications of damage to the structure and in applications such as sonar arrays and aircraft wings where knowledge of a structure's shape can yield improved results.

DISTRIBUTED SENSING FOR FLEXIBLE STRUCTURES

USING A FIBER OPTIC SENSOR SYSTEM

by

Christopher S. Baldwin

Dissertation submitted to the Faculty of the Graduate School of the
University of Maryland, College Park in partial fulfillment
of the requirements for the degree of
Doctor of Philosophy
2003

Advisory Committee:

Assistant Professor	Steven Buckley, Chairman/Advisor
Professor	Balakumar Balachandran, Co-Advisor
Assistant Professor	Hugh Bruck
Assistant Professor	Donald Robbins, Jr.
Associate Professor	Darryll Pines, Dean's Representative

DEDICATION

To:

My wife Tami and my son Jake Andrew Baldwin born during the writing of my

dissertation

ACKNOWLEDGEMENTS

I would like to acknowledge the guidance and support of my dissertation committee members, as well as all the people that have supported my research efforts at the University of Maryland. I would also like to acknowledge the loving support of my parents, Glenn and Julie Baldwin. Finally, I wish to thank my wife, Tami, for her encouragement, love, and understanding during the long evenings and weekends when much of this work was accomplished.

TABLE OF CONTENTS

LIST OF FIGURES

xi

LIST OF TABLES

LIST OF SYMBOLS

Λ	Pitch of FBG
n_{core}	Refractive index of optical fiber core
n_{eff}	Refractive index of FBG sensor
β	Optical propagation value
k_w	Wavenumber
λ	Wavelength
λ_B	Bragg wavelength
p_{ij}	Strain-optic tensor
ε	Strain
ν	Poisson's Ratio
M	Number of optical fiber channels
N	Number of sensors per channel
$\bar{x}$	Centroid of sensor spot
I_i	Intensity of pixel number i
K_{ce}	Centroid to strain coefficient
$y(x,t)$	Deflection of cantilever beam
$\phi(x)$	Mode shape
$q(t)$	Time component of beam response
E	Modulus of elasticity
I	Moment of inertia
γ	Mass per unit length

ω	Angular frequency
R	Position vector
κ	Curvature
ρ	Radius of curvature
h	Thickness of beam
T	Tangent vector
N	Normal vector
B	Binormal vector
y_{exp}	Experimentally determined shape
y_{theory}	Theoretically determined shape
n	Number of segments used for error calculation
r_p	Pearson coefficient
A_r	Modal coefficient for mode r
H	Mode shape matrix
A	Vector of A_r values
Y	Vector of deflection values

1 Introduction

In this dissertation, the development of a fiber optic sensor system is discussed for performing distributed sensing of strain along flexible structures. The distributed strain measurements are incorporated into a modal analysis algorithm to describe the dynamic response of the structure. The ability to determine the dynamic modal response of a structure by using distributed strain measurements represents an improvement over the use of a Fourier transform to determine the time averaged frequency response of the system. The Fourier transform method provides a measure of the vibration component frequencies in a structure's motion. The modal analysis algorithm discussed in this dissertation provides a means for determining the modal coefficients and the associated spatial modes in the structures response at any given time during the structure's motion. Variations in these modal coefficients can be observed as a function of time to monitor changes in the structure's dynamics. This new algorithm makes use of a fiber optic monitoring system, a signal processing component for the measured sensor data, and the application of modal analysis techniques to determine the vibration characteristics of the structure.

The fiber optic sensor system makes use of serially multiplexed fiber Bragg grating (FBG) sensors to achieve multiple discrete strain measurements along the structure whose dimensions are much larger then the gage length of the FBG sensor. The measurements are discrete in the sense that the fiber optic sensor has a gage length of approximately 1 cm instead of a longer gage length typical of a distributed sensor scheme, such as a Michelson or a Mach-Zehnder interferometer. Once the distributed strain data is obtained, the dynamic structural shape can be determined through the use of Serret-Frenet formulae. The scope of this work involves monitoring the strain along a structure, determining the deflection of the structure based on the measured strain data and mechanics models, and determining the dynamic response of the structure based on modal analysis techniques.

The flexible structure investigated in this research effort is an isotropic cantilever beam, since the cantilever beam model provides a well-understood response that can be used to evaluate and validate the shape measurement system. Strain is measured from the FBG sensors by using the University of Maryland patented Digital Spatial Wavelength Domain Multiplexing (DSWDM) technology [Chen and Hu, 2002; Baldwin, Chen, Kiddy, Niemczuk, Christiansen, Vaithyanathan, and Chen, 2001a; Christensen, Chen, Baldwin, Niemczuk, Kiddy, Chen, Kopola, Aikio, Suopajarvi, and Buckley, 2001]. This technology allows for multiple FBG sensors to be demodulated simultaneously at a sampling rate of 2 kHz. The measured strain data along the length of the beam is converted to curvature by using mechanics. Distributed values for curvature are calculated through interpolation of the sensor-derived values, and these

2

curvature values are then used to determine the deflection of the structure. The first few mode shapes of a periodically forced cantilever beam are investigated experimentally and analytically. Experimental and simulated results are compared with the theoretical predictions for cantilever beam deflection based on known mode shapes. Modal analysis techniques are then used to determine the modal coefficients associated with the dynamic response of the experimental structure. The proposed system can be used to determine not only the shape (or deflection) of the structure, but can also potentially used to monitor the structure for damage or other structural characteristics [Pandey, Biswas, and Samman, 1991].

1.1 Motivation

The determination of a structure's shape is important for structural functionality in many fields. This is particularly true in fields where structures are acted upon by periodic forces imparting a modal response to the structure. For example, the functionality of helicopter blades is based on a twisting motion of the blades during forward flight [Bramwell, 1986]. The twist prevents an unbalanced lift condition between the forward moving and retreating blades. Fixed wing aircraft is another aerospace application where the shape of the structure is important [Austin, Rossi, Nostrad, Knowles, and Jameson, 1994]. For these applications, the shape of the wing determines the amount of lift provided to the aircraft. Efforts are underway to develop new smart structures (morphing wings) to provide more lift from a fixed wing while reducing the amount of drag created by the structure [Reich and Sanders, 2003]. These

two examples illustrate potential benefits from technologies that determine structural shape for applications that involve fluid flow over a structural surface.

Another application that would benefit from a shape sensing system is active structural acoustics control. In these applications, the surface of a structure can be dynamically altered in a manner to reduce, or cancel out, various components of the transmitted acoustic signal. The modulation of the structure's surface is determined via a feed-forward control system that has inputs from surface mounted strain sensors and/or microphones. Experimentation involving the use of piezoceramic actuators actuating a plate has been shown to significantly affect the noise transfer into an enclosure [Sampath and Balachandran, 1997; Balachandran, Sampath and Park, 1996]. Including the use of the shape measurement system would provide a measurement of distributed strain or deflection of the surface as input to the control system instead of a limited number of discrete strain inputs.

A further field of interest is towed sonar arrays; knowledge of the exact position (and orientation) of the sonar array is required for accurate interpretation of the results from the hydrophone sensors [Nikitakkos, Leros, and Katsikas, 1998; Smith, Leung, and Cantoni, 1996; Wahl, 1993]. By determining the shape of the array with respect to a known reference point, a more accurate determination of object location is available from the sonar array data. These types of sonar arrays are employed in various applications from Navy applications to oil exploration vessels. As the towed sonar array travels through water, motions of the towing vessel (bobbing and swaying due to

surface waves) are transmitted down the tow cable to the array module. This motion induces a vibration that propagates down the length of the towed sonar module. Vibration can also be imparted to the towed sonar module via underwater currents [Gray, Anderson, and Bitmead, 1993]. These excitations can be considered periodic within a given time period, and the resulting vibrations of the flexible structure have a periodic structure.

1.2 Fiber Optic Strain and Shape Sensing Background

In recent years, there has been substantial progress in using fiber optic sensors to detect structural health and performance [Othonos and Kyriacos, 1999; Measures, 2001]. For example, various types of fiber optic sensors have been developed to meet application-specific requirements for sensing strain in many environments. The most popular of these types of sensors has been the FBG sensor. Researchers have used this type of sensor to monitor the structural health and load response of composite pressure vessels [Foedinger, Rea, Sirkis, Baldwin, Troll, Grande, Davis, and Vandiver, 1999], composite marine piles [Baldwin, Salter, Niemczuk, Chen, and Kiddy, 2002a; Baldwin, Poloso, Chen, Niemczuk, Kiddy, and Ealy, 2001b], Navy structures [Kiddy, Baldwin, Salter, and Chen, 2002; Baldwin, Niemczuk, Kiddy, Chen, Christiansen, and Chen, 2002b; Baldwin, et al. 2001; Wang, Havsgard, Urnes, Pran, Knudsen, Kersey, Davis, Berkoff, Dandridge, and Jones, 1997], as well as other civil and mechanical systems [Othonos and Kyriacos, 1999].

The use of FBG sensors to monitor the shape of the structure was first investigated by Davis et al, who presented results for static deflections of a cantilever beam [Davis, Kersey, Sirkis, and Frieble, 1996]. The deflections investigated corresponded to the first three mode shapes for this structure, and measurements were made by using only three multiplexed FBG sensors. The sensors were mounted to the surface of the cantilever beam, so that the second FBG sensor was at the node of the second vibrational mode and the third FBG sensor was located at a node of the third vibrational mode. The shape (deflection) of the beam determined by the sensors due to these loads was compared to the actual shape via digitized photographs. The strain levels recorded from the FBG sensors were processed by an algorithm based on the Rayleigh-Ritz theorem [Davis et al, 1996]. For shape determination, the trial beam functions were adjusted by using weighting parameters to obtain better agreement between the calculated and measured beam shapes. The FBG sensors were interrogated via a scanning fiber Fabry-Perot (FFP) filter. This technique is the precursor to the commercially available fiber Bragg grating interrogation system (FBG-IS) produced by Micron Optics Inc. [Micron, 2001]. The data from these sensors were also monitored during the periodic excitation of this beam through the first three modal frequencies. The dynamic response spectra for the FBG sensors were compared to resistance strain gage data and showed good correlation. No attempt was made to determine the dynamic shape of the structure from the recorded strain data during the vibration experiments, and only Fourier transforms of the strain data were presented in this work.

Another application of FBG sensors to determine the shape of flexible structures is in the field of towed sonar arrays [Chen and Sirkis, 2001]. This system is also based on the scanning Fabry-Perot demodulation system [Micron, 2001]. The number of FBG sensors used for this application is greatly increased over the cantilever beam test design by using four or five (for proposed temperature compensation) sensors at various locations along the length of the array. The increase in number of sensors allows the determination of bending and torsion strains to resolve a three dimensional shape of a flexible member of a towed sonar array. The shape measurement algorithm for this work is based on elasticity relationships between the bending strains and the deflection of the hose, where the three-dimensional structure is assumed to experience beam-type deflection. This work is also restricted to quasi-static deflections of the flexible structure.

Other types of fiber optic sensors can be used to measure vibration and strain of structures, such as Hill gratings [Greene, Murphy, Fogg, Claus, and Vengsarkar, 1992], polarization maintaining Panda fibers with Michelson interferometer readout [Lou, Liu, and Chen, 1997], and spatially weighted fiber optic sensors [Li, 1998]. These techniques typically filter the sensor response to one mode shape for the vibrating structure; the sensor has a unique response to one vibrational state and all others are filtered from the response. These sensors also require more complicated fabrication techniques such as formation of in-fiber gratings while mounted to the structure [Greene, et al., 1992] or optical fiber material parameter changes as a function of sensor length to match certain strain-optic conditions [Li, 1998]. Giving these types of sensors

the capability to function over multiple vibration modes would require the use of

multiple detection systems and multiple sensors each one by using a separate optical

fiber (no serial multiplexing capability). Each of the fiber optic sensors has been

demonstrated experimentally by using a cantilever beam model. There has also been

development work on fiber optic sensor based tip measurements sensors for acoustic

pressure measurements [Yu, Balachandran, 2003; Yu, 2002].

There are other methods used to determine the shape of structures besides fiber

optic sensors. For example, in the field of towed sonar arrays, current methods use

beam forming algorithms with the sonar data and known noise source locations

[Nikitakkos, et al., 1998; Smith, Leung, and Cantoni, 1996; Wahl, 1993]. This

technique can be improved through the use of various filtering and other techniques,

such as Kalman filters [Gray, etal, 1993]. Another proposed method involves using

heading and depth sensor information taken along the array length, and processing this

data as a cubic spline or quartic spline [Howard and Syck, 1992]. These formulations

do not take into account the twisting (or torsion of the structural member) of the array,

but treat the problem as essentially a beam type structure. The work presented by

Howard has been criticized for relying on external sensors from the acoustic array that

are inaccurate and unreliable [Wahl, 1993].

Other non-contact type sensors have been developed to monitor the deflection of

structural surfaces, including laser range finders and radar systems. These types of non-

contact measurements require long sampling times (on the order of 1 Hz sampling rate)

compared with the fiber optic system investigated in this dissertation, which has a sampling rate of approximately 2 kHz. Methods have been investigated to monitor structural changes by using techniques including photographs and CCD imaging [Sevenhuijsen, Sirkis, and Bremand, 1993]. To employ these techniques, the structure must have a visible grid drawn on the surface and the image changes need to be tracked via grid deformations. There must also be a direct line of sight to the structure. A similar technique involves tracking the changes of spots on the surface. These spots can be imaged on a surface via a laser and a diffraction grating. A cross grid can be used to produce diffraction peaks on the surface of the structure, and changes in the surface geometry can be monitored through changes in the locations of these peaks [Sevenhuijsen, et al., 1993].

1.3 Technical Objectives

In this research, the application of a strain-based shape measurement system for structural dynamic analysis is examined and the necessary framework for such analysis is developed. This work concentrates on modal shape sensing by using FBG sensors to measure strain due to the dynamic deformation of the structure. FBG sensors are chosen by using their inherent optical advantages and multiplexibility of these sensors. Recent advances in structural sensing with FBG sensors has allowed the development of a high-speed, highly multiplexed instrumentation system. To perform shape sensing modal analysis as investigated in this dissertation, the measurement system must have a high sampling rate for multiple sensors to interpret the spatial information in terms of an

adequate number of modes of the structure. The fiber optic sensor system must also interrogate a sufficient number of sensors to determine the shape of the highest vibration mode under consideration.

The review of the literature found previous approaches monitoring the frequency response of surface mounted FBG sensors (e.g. Davis, et al, 1996 and subsequent work). The methods employed in this research were limited in the number of sensors used and the speed of the interrogation system. The research presented in this dissertation describes a FBG interrogation system capable of a sampling rate of approximately 2 kHz for a serially multiplexed array of FBG sensors. This research discusses the development of an algorithm that translates strain information into the shape of the flexible structure. The resulting shape data is used with modal analysis techniques to determine the modal coefficients for the structural vibration as a function of time. The following contributions follow from the present dissertation work:

- Development of a fiber optic sensor system for dynamic shape sensing including DSWDM instrumentation, mechanics models, and signal processing
- Investigation of sensor spacing for the DSWDM instrumentation system
- Development of an algorithm based on Frenet frame analysis for the determination of structural shape and investigation of error sources for the Frenet frame shape algorithm

- Examination of modal analysis techniques of the experimental shape data for the vibrating cantilever beam and development of a modal analysis system that uses the experimental shape data to determine the modal coefficients as a function of time

Experimental validation of this research was conducted by using vibrations of a cantilever beam. The cantilever beam model is well-understand to generate numerical data for comparison with experimental data. The experimental setup was constructed to restrict the modal frequencies of interest to be below 200 Hz, by properly selecting the beam material properties and geometry, to allow an adequate sampling rate for the resonant frequencies.

1.4 Outline of Dissertation

In Chapter 2, the fiber optic sensor system is discussed and an overview is provided of FBG sensors including fabrication techniques used throughout the research effort, multiplexing of the sensors, and a detailed description of the DSWDM system used to interrogate the FBG sensors. Issues of FBG sensor wavelength spacing and the sensor response with respect to the DSWDM system are also discussed. In Chapter 3, the dynamics of cantilever beams (the experimental case investigated) are discussed, and the shape measurement method using Serret-Frenet frames and the measured strain data is introduced. In Chapter 4, the shape measurement method is examined through analytical models and some of the error sources associated with the method including the number of sensors used and effects of a Taylor series approximation are

investigated. The experimental setup is described in Chapter 5 along with the fiber

optic data acquired from the DSWDM system. In Chapters 6 and 7, analysis of the

recorded data and examination of the experimentally determined shapes from the

cantilever beam are presented. Comparisons of the experimental shapes to the mode

shape components are carried out in Chapter 6. Analysis of the fast Fourier transforms

of the strain data illustrates influences from neighboring modal components. Modal

analysis techniques are employed in Chapter 7 to determine the modal coefficients for

the response of the cantilever structure. These techniques demonstrate the ability for

determining the modal characteristics of the cantilever structure at any particular time or

as a function of time.

2　Fiber Bragg Grating Sensors

Fiber Bragg grating (FBG) sensors constitute the distributed sensory components of the mode shape monitoring method investigated in this dissertation. FBGs have become an integral part of the telecommunications hardware, used in applications such as add/drop filters, fiber lasers, and data multiplexing [Kashyap, 1999]. Since the discovery of the photosensitive effect in optical fiber [Hill, Fujii, Johnson, and Kawasaki, 1979], by which UV light can be used to induce a permanent change in the refractive index of optical fiber, researchers have been discovering new applications for this unique optical phenomena. Because of the widespread use and development of this technology, several textbooks dedicated to FBGs and their applications have recently been published [Othonos and Kyriacos, 1999; Kashyap, 1999; and Measures, 2001]. In particular, Kashyap [1999] deals mainly with the telecommunications applications of FBGs, while Othonos and Kyriacos [1999] and Measures [2001] provide more details regarding sensing applications. The first portion of this chapter provides an overview of the relevant features of FBG sensors such as their fabrication, sensitivity to strain, and multiplexibility. The second portion of this chapter discusses the demodulation system used throughout the research investigation.

13

2.1 Fabrication Techniques

Bragg gratings are possible due to a property of optical fiber known as photosensitivity. Photosensitivity causes a potentially permanent change in the refractive index or opacity of glass induced by exposure to light [Kashyap, 1999]. In the case of Bragg grating formation, the change of the refractive index of an optical fiber is induced by exposure to intense UV radiation (typical UV wavelengths are approximately in a range from 150 nm to 248 nm). To create a periodic change in the refractive index, an interference pattern of UV radiation is typically produced such that it is focused onto the core region of the optical fiber. The refractive index of the optical fiber core changes where the intensity is brightest in the interference pattern to produce the periodic refractive index profile [Kashyap, 1999]. The length of a single period for the grating structure is called the grating pitch, Λ, as shown in Figure 2.1. The pitch of the grating is controlled during the manufacturing process, and this pitch is typically ~0.5 μm, while the amplitude of the index variation is only on the order of 0.1 to 0.01 percent of the original refractive index [Kashyap, 1999].
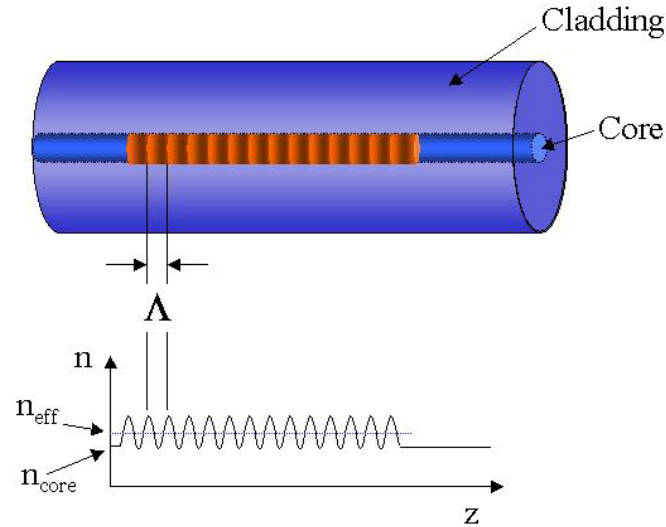
Figure 2.1: Schematic of a FBG sensor

There are many methods used to create the periodic interference pattern (e.g. phase masks [Hill, Malo, Bilodeau, Johnson, and Albert, 1993], Mach-Zehnder interferometers [Meltz, Morey, and Glenn, 1989], and Lloyd mirrors [Othonos and Kyriacos 1999]). Phase masks are corrugated silica optical components, as shown in Figure 2.2. As laser radiation passes through the phase mask, the light is divided into different diffraction beams. The diffracted beams in the example are the [+]1 and [−]1 beams, which create an interference pattern that is focused on the optical fiber core. Other orders of diffraction are designed to be minimized in these passive optical devices. The interference pattern induces a periodic refractive index change along the exposed length of the optical fiber, thus creating the Bragg grating.
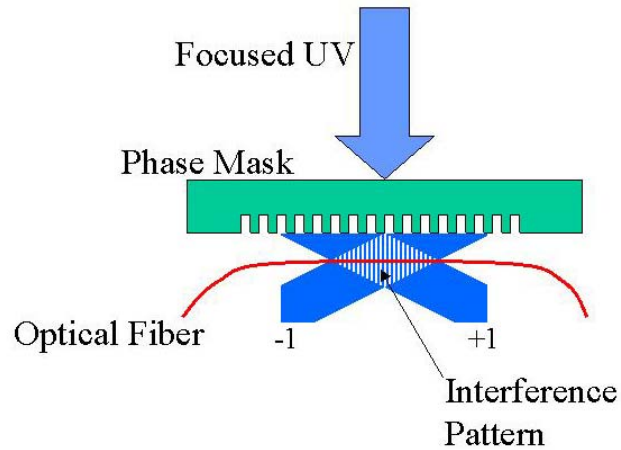
Figure 2.2: Phase mask fabrication technique

The Mach-Zehnder interferometer technique uses a Mach-Zehnder interferometer to create an interference pattern on the optical fiber. The optical arrangement for the Mach-Zehnder technique is shown in Figure 2.3. Light from the laser emission is passed through focusing optics, and it is split via an optical beam splitter. The two divergent laser beams are redirected via mirrors to combine at the optical fiber location resulting in an interference pattern from the combination of these two laser beams. The focusing optics are designed to focus the laser energy at the optical fiber location.
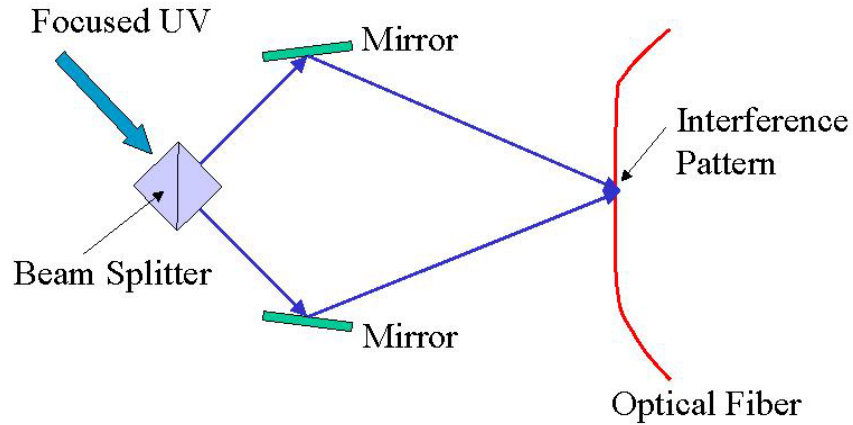
Figure 2.3: Mach-Zehnder interferometer technique

The Lloyd mirror technique used to fabricate the sensors in this research, uses a Lloyd mirror to create an interference pattern on the optical fiber, as shown in Figure 2.4. Light from the laser emission is passed through focusing optics, and it is transmitted to the Lloyd mirror arrangement. The Lloyd mirror causes the input laser beam to be split into two beams. These beams are recombined and focused at the optical fiber location, which creates an interference pattern and forms the FBG.
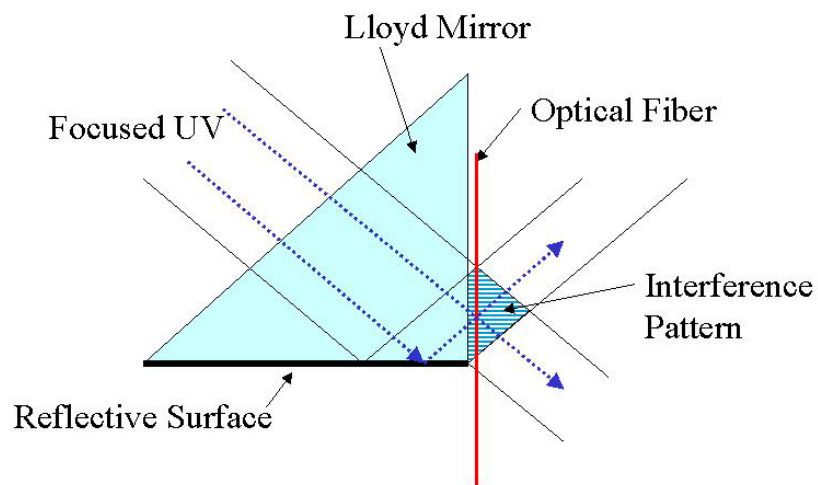
Figure 2.4: Lloyd mirror technique

2.2 Fiber Bragg Grating Optical Response

Light traveling in an optical fiber can be classified by an optical modal parameter β, given by [Snyder and Love, 1983]

$$\beta = nk_w = \frac{2\pi n_{core}}{\lambda},\qquad(2.1)$$

where n_{core} is the refractive index of the core of the optical fiber and k_w is the wavenumber associated with the wavelength of light propagating in the optical fiber. The function of the Bragg grating is to transfer a forward propagating mode (β_1) into a backward propagating mode ($-\beta_1$) (i.e., reflect the light) for a particular wavelength meeting the phase matching criterion. The phase matching condition, given by Equation 2.2, provides a means for determining which propagation modes (β_1 and β_2) are affected by the Bragg grating pitch [Hill, et al., 1993]:

$$\beta_1 - \beta_2 = \frac{2\pi}{\Lambda}.\qquad(2.2)$$

If the backward propagating mode ($-\beta_1$) is substituted into Equation 2.2 for β_2, then the following equation can be derived:

$$\beta_1 = \frac{\pi}{\Lambda} = \frac{2\pi n_{eff}}{\lambda}.\qquad(2.3)$$

The index of refraction is now noted as an effective (or average) refractive index, n_{eff}, for the Bragg grating, due to the periodic change across the length of the optical fiber. Solving Equation 2.3 for the wavelength (λ) provides the Bragg wavelength equation:

$$\lambda_B = 2 n_{eff} \Lambda\qquad(2.4)$$

where the subscript 'B' defines the wavelength as the Bragg wavelength. Equation 2.4
states that for a given pitch (Λ) and average refractive index (n_{eff}), the wavelength λ_B
will be reflected from the Bragg grating, as illustrated in Figure 2.5.
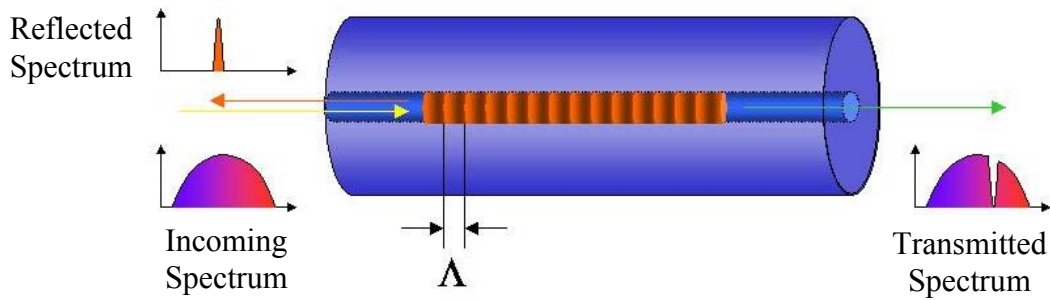
Figure 2.5: Schematic of FBG sensor with reflected and transmitted spectra

2.3 Strain Sensing using FBG Sensors

Bragg gratings operate as wavelength selective filters reflecting the Bragg
wavelength, λ_B, which is related to the grating pitch, Λ, and the mean refractive index
of the core, n_{eff}, given by Equation 2.4. Both the effective refractive index (n_{eff}) of the
core and the grating pitch (Λ) vary with changes in strain (ε) and temperature (ΔT), so
that the Bragg wavelength shifts to higher or lower wavelengths in response to applied
thermal-mechanical fields. For most applications, the shift in the Bragg wavelength is
considered a linear function of the thermal-mechanical load. The treatment of FBG
sensors here will ignore the thermal effects, because the thermal effects can be modeled
as an independent response of the Bragg grating. Birefrigent changes in the refractive
index of the optical fiber are also ignored because these changes result from diametric

19

loading on the optical fiber which is not considered in this dissertation. The shift in the

Bragg wavelength due to an incremental change of length (ΔL) is given by [Melle, Liu,

and Measures, 1992]:

$$\Delta\lambda_B = 2\left(\Lambda\frac{\partial n_{eff}}{\partial L} + n_{eff}\frac{\partial\Lambda}{\partial L}\right)\Delta L \tag{2.5}$$

Assuming the strain field is uniform across the Bragg grating length (L), then the term

$\dfrac{\partial\Lambda}{\partial L}$ can be replaced with $\dfrac{\Lambda}{L}$. Likewise, the term $\dfrac{\partial n_{eff}}{\partial L}$ can be replaced by $\dfrac{\Delta n_{eff}}{\Delta L}$ in

Equation 2.5. The terms Λ and L are physical quantities that are determined by the

interference pattern formed during fabrication and are known. The change in the

effective refractive index (Δn_{eff}) can be related to the optical indicatrix, $\Delta\left[\dfrac{1}{n_{eff}^2}\right]$, as

[Haaslach and Sirkis, 1990; Melle, et al., 1992]

$$\Delta n_{eff} = -\frac{n_{eff}^3}{2}\left(\Delta\left[\frac{1}{n_{eff}^2}\right]\right) \tag{2.6}$$

In the case of small strain, the optical indicatrix is related to the strain on the optical

fiber as:

$$\Delta\left[\frac{1}{n_{eff}^2}\right]_i = p_{ij}\varepsilon_j \tag{2.7}$$

where p_{ij} is the strain-optic tensor of the optical fiber and ε_j is the contracted strain

tensor. The directions associated with the indices shown in Equation 2.7 are illustrated

in Figure 2.6. In the general case, the strain-optic tensor will have 9 distinct elements,

termed photoelastic constants.
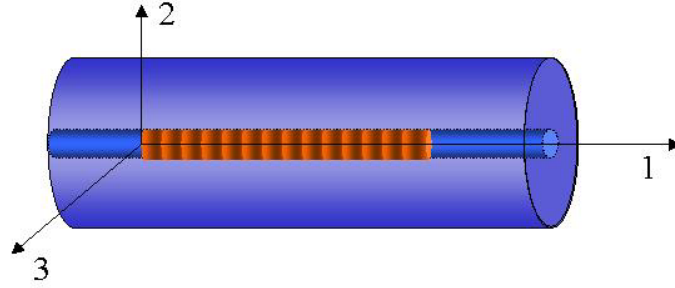
Figure 2.6: Indicial directions for optical fiber

Fortunately, for a homogenous, isotropic material (such as optical fiber), the strain-optic tensor can be represented by two photoelastic constants p_{11} and p_{12} as [Haaslach and Sirkis, 1990]

$$p_{ij} = \begin{bmatrix} p_{11} & p_{12} & p_{12} \\ p_{12} & p_{11} & p_{12} \\ p_{12} & p_{12} & p_{11} \end{bmatrix} \tag{2.8}$$

For the case of a surface mounted FBG sensor, it has been shown that the contracted strain tensor may be written as [Udd, 1995]:

$$\varepsilon_j = \begin{bmatrix} 1 \\ -v \\ -v \end{bmatrix} \varepsilon_z \tag{2.9}$$

where v is Poisson's ratio for the optical fiber. Incorporating the strain tensor into Equation 2.7 leads to the following expression for a surface mounted optical fiber sensor.

$$\Delta \left[\frac{1}{n_{eff}^2} \right] = \varepsilon_z \left[p_{12} - v(p_{11} + p_{12}) \right] \tag{2.10}$$

After substituting the Equations 2.6 and 2.10 into Equation 2.5, the result is

21

$$\Delta\lambda_B = -2\Lambda\frac{n_{eff}^3}{2}\varepsilon_z\left[p_{12} - v(p_{11} + p_{12})\right] + 2n_{eff}\Lambda\varepsilon_z \tag{2.11}$$

Normalizing Equation 2.11 by the Bragg wavelength demonstrates the dependence on the wavelength shift of the FBG sensor on the refractive index, strain-optic coefficients, and Poisson's ratio for the optical fiber.

$$\frac{\Delta\lambda_B}{\lambda_B} = \left(1 - \frac{n_{eff}^2}{2}\left[p_{12} - v(p_{11} + p_{12})\right]\right)\varepsilon_z \tag{2.12}$$

The terms multiplying the strain in Equation 2.12 are constant over the strain range of the Bragg grating, and Equation 2.12 is often written in simplified form as

$$\frac{\Delta\lambda_B}{\lambda_B} = P_e\varepsilon \tag{2.13}$$

2.4 Multiplexing

Multiplexing is one of the most critical advantages offered by Bragg grating sensor technology. There are two basic methods for multiplexing FBG sensors, termed serial multiplexing and spatial multiplexing. Serial multiplexing involves using the wavelength selectivity of FBG sensors to multiplex many FBG sensors within a given wavelength space following the illumination with broadband or white light. Spatial multiplexing involves using an optical switch or other means to interrogate multiple sensing channels, and each channel can contain multiple serially multiplexed FBG sensors along the optical fiber, again illuminated with broadband or white light. A third, recently developed method involves using a rapidly swept laser source with low-

reflectivity FBG sensors in conjunction with Fourier transforms to resolve the

contribution of multiple FBG sensors with the same Bragg wavelength [Sivanesan,

2002]. The research effort discussed in this dissertation only utilizes serial

multiplexing, and therefore spatial multiplexing is not discussed.

As shown in Figure 2.7, serial multiplexing is accomplished by producing an

optical fiber with a sequence of physically separated Bragg gratings, each with different

grating pitches, Λ_i, $i = 1,\ 2,\ 3,...,$ n. The output of the multiplexed sensors is processed

through wavelength selective instrumentation, such as a scanning optical bandpass filter

[Micron, 2001] or a dispersive device. In this case, the reflected spectrum contains a

series of peaks, each associated with a different Bragg wavelength given by $\lambda_{Bi} = 2n\Lambda_i$,

where λ_{Bi} and Λ_i are the Bragg wavelength and pitch of the ith grating, respectively. For

example, the measurement field at grating 2 in Figure 2.7 is uniquely encoded as a

perturbation of the corresponding Bragg wavelength, λ_{B2}. Note that this multiplexing

scheme is completely based on the optical wavelength of the Bragg grating sensors, not

the intensity of the signal response or bandwidth of the reflected signal.
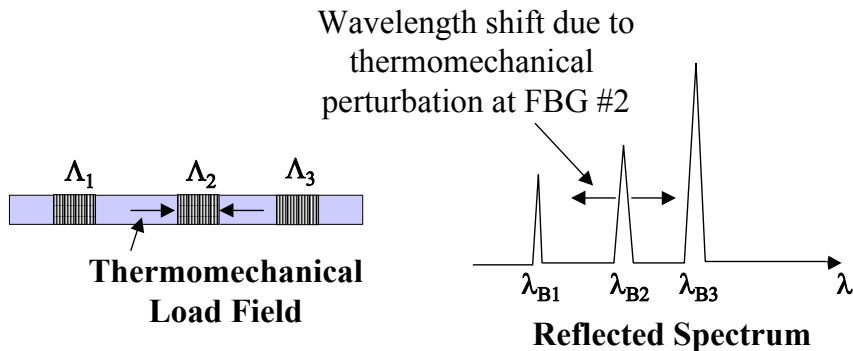
Figure 2.7: FBG sensor serial multiplexing
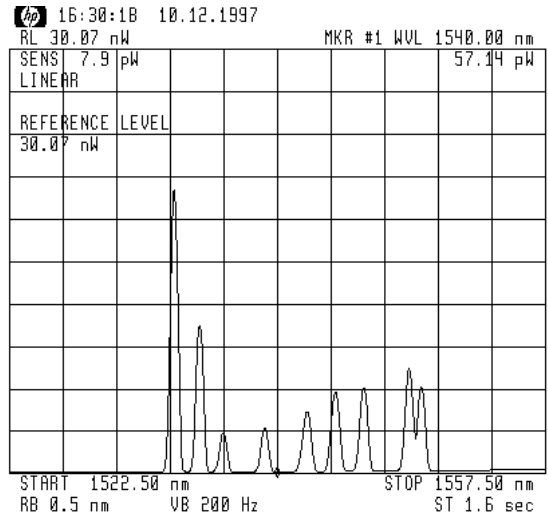
Figure 2.8: FBG reflected sensor data from nine serially multiplexed sensors

Figure 2.8 presents representative experimental data for nine serially

multiplexed FBG sensors as shown on an optical spectrum analyzer output, where the x

axis represents wavelength and the y axis represents optical intensity. Nine discrete

wavelength peaks are shown representing the nine sensors. For this research effort,

serial multiplexing technology was used to obtain multiple strain readings along the

length of a cantilever beam structure by using a single array of FBG sensors.

The number of FBG sensors that can be serially multiplexed in this manner is

limited by the optical bandwidth of the broadband source, the optical bandwidth of the

interrogation instrument, and the expected thermomechanical response of the FBG

sensors. For example, if the optical source has a bandwidth of 40 nm, then only FBG

sensors with Bragg wavelengths within this 40 nm region can be interrogated. The

maximum number of FBG sensors that can be used within this region further depends

on the operational wavelength range for each sensor (the expected measured strain for

each sensor). If the expected strain range for each sensor were ±500 με for example,

then this would correspond to approximately 1 nm of wavelength space for FBG

sensors in the 800 nm range. In order to prevent signal overlap, at least 0.5 nm of

wavelength space should be reserved between each sensor, as demonstrated in Figure

2.9. Based on the above analysis, 26 FBG sensors could be interrogated serially within

the hypothetical 40 nm wavelength range. A similar discussion regarding the spacing of

the FBG sensors used in the experimental portion of the research is given in Section 2.6.
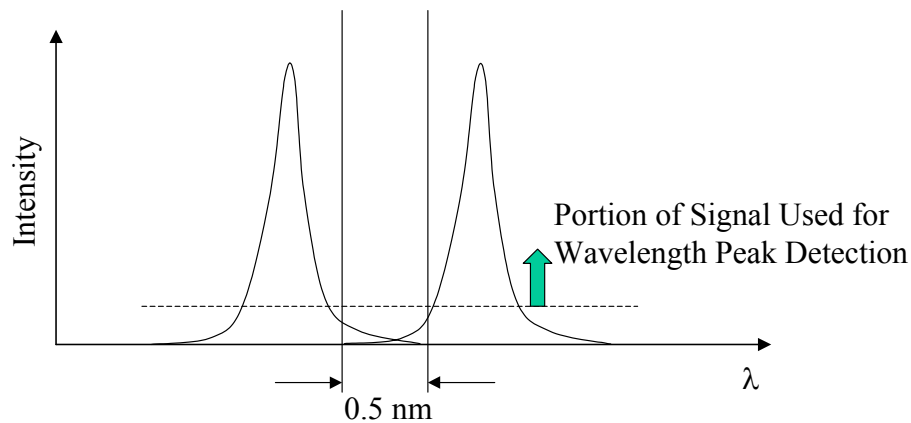
Figure 2.9: Separation of two FBG sensor signals to prevent signal overlap

2.5 Digital Spatial Wavelength Domain Multiplexing (DSWDM) System

The research presented in this dissertation focuses on the use of multiplexed

fiber Bragg gratings (FBG) as strain sensors. Due to developments over the past decade

in the telecommunications market, the availability of commercial fiber Bragg grating

components has exploded. Unfortunately, most of these devices deal with a static

Bragg grating spectra; that is environmentally isolated fiber Bragg gratings. For FBG

sensors, two commercially available systems exist for monitoring the shifting

wavelength response for sensing applications. One system, marketed by Blue Road

Research, is based on the use of ratiometric demodulation [Melle, Liu, and Measures,

1993; Baldwin, 1996; Blue Road, 2001]. This system functions by passing the reflected

Bragg grating signal through a linear optical filter, such as a wavelength division

multiplexer (WDM) [Melle, et al., 1993], a long period grating [Baldwin, 1996], or a

chirped Bragg grating [Blue Road, 2001]. The linear optical filter converts the Bragg

wavelength shift induced by applied strain into a linear variation of the optical intensity.

The ratiometric system suffers from requiring a separate linear filter for each fiber

Bragg grating sensor, thus leading to a large, expensive system for highly multiplexed

sensor systems. Micron Optics, Inc. produces the second commercially available

system. This system uses a dithered scanning in-line Fabry-Perot filter to demodulate

serially multiplexed FBG sensors [Davis, et al., 1996; Micron, 2001]. This system

allows a greater number of FBG sensors to be demodulated compared with ratiometric

demodulation system, because of the ability to demodulate serially multiplexed sensors

with one instrument. The system involves the use of piezoelectric actuated components

(scanning filter) that can suffer from failure due to the constant motion of these active

components. The maximum sampling rate of this instrument is also limited to

approximately 100 Hz because of the scanning rate of the active filter element.

The demodulation system used for this research is the Digital Spatial

Wavelength Domain Multiplexing (DSWDM) system recently developed at the

26

University of Maryland [Christiansen, et al., 2001; Baldwin, et al., 2001a, Baldwin, et al., 2002b]. This system is capable of high-speed (up to 2 kHz) demodulation of serially and spatially multiplexed FBG sensors. The ability to demodulate hundreds of FBG sensors makes this system attractive for large scale structural sensing applications. The DSWDM functions by splitting the reflected FBG spectrum through the use of a Prism-Grating-Prism (PGP) onto the surface of a Complementary Metal Oxide Semiconductor (CMOS) imager. A unique feature of this technology is that each sensor in the system can be addressed independently. This allows the sample rate and resolution of each sensor to be changed by software reconfiguration to tailor the system to a particular application need. The variable addressability of the CMOS imager allows for data sampling rates approaching 2 kHz. In addition, the sensor interrogation instrument is compact, robust, and contains no moving parts. In short, this technique offers significant performance improvements over existing FBG sensor demodulation systems.

A schematic diagram of the sensing network is shown in Figure 2.10, where light from a broadband source is split into many single mode fibers (hereafter denoted as "fiber channels") by an optical fiber dispatch box. The dispatch box consists of multiple 3 dB fiber optic couplers arranged to provide the number of sensing channels required for the system. Along each sensing channel, multiple FBG sensors with pre-determined discrete Bragg wavelengths can be serially multiplexed as discussed in Section 2.4. FBG sensors on different sensing channels can have the same Bragg wavelength because these will be spatially multiplexed. Light reflected from the FBG

sensors in each fiber channel is coupled into a down-lead fiber via a 3 dB fiber optic

coupler arrangement of the dispatch box and sent to the two-dimensional spectrometer.
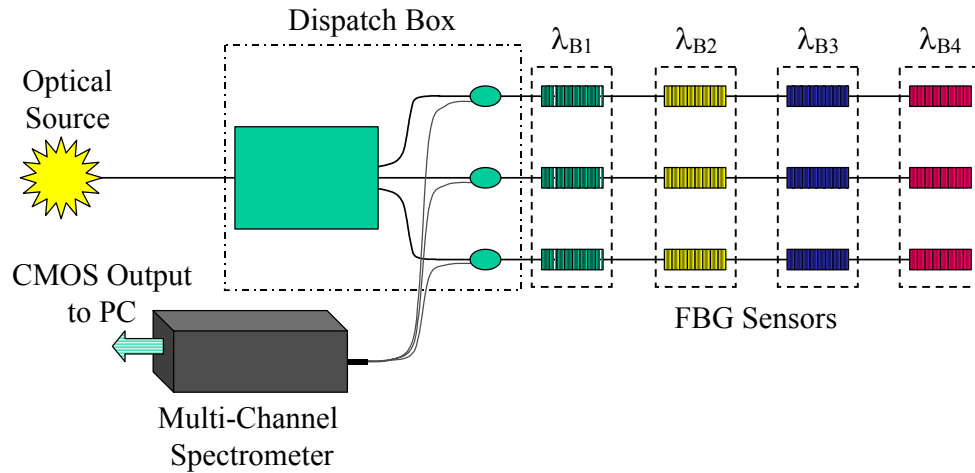
Figure 2.10: Schematic of the DSWDM optical sensing network

The spectrometer used for this research, shown schematically in Figure 2.11, is

developed by VTT (Technical Research Centre of Finland) [Aikimo, Vaarala, and

Keranen, 1997] and uses a Prism-Grating-Prism (PGP) configuration that uses

transmission lenses and a transmission grating to disperse the light. A 2-D CMOS

random access image sensor is placed at the output port of the spectrometer. The

optical fibers leading into the spectrometer are arranged in a horizontal line positioned

at the input slit. The three optical paths shown in the figure are separated in the vertical

direction to demonstrate the multi-channel functionality of the spectrometer. The

CMOS image sensor chip is positioned such that its pixel columns (Y-axis) are parallel

to the grooves of the bulk grating in the spectrometer. The digital output of the imager

is sent to a computer for signal processing.
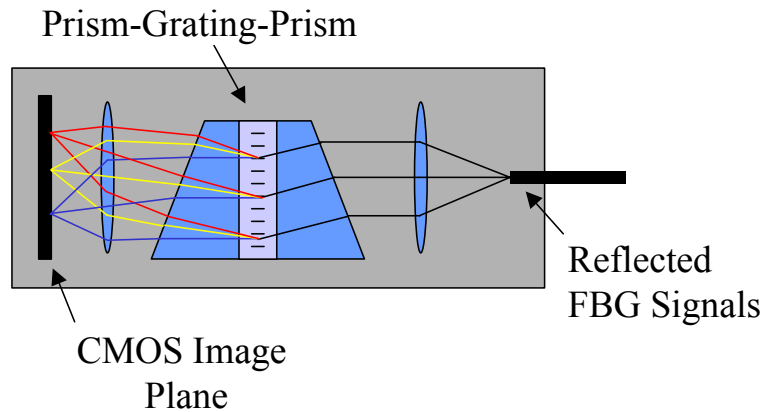
Figure 2.11: Prism-Grating-Prism (PGP) spectrometer configuration

The spectrometer imaging system separates light from different fibers and distributes the light across the 2-D image sensor. Because of the diffraction grating, the light at different wavelengths is dispersed to different positions along the X-axis, the output of each fiber forms bright spots at different positions along pixel rows of the image sensor, as shown in Figure 2.12. Therefore, if the system has M fiber channels and N FBG sensors of different wavelengths along each fiber, there will be an M × N matrix of discrete spots on the image sensor array. A column of such spots in the matrix represents FBG sensors of the same or similar wavelength in different fiber channels, while a row represents different FBG sensors along the same fiber. In other words, for each FBG, the spatial position of its fiber channel is encoded into the position along the Y-axis of the imager while its wavelength is encoded along the X-axis. The precise central wavelength of a FBG sensing node is detected by locating the centroid of the associated spot along the X-axis of the imager pixel array.
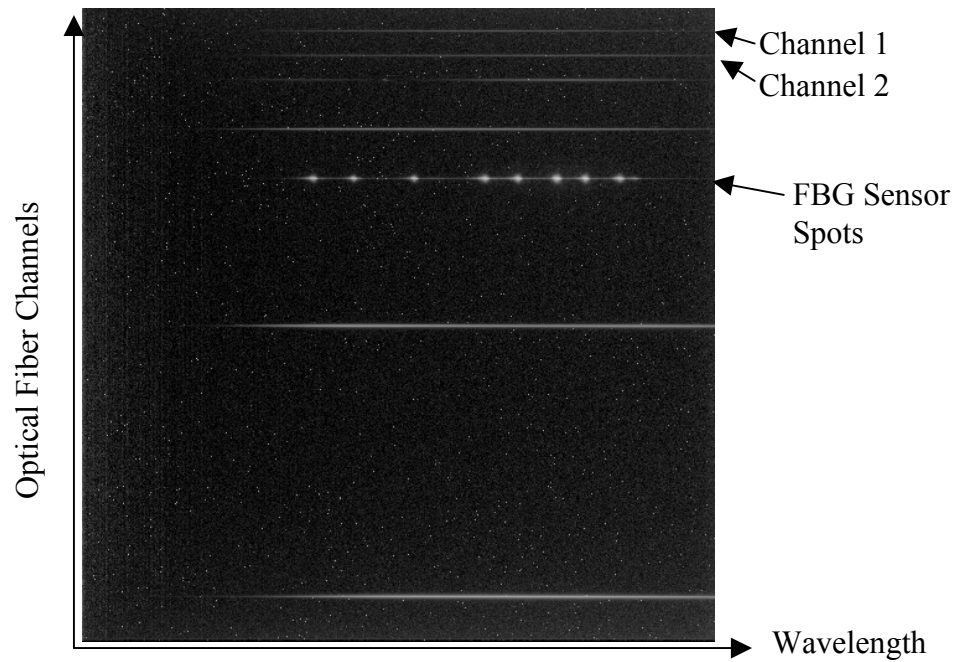
Figure 2.12: Actual image of CMOS camera with sensor spots

Because of the random addressibility of the pixels in the CMOS imager, any

FBG in the network can be addressed in a truly random fashion by reading out only the

relevant pixels and calculating the centroid along the X-axis. This unique feature not

only adds great flexibility for various applications but also enables the system to utilize

its resources efficiently, resulting in a significant performance enhancement.
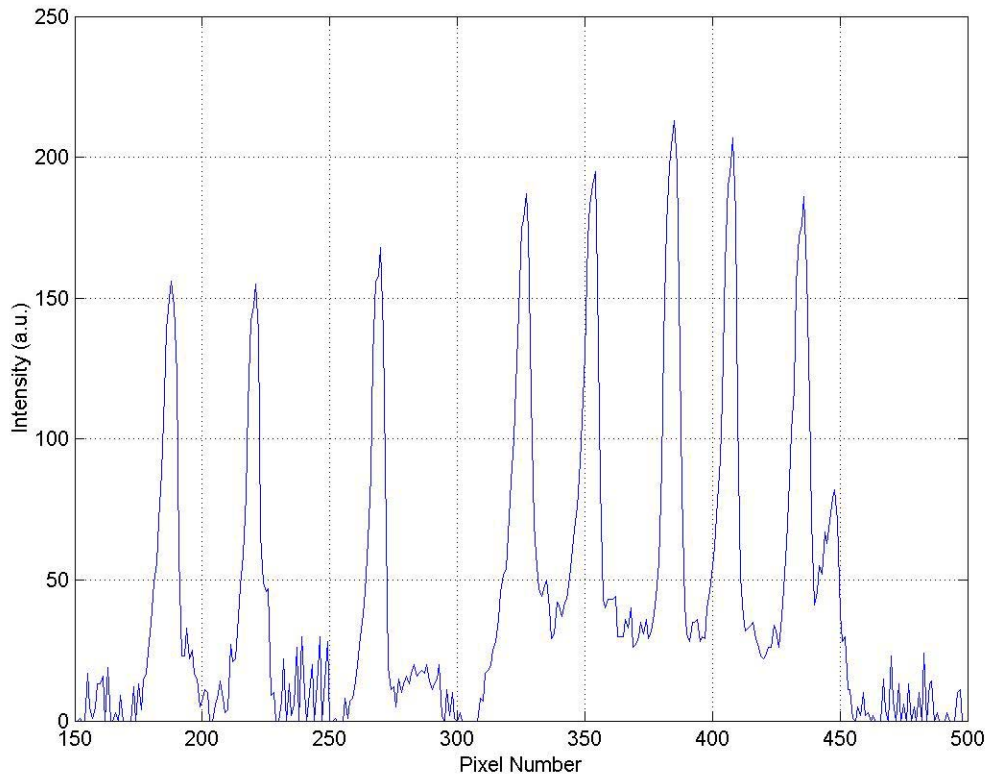
Figure 2.13: Intensity plot for one optical fiber channel showing reflected FBG sensor

signals using the DSWDM system

As can be seen in the intensity plot in Figure 2.13, each sensor spot on the

CMOS imager covers multiple pixels (typically 6 to 8 pixels depending on the spectral

width of the Bragg grating). An average of the intensity spectrum is taken to determine

the pixel location of the centroid of the spot intensity for each sensor. This value is

used to determine the wavelength shift and subsequent strain value for that particular

sensor. This method is shown pictorially in Figure 2.14; it is to be noted that only the

center row of the sensor is recorded for data processing.

31

As the FBG sensors are strained, the spots of the strained gratings move in the X-direction of Figure 2.12 as depicted in Figure 2.14. By determining the precise location of the centroid for a particular spot, the strain of the FBG sensor associated with that spot is determined. Below are the equations that determine the centroid ($\overline{x}$) of the reflected FBG sensor signal and the associated linear transform of the centroid due to axial strain (ε) experienced by the FBG sensor

$$\overline{x} = \frac{\sum_{i=x_{min}}^{x_{max}}(I_i \, x_i)}{\sum_{i=x_{min}}^{x_{max}} I_i} \qquad \varepsilon = \frac{1}{K_{ce}}\left(\frac{\overline{x} - \overline{x}_0}{\overline{x}_0}\right) \tag{2.14}$$

where I_i is the intensity value at pixel number x_i, $\overline{x}_0$ denotes the zero strain position of the centroid, and K_{ce} is a constant that relates a change in centroid to strain.
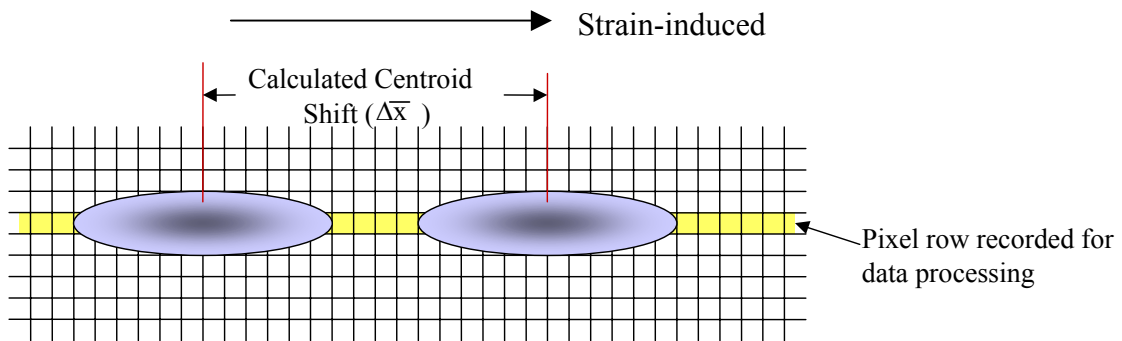
Figure 2.14: Spot shift due to applied strain

2.6 Wavelength Spacing of Sensors

As stated in Section 2.4, the number of FBG sensors that can be interrogated along a single optical fiber is dependent on the optical bandwidth of the broadband source, the optical bandwidth of the interrogation instrument, and the expected thermomechanical response of the FBG sensors. In Figure 2.15, the intensity shift seen on the CMOS is demonstrated for a strain of 250 $\mu\varepsilon$ applied to a FBG sensor. The dashed horizontal line indicates the intensity threshold used in the centroid calculations. Intensity values below this line are not included in the centroid calculation to reduce the influence of noise on the strain measurement. The signal shown outside of the two vertical dashed lines does not vary with respect to the shifting FBG sensor signals. These boundaries have been determined based on many experimental studies previously conducted [Baldwin, et al., 2002(b); Baldwin, et al., 2001a; Christiansen, et al., 2001].
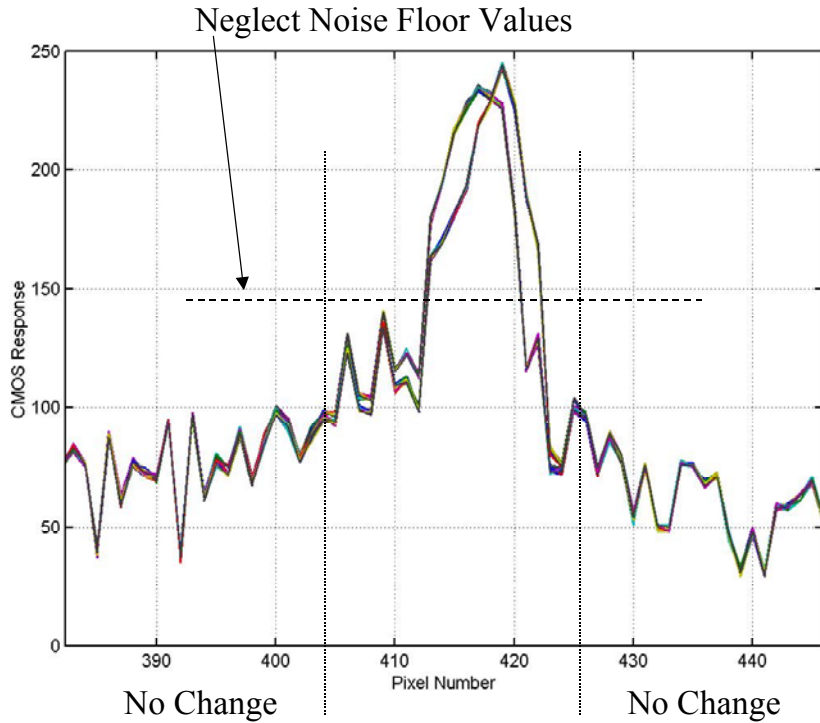
Figure 2.15: FBG sensor pixel shift for 250 με

The majority of the noise shown in Figure 2.15 is due to optical back-reflection from the broadband optical source. Back-reflection occurs in optical systems due to light interacting with physical interfaces such as a mechanical optical connection or a terminated fiber lead. Because the noise comes from the broadband optical source, the noise remains essentially constant throughout the test. For extended measurement sequences (long-term static measurements) variations in the optical output of the broadband source will cause a slight shift in the noise signal. To prevent changes in the noise from influencing the centroid calculation (and hence the strain measurement), intensity values below a certain percentage of the peak intensity are neglected.

The example of a 250 $\mu\varepsilon$ load applied to a FBG sensor is provided to determine the required sensor spacing in wavelength (or pixel) space for the research in this dissertation research. The measured strain values from the individual sensors will be affected if the sensor spectrum overlaps a neighboring sensor spectrum. The FBG sensor center wavelengths must be specified to have adequate spacing between sensors to prevent sensor overlap. An example of the sensor spacing is shown in Figure 2.16, which depicts the centroid shifts of eight FBG sensors during a typical experimental case (discussed in Chapter 5). The oscillations in each sensor signal are due to periodic excitation of the cantilever beam. Each sensor shown in Figure 2.16 has more than 10 pixels, corresponding to more than 1000 $\mu\varepsilon$, in which intensity variations can occur without affecting neighboring sensors. This span is sufficient to ensure no overlap of the sensor signals during the experimental studies of this dissertation.
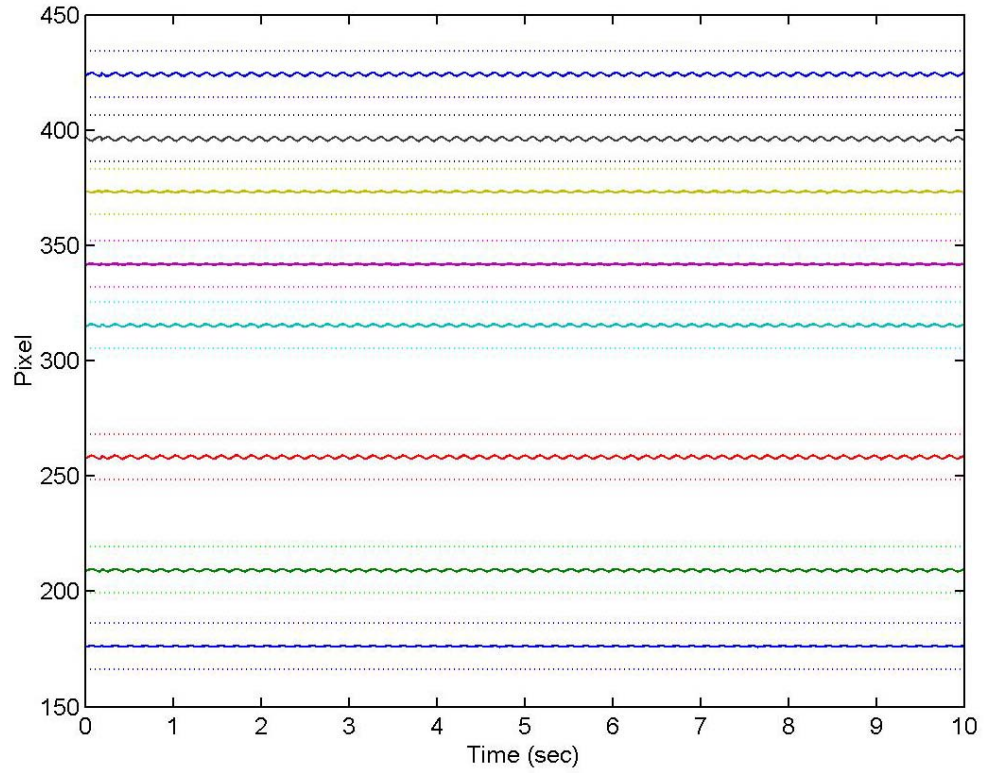
Figure 2.16: Experimental centroid response of FBG sensors

(⎯ Sensor, ⋯ ± 10 Pixel band)

3 Shape Measurement Derivation

The goal of this research is to investigate a dynamic shape sensing system using fiber Bragg gratings for flexible structures. The structure under consideration is modeled as a cantilever beam. Linear analysis of transverse vibrations of an undamped, isotropic cantilever beam is presented in the first section of this chapter. The purpose of this exercise is to demonstrate the basis for the shape determination simulations presented in Section 3.3. The derivation of the shape determination algorithm based on Serret-Frenet frame analysis is given in Section 3.2.

3.1 Natural Modes for a Cantilever Beam

The transverse vibrations of a cantilever beam can be modeled as a function of a single spatial variable, x (along the length of the beam), and time, t [James, 1994]. For transverse displacements in the y direction, the vibration of a cantilever beam can be written in terms of a spatial component, $\phi(x)$, and a time component, q(t) as

$$y(x,t) = \phi(x)q(t) \tag{3.1}$$

In the case of a modal vibration, $\phi(x)$ represents a given mode shape. Considering linear elastic materials, the differential equation of motion for a uniform, cantilever beam is given by [James, 1994]:

$$\frac{EI}{\gamma}\frac{\partial^4 y}{\partial x^4} + \frac{\partial^2 y}{\partial t^2} = 0,$$ (3.2)

where E is the modulus of elasticity of the material, I is the moment of inertia about the bending axis, and γ represents the mass per unit length. After substituting Equation 3.1 into Equation 3.2 the result is

$$\frac{EI}{\gamma}\frac{d^4\phi}{dx^4}q + \frac{d^2 q}{dt^2}\phi = 0$$ (3.3)

Rewriting Equation 3.3 by collecting on terms in ϕ and q yields an equality. For the function to exist, it must equal a constant represented by, ω^2.

$$\frac{EI}{\gamma}\frac{d^4\phi}{dx^4}\frac{1}{\phi} = -\frac{d^2 q}{dt^2}\frac{1}{q} = \omega^2$$ (3.4)

The time component q(t) of Equation 3.4 can be solved by Equation 3.5 where A and B are constants to be determined by the initial conditions of the dynamic system:

$$q(t) = A\cos(\omega t) + B\sin(\omega t)$$ (3.5)

The spatial component $\phi(x)$ of Equation 3.4 is governed by the linear differential equation

$$\frac{d^4\phi}{dx^4} - \frac{\gamma\,\omega^2}{EI}\phi = 0$$ (3.6)

The following function is used to solve the fourth order differential equation

$$\phi(x) = C_1\cosh(kx) + C_2\sinh(kx) + C_3\cos(kx) + C_4\sin(kx)$$ (3.7)

38

where C_i represents constants determined by the boundary conditions of the cantilever beam, and k is given by:

$$k^4 = \frac{\gamma \, \omega^2}{EI} \tag{3.8}$$

For the present application, the solutions for C_i are based on the boundary conditions for a cantilever beam fixed at $x = 0$. These boundary conditions are given as:

$$y(0,t) = 0 \Rightarrow \phi(0) = 0 \tag{3.9a}$$

$$\left.\frac{\partial y(x,t)}{\partial x}\right|_{x=0} = 0 \Rightarrow \left.\frac{d\phi(x)}{dx}\right|_{x=0} = 0 \tag{3.9b}$$

$$\left.\frac{\partial^2 y(x,t)}{\partial x^2}\right|_{x=L} = 0 \Rightarrow \left.\frac{d^2\phi(x)}{dx^2}\right|_{x=L} = 0 \tag{3.9c}$$

$$\left.\frac{\partial^3 y(x,t)}{\partial x^3}\right|_{x=L} = 0 \Rightarrow \left.\frac{d^3\phi(x)}{dx^3}\right|_{x=L} = 0 \tag{3.9d}$$

Applying the conditions given in Equation 3.9 to Equation 3.7 leads to the characteristic equation for a cantilever beam, given by:

$$\cos(kL)\cosh(kL) + 1 = 0 \tag{3.10}$$

Solutions of this equation provides the natural frequencies of the system. As shown in Figure 3.1, Equation 3.10 has solutions at kL values of 1.875, 4.694, 7.854, … These values can be used in Equation 3.7 to determine the mode shape associated with a particular natural frequency.
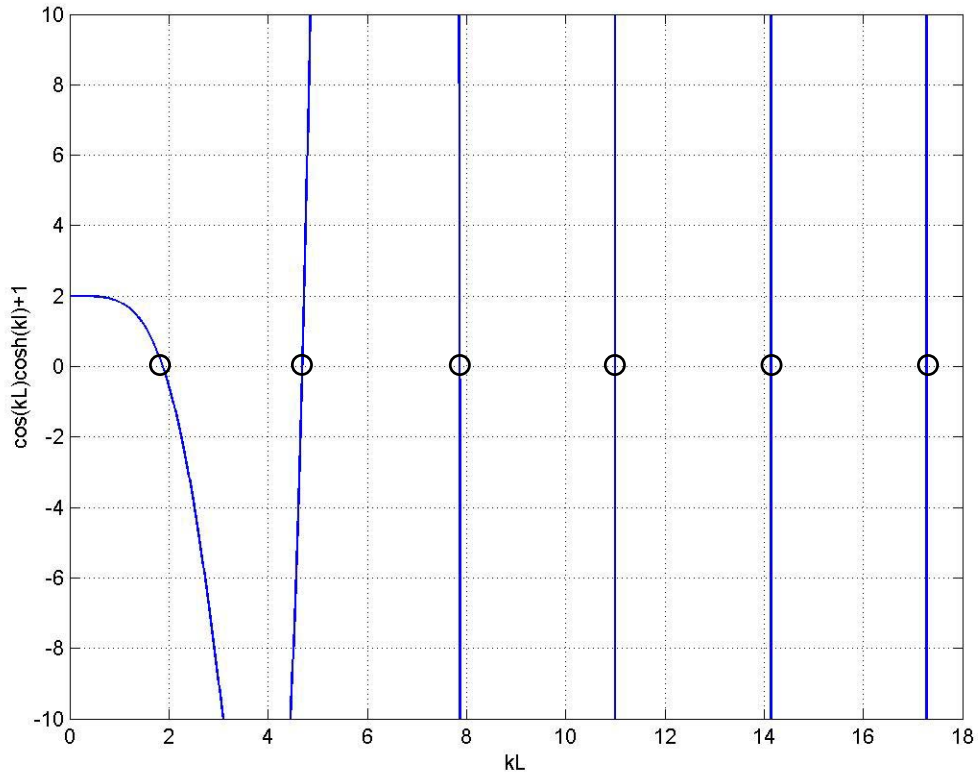
Figure 3.1: Graph of transcendental equation (Equation 3.10) solutions

(solution values shown by o)

The constants (C_i's) in Equation 3.7 must be determined from the boundary conditions given in Equations 3.9a-d. From the boundary conditions, the four constants can be condensed into a single constant that is determined by normalizing the mode shapes. If the product of two different mode shapes is integrated along the length of the beam, the resultant should be zero, as:

$$\int_0^L \phi_i \phi_j dx = 0 \qquad (i \neq j) \tag{3.11}$$

If a normalized mode shape is integrated, this will result in a value of unity, as:

$$\int_0^L \phi_i^2 dx = 1 \tag{3.12}$$

Based on this definition of normal modes, the mode shapes for a uniform cantilever beam can be written as:

$$\phi_i(x) = \cosh(k_i x) - \cos(k_i x) - \alpha_i (\sinh(k_i x) - \sin(k_i x)) \qquad i = 1,2,3,... \tag{3.13}$$

where,

$$\alpha_i = \frac{\cosh(k_i L) + \cos(k_i L)}{\sinh(k_i L) + \sin(k_i L)} \qquad i = 1,2,3,... \tag{3.14}$$

Using Equation 3.13 to represent the mode shape of the cantilever beam, the first four mode shapes are obtained as shown in Figure 3.2.
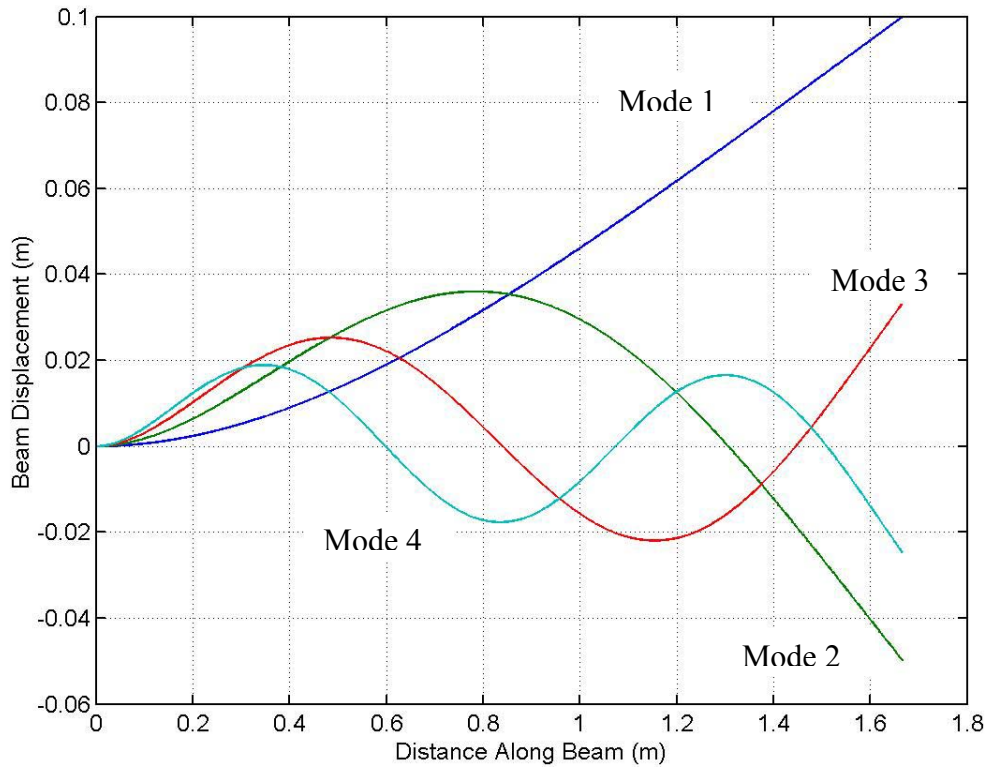
Figure 3.2: Calculations for the first four mode shapes

3.2 Shape Determination by using Serret-Frenet Frames

The vector relationships defining motion along a space curve are developed

through the use of Frenet formulas [Ventsel, 2001; Thomas and Finney, 1992]. These

relations define Frenet-Serret motion that relates the motion of an object to the

curvature and torsion of the path along which the object moves through space. An

application of these relationships is in the theory of cable dynamics [Behbahani-Nejad

and Perkins, 1997]. The deformation of a cantilever beam can be considered as a curve

in space, y = f(x), where a particle travels along the shape of the deflected beam. The

torsion component is always zero and the curvature components are related to the

bending strain through a basic strain mechanics model. The curve 'y' can be

represented in terms of the mode shapes (ϕ) of the beam, as discussed in Section 3.1.

For more complex structures such as cables and hoses, the rotation of the structure must

be considered through torsion of the space curve. The concept of Serret-Frenet analysis

for structural shape monitoring as been recently investigated for towed sonar array

applications (unpublished as of this date). This is the first discussion of this technique

for cantilever beams. Later in this work, the first successful experimental verification

of this technique is provided.

3.2.1   Shape Algorithm Derivation

If a global coordinate system is anchored at the root of the cantilever beam, then

each point along the beam (space curve) can be located by the parametric function:

$$\mathbf{R}(\eta) = X(\eta)\mathbf{i} + Y(\eta)\mathbf{j} + Z(\eta)\mathbf{k} \tag{3.15}$$

where η is a parameter such that each value of η will determine one unique point on the

space curve. For the case of a cantilever beam undergoing excitation in only the y

direction, $Z(\eta)$ can be considered a constant or zero, assuming that the beam exhibits

motions in the x-y plane.

The value for curvature (κ) of the deflected cantilever beam is defined as the reciprocal of the radius of curvature (ρ) [Beer and Johnston, 1981].

$$\kappa = \frac{1}{\rho} = \frac{\phi''}{\left[1 + \phi'^2\right]^{3/2}} \tag{3.16}$$

where the prime denotes differentiation with respect to the x variable. For cases of small deflections, the derivative of ϕ is small and the value for curvature can be approximated by:

$$\kappa = \frac{1}{\rho} \approx \phi'' \tag{3.17}$$

Based on a mechanics of materials approach, the bending strain measured on the surface of the cantilever beam is related to the curvature through the following relation [Beer and Johnston, 1981]

$$\varepsilon = \kappa\left(h/2\right) \approx \phi''\left(h/2\right) \tag{3.18}$$

where h represents the thickness of the beam. The method for shape determination used in this dissertation involves the use of the Serret-Frenet formulae. These formulae relate curvature to the local rectangular coordinate system. Figure 3.3 provides a pictorial description of the Frenet frame coordinates and curvature for an arbitrary curve [Thomas and Finney, 1992]. In Appendix A, the relationship between the mechanical curvature (κ) and the vector relations discussed in this section are formed. The basis of this method is to relate a local coordinate system at the sensor locations to the global coordinate, fixed frame, at the root of the beam. The local coordinate system is determined based on the differential geometry of the Serret-Frenet formulation. The local system of vectors is given by the tangent vector, **T**, the principal normal vector, **N**, and the bi-normal vector **B** = **T** × **N**.

44
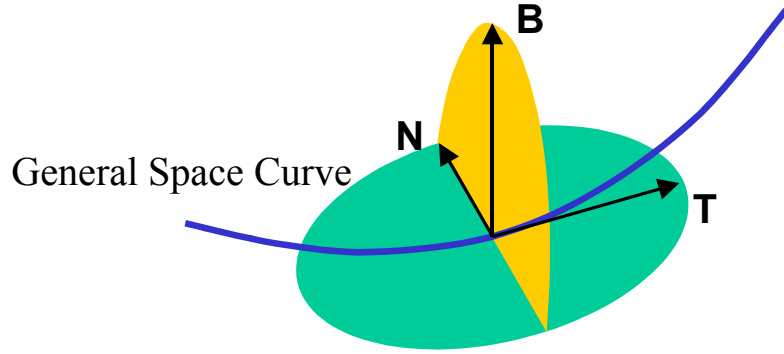
Figure 3.3: Local set of unit vectors along a general space curve

The origin of the global coordinate system is located at the first sensor (or root of the beam), and the local vectors $\mathbf{T}$, $\mathbf{N}$, and $\mathbf{B}$ for the origin are the unit vectors $\mathbf{i}$, $\mathbf{j}$, and $\mathbf{k}$ that are fixed in the global frame. For a cantilever beam, the strain at the free end of the beam will always be zero, and hence no sensor is required at this location.

The beam is described by a parametric vector function $\mathbf{R}(s) = (x(s), y(s), z(s))$, where 's' is a variable that travels along the beam span. The coordinates $x(s)$, $y(s)$, and $z(s)$ refer to the coordinates in the global frame. Through the use of a Taylor series expansion, the vector $\mathbf{R}(s)$ can be determined in terms of a previous point along the curve, $\mathbf{R}(a)$.

$$\mathbf{R}(s) = \mathbf{R}(a) + (s-a)\frac{d\mathbf{R}(s)}{ds}\bigg|_{s=a} + \frac{(s-a)^2}{2!}\frac{d^2\mathbf{R}(s)}{ds^2}\bigg|_{s=a} + \frac{(s-a)^3}{3!}\frac{d^3\mathbf{R}(s)}{ds^3}\bigg|_{s=a} + \ldots \qquad (3.19)$$

Equation 3.19 can be simplified by inserting the following Serret-Frenet formulae:

$$\frac{d\mathbf{R}(s)}{ds} = \mathbf{T}(s), \quad \frac{d\mathbf{T}(s)}{ds} = \kappa(s)\mathbf{N}(s), \quad \frac{d\mathbf{N}(s)}{ds} = -\kappa(s)\mathbf{T}(s) + \tau(s)\mathbf{B}(s) \qquad (3.20)$$

where $\kappa(s)$ and $\tau(s)$ are the curvature and torsion at location 's', respectively.

$$\mathbf{R}(s) = \mathbf{R}(a) + (s-a)\mathbf{T}(a) + \frac{(s-a)^2}{2}\kappa(a)\mathbf{N}(a) +$$
$$\frac{(s-a)^3}{6}\left\{ \left. \frac{d\kappa(s)}{ds}\right|_{s=a} \mathbf{N}(a) + \kappa(a)\left[-\kappa(a)\mathbf{T}(a) + \tau(a)\mathbf{B}(a)\right]\right\} + \ldots$$

(3.21)

Limiting the expansion to the third order and collecting on terms of $\mathbf{T}(a)$, $\mathbf{N}(a)$, and $\mathbf{B}(a)$

leads to:

$$\mathbf{R}(s) = \mathbf{R}(a) + \left\{ (s-a) - \frac{(s-a)^3}{6}\kappa^2(a)\right\}\mathbf{T}(a) + \left\{ \frac{(s-a)^2}{2}\kappa(a) + \frac{(s-a)^3}{6}\left.\frac{d\kappa(s)}{ds}\right|_{s=a}\right\}\mathbf{N}(a) +$$
$$\left\{ \frac{(s-a)^3}{6}\kappa(a)\tau(a)\right\}\mathbf{B}(a)$$

(3.22)

Equation 3.22 shows that the position vector at location 's' is determined by the

position vector at location 'a' plus modifications of the Frenet frame vectors by the

curvature and torsion values at position 'a'. Therefore, Equation 3.22 can be used as a

basis for mapping the shape of a structure if the curvature, torsion, and Frenet frame

vectors are known at some starting point 'a'. By taking derivatives of $\mathbf{R}(s)$ and using

Serret-Frenet formulae given by Equation 3.20, the Frenet vectors $\mathbf{T}$ and $\mathbf{N}$ can be

determined at any location 's', as:

$$\mathbf{T}(s) = \frac{d\mathbf{R}(s)}{ds} = \left[1 - \frac{1}{2}(s-a)^2\kappa^2(a)\right]\mathbf{T}(a) + \left[(s-a)\kappa(a) + \frac{1}{2}(s-a)^2\left.\frac{d\kappa(s)}{ds}\right|_{s=a}\right]\mathbf{N}(a) +$$
$$\left[\frac{1}{2}(s-a)^2\kappa(a)\tau(a)\right]\mathbf{B}(a)$$

(3.23)

$$\mathbf{N}(s) = \frac{1}{\kappa(s)} \frac{d\mathbf{T}(s)}{ds} =$$

$$\frac{1}{\kappa(s)} \left[\left\{ -(s-a)\kappa^2(a) \right\} \mathbf{T}(a) + \left\{ \kappa(a) + (s-a)\frac{d\kappa(s)}{ds} \bigg|_{s=a} \right\} \mathbf{N}(a) + \left\{ (s-a)\kappa(a)\tau(a) \right\} \mathbf{B}(a) \right]$$

$$(3.24)$$

The bi-normal vector at location 's' is determined by the cross product of the tangent and normal vector, as:

$$\mathbf{B}(s) = \mathbf{T}(s) \times \mathbf{N}(s) \tag{3.25}$$

3.2.2 Example of Shape Algorithm

Equations 3.23, 3.24, and 3.25 provide a means for obtaining the Frenet frame vectors at a position 's' based on values at a previous position 'a'. Therefore, a structure can be divided into sections where the determination of the deflection at the end of the section is based on the values at the beginning of the section. For the case of a cantilever beam, this implies dividing the beam along the length into multiple sections. The first section begins at the root of the beam where $\mathbf{R}$, $\mathbf{T}$, $\mathbf{N}$, and $\mathbf{B}$ are defined as: $\mathbf{R}(0) = (0,0,0)$, $\mathbf{T}(0) = \mathbf{i}$, $\mathbf{N}(0) = \mathbf{j}$, and $\mathbf{B}(0) = \mathbf{k}$. Based on the value of strain at the root of the beam, the value for curvature is known from Equation 3.18. Therefore, the position of the beam at the end of the section is known from the above equations. As long as the curvature (or strain) is known along the length of the beam, the above equations can be used to "map out" the deflection of the beam along its entire length as illustrated in Figure 3.4.
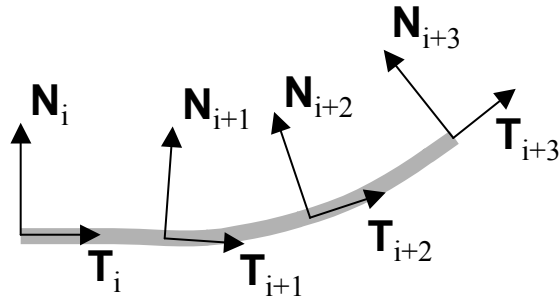
Figure 3.4: Depiction of the coordinate frame updating

These relations have been implemented into a Matlab algorithm to compute the shape of the cantilever beam based on the distributed strain readings along the length of the beam structure. The following sections provide numerical results obtained from this formulation.

3.3 Numerical Simulations of the Shape Algorithm

An integral part of the shape measurement system is the algorithm that calculates the mode shape of the vibrating structure from the recorded strain readings of the FBG sensors. In order to determine modal properties, the change in the shape must be examined over a given time period. The analysis presented here does not consider randomly varying forces, but only for vibrations associated with periodic excitations.

Simulations are presented for the case of a vibrating cantilever aluminum beam. Material properties and geometry are chosen as discussed in Chapter 5. The motion of

the beam is considered to be linear and consist of small deflections (as discussed in Section 3.1). The simulation procedure consists of three parts 1) generation of a particular mode shape, 2) determination of the corresponding strain values at the sensor locations, and 3) calculation of curvature values at and between sensor locations (calculation of values between sensor locations is described in detail below). The generation of the mode shape is only used to generate simulated strain and curvature data. The assumed shapes are the mode shapes of a cantilever beam, given by Equation 3.13, and the simulations are restricted to one mode shape at a time. Once the reference mode shape is input to the code, the sensor locations are assumed uniformly spaced along the span of the beam and strain readings are calculated from the reference shape at these locations. Values for curvature at the sensor locations are then determined from the theoretical strain values. The shape calculation algorithm was then used to process the curvature values following the discussion in Section 3.2.1.

A measurement system that provides accurate data along the length of the beam with a minimum number of sensors is desired. To increase the resolution of the shape measurement algorithm, an estimation of the strain (and/or the curvature) between the sensor locations is performed. Multiple estimation methods are available to allow the calculation of data points between the sensor values including linear approximation, cubic Hermitic spline, and general cubic spline interpolation of the data set. The linear interpolation method assumes a separate linear function between each of the data points. This creates a disjointed function for the strain across the length of the beam. The cubic Hermitic spline attempts to fit the given data set to a third order Hermite polynomial

49

equation. A disadvantage of this technique is that outlying data points may be considerably out of range of the determined best-fit function [MATLAB, 2000]. The most appropriate method for the shape estimation algorithm is the general cubic spline method, as will be demonstrated in this section. Similar to the linear interpolation method, the cubic spline technique assumes a distinct function between each pairs of data points. Instead of a discontinuous function, each function is "fitted" at the data points by equating not only the data point but also the first and second derivatives of the functions. The following section provides examples of each of these fitting methods. Qualitative analysis demonstrates the effectiveness of these methods on various mode shapes. An error function is presented in Chapter 4, and this will be used for quantitative purposes in the shape sensing algorithm.

The following sections describe the modeling for the various interpolations described above. The cantilever structure being modeled in these cases is an aluminum structure that has the dimensions of 65.625×2.0×0.125 inches (166.7×5.1×0.32 cm). The clamp at the base of the structure is used to realize. The sensor locations for the structure are assumed to be equally spaced along the structure's length. To simulate the experimental case, only eight sensors are modeled along the structure's span. The tip of the cantilever structure is assumed to have zero strain for all cases. For the purposes of the simulations, the cantilever structure is modeled as a cantilever beam.

3.3.1 Linear Interpolation Method
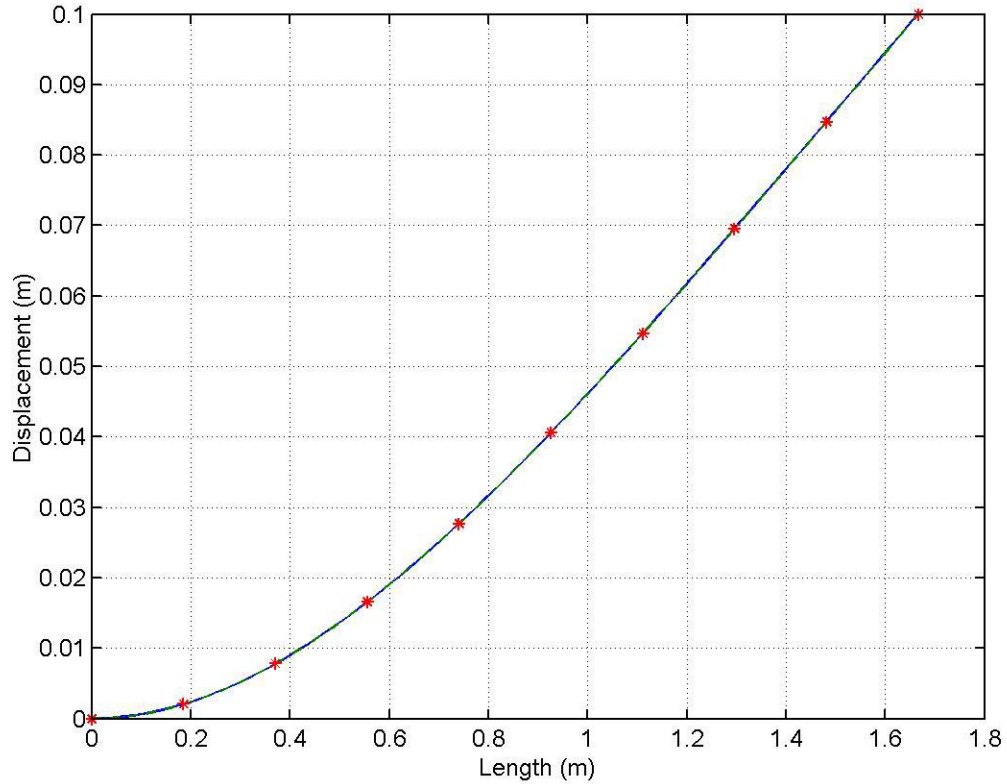
Figure 3.5: Mode 1 shape with linear interpolation between sensor node points

(*-) theoretical, (⎯) simulated algorithm

In Figure 3.5, the simulation results for a mode 1 deflection of the cantilever structure are shown. As displayed, the linear interpolation of the curvature between the chosen sensor locations provides an accurate interpretation of the mode shape. The accuracy of this result can be explained by examining the predicted strain distribution along the length of the structure for this mode shape. In Figure 3.6, the strain distribution is illustrated along the structure's span. At the end of the span, a nonlinear

characteristic is observed, but the assumption of linear strain variation does not affect

the mode shape approximation much. However, as the order of the mode shape

increases, the linear interpolation method provides results that deviate from the

predicted mode shape, as shown in Figure 3.7 and Figure 3.8. A similar trend was also

observed in the results obtained for mode 3.
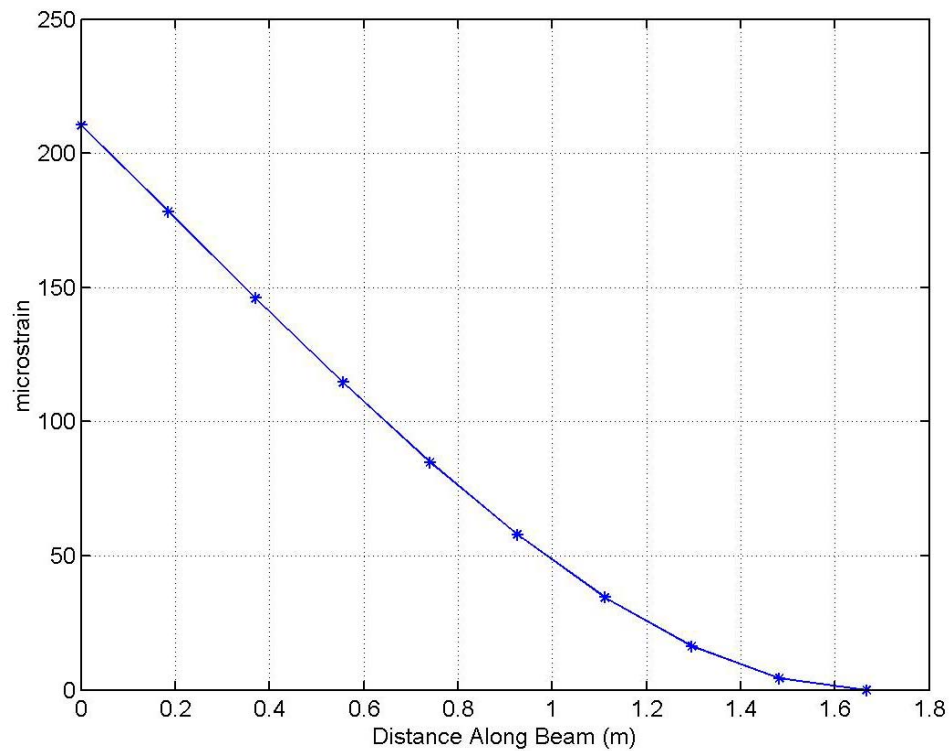
Figure 3.6: Strain variation along the structure for mode 1 shape

{chosen sensor locations are marked by (*)}
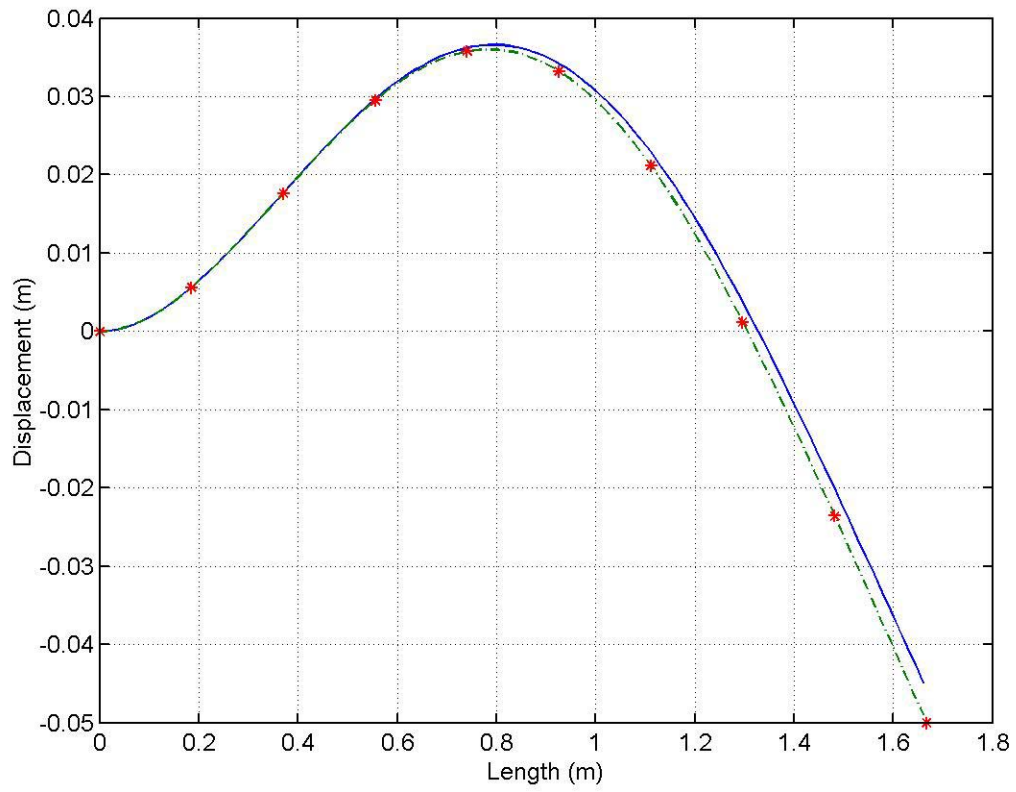
Figure 3.7: Mode 2 shape approximation with linear interpolation

(*-) theoretical and (——) simulated algorithm
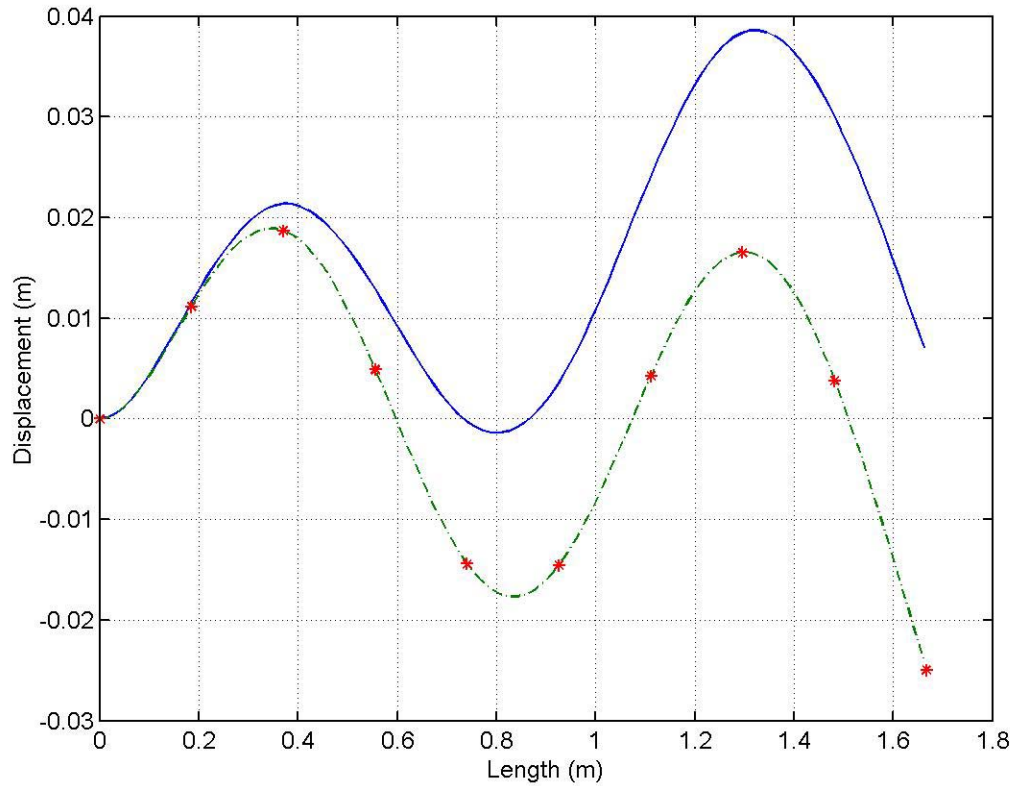
Figure 3.8: Mode 4 shape approximation with linear interpolation

(*-) theoretical and (—) simulated algorithm

As illustrated, the linear interpolation method provides reasonable results for the first mode. For higher order modes, the linear approximation results in considerable errors in the shape calculation algorithm. These errors propagate down the length of the beam resulting in large errors at the beam tip. It should be noted that this method could be improved by increasing the number of sensors along the length. This statement is true for all other methods as well, as will be discussed in the following chapter.

3.3.2 Cubic Hermitic Interpolation Method

The cubic Hermitic interpolation method is provided as a built in MATLAB function. This method is similar to the cubic spline method discussed in Section 3.3.3. The cubic Hermitic method is sometimes used because it takes less processing time than the general cubic spline interpolation method [MATLAB, 2000]. The cubic Hermitic function is represented by Equation 3.26, where the variable C is used to determine the interpolation fit for the data.

$$H_3(x) = C\left(x - \frac{2}{3}x^3\right) \tag{3.26}$$

With only one variable to define, the cubic Hermetic interpolation method is simpler than a general cubic spline method, but it has limited effectiveness. The interpolation is accomplished by matching the data point values and the first and second derivatives of the Hermetic function at the data point location. Mode shape approximations obtained by using the cubic Hermitic interpolation method are presented in Figure 3.9 through Figure 3.11. Higher order mode shapes exhibit an improvement over the linear interpolation method. Mode 3 simulation results are similar to these obtained for mode 2, and they are not shown here in the interest of space.
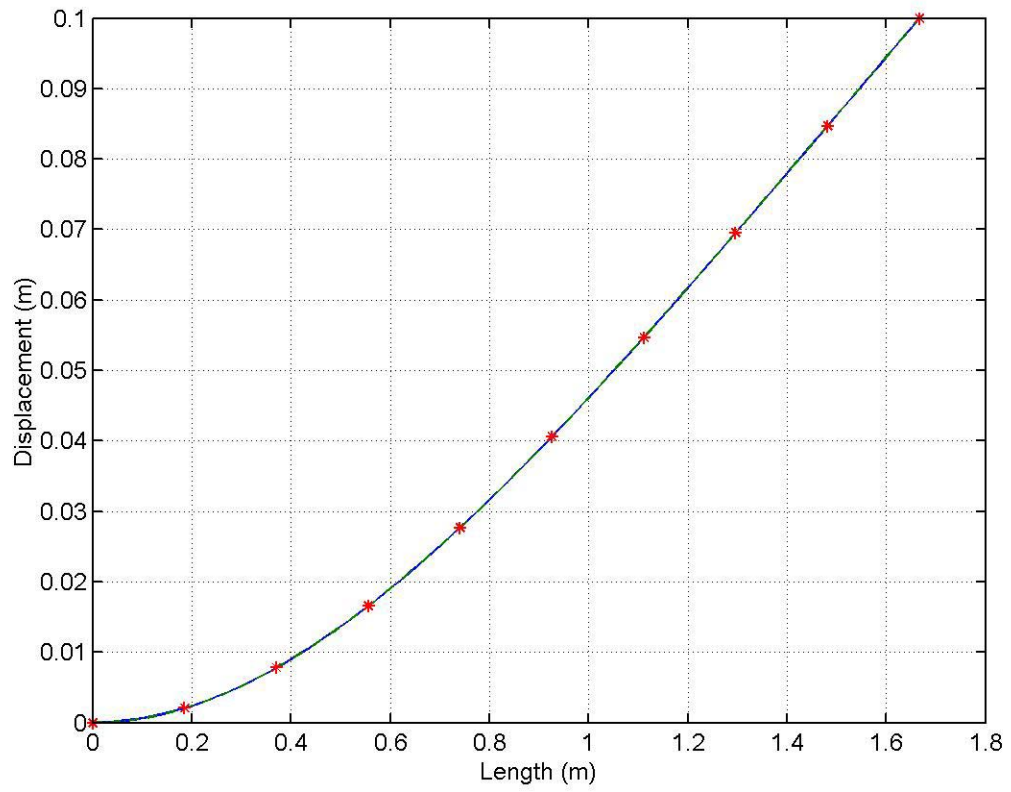
Figure 3.9: Mode 1 shape approximation with cubic Hermitic interpolation

(*-) theoretical and (—) simulated algorithm
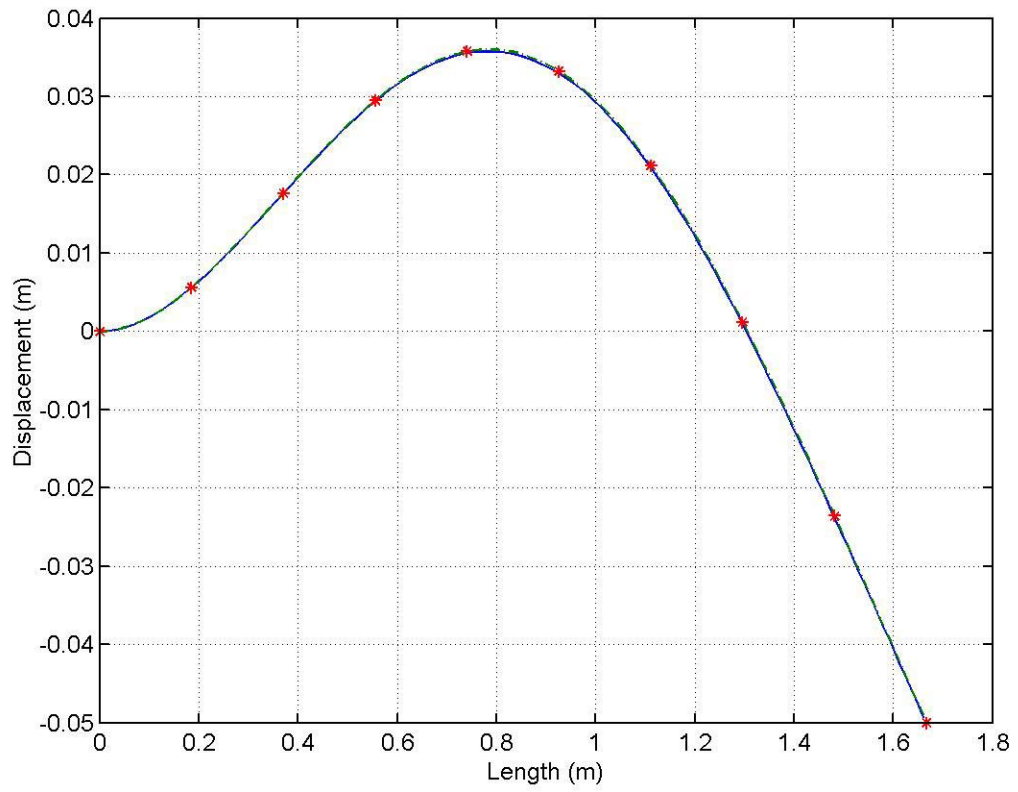
Figure 3.10: Mode 2 shape approximation with cubic Hermitic interpolation

(*-) theoretical and (——) simulated algorithm
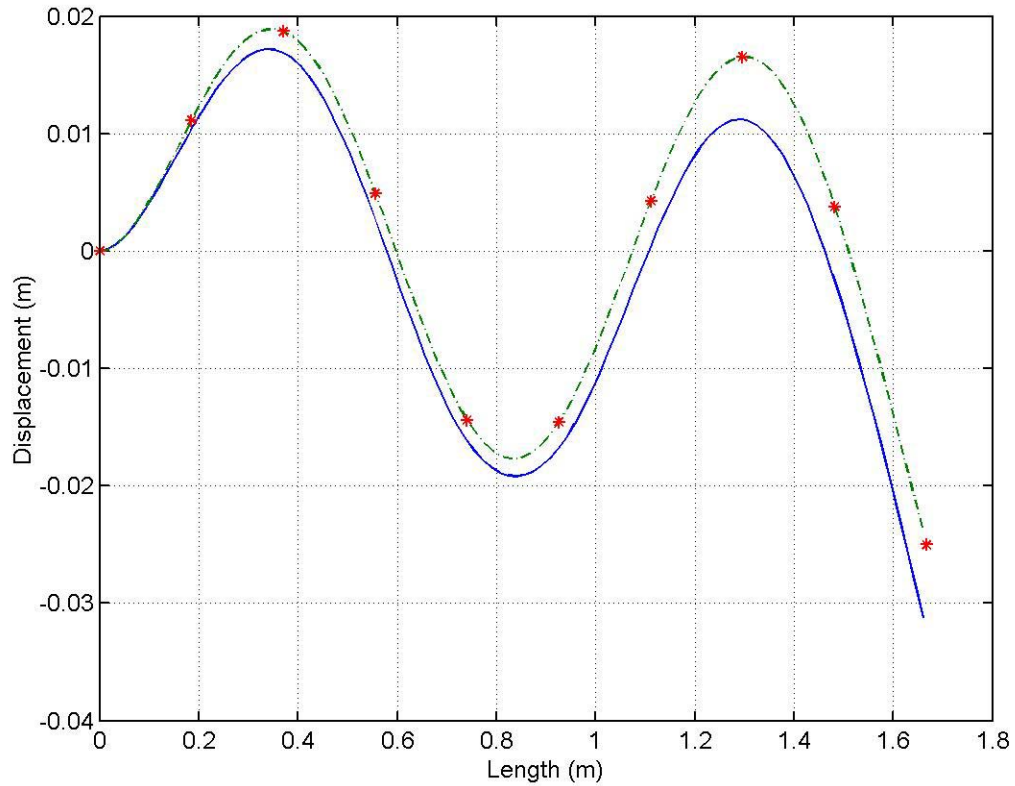
Figure 3.11: Mode 4 shape approximation with cubic Hermitic interpolation

(*-) theoretical and (—) simulated algorithm

3.3.3   Spline Interpolation Method

The cubic spline interpolation method fits a different cubic function between each pair of existing data points. This method not only matches the value of the data point, but also the first and second derivative at these points. This method allows for more generic cubic interpolation functions then the cubic Hermetic discussed in Section 3.3.2. As shown in Figure 3.12 through Figure 3.14, this method provides a more

58

accurate approximation for each mode shape of the cantilever beam for the first and higher order modes. Again, the mode 3 simulation results are similar to the mode 2 results, and they are not shown in the interest of space. Based on the numerical results, the cubic spline interpolation is used for the shape determination algorithm.
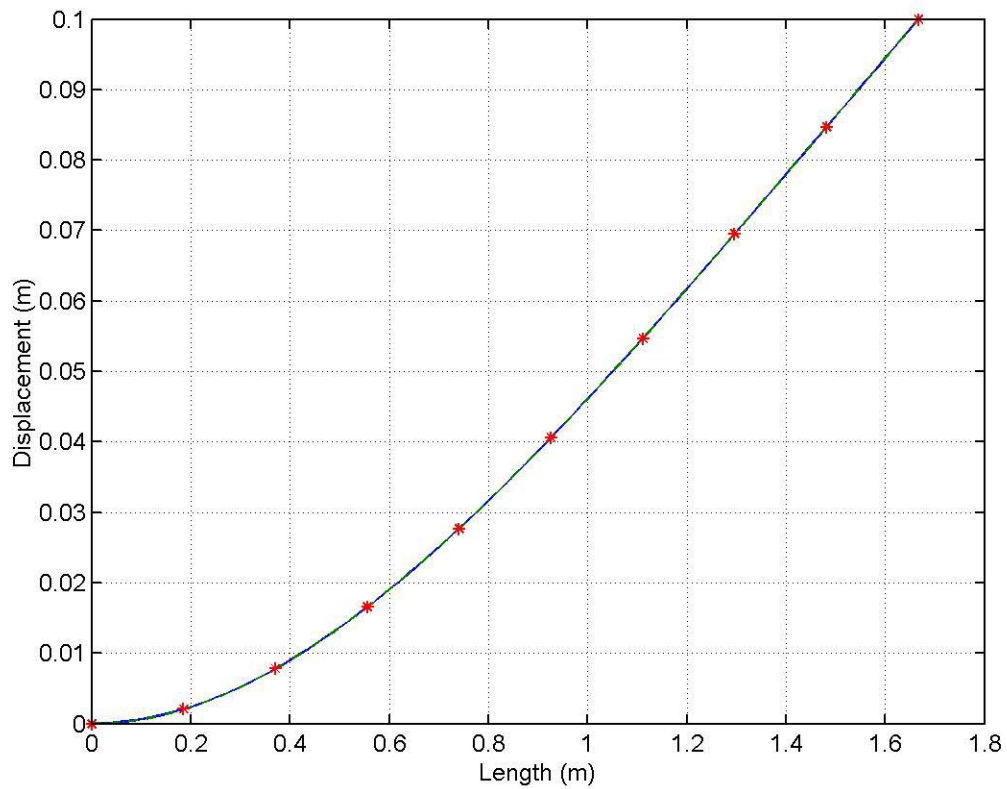
Figure 3.12: Mode 1 shape approximation with cubic spline interpolation

(*-) theoretical and (—) simulated algorithm
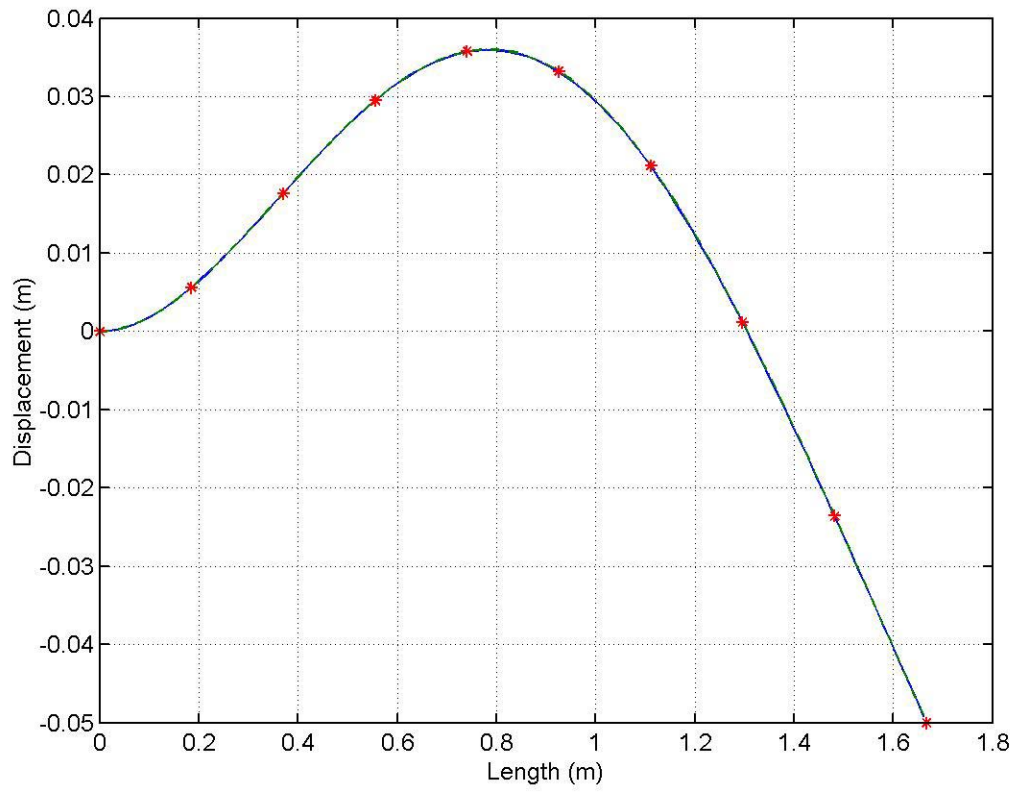
Figure 3.13: Mode 2 shape approximation with cubic spline interpolation

(*-) theoretical and (——) simulated algorithm
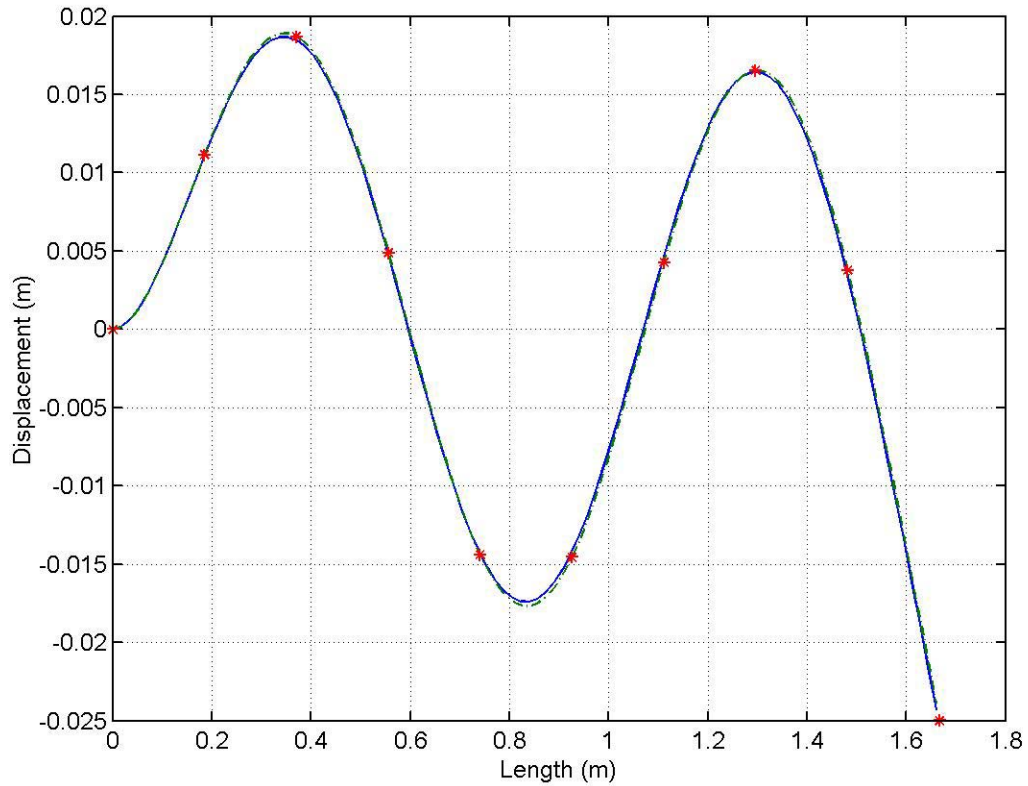
Figure 3.14: Mode 4 shape approximation with cubic spline interpolation

(*-) theoretical and (——) simulated algorithm

3.4 Analysis for Higher Mode Shapes

For higher order mode shapes, as shown in Figure 3.15 for the case of a mode shape of the sixth mode, differences exist between the simulated and predicted results; this is attributed to the number of sensors used to measure strain along the structure. Again, for more complicated shapes, with many inflection points, at least one sensor per sign change is required to resolve the deformation of the structure. As the number of

sensors is increased, better estimates for strain and curvature can be determined along the structure's span, thus improving the accuracy of the algorithm. It is to be noted that not only the number of sensors, but also the number of interpolation points and type of interpolation used will affect the accuracy of the shape determination algorithm. These errors will be discussed further in the following chapter.
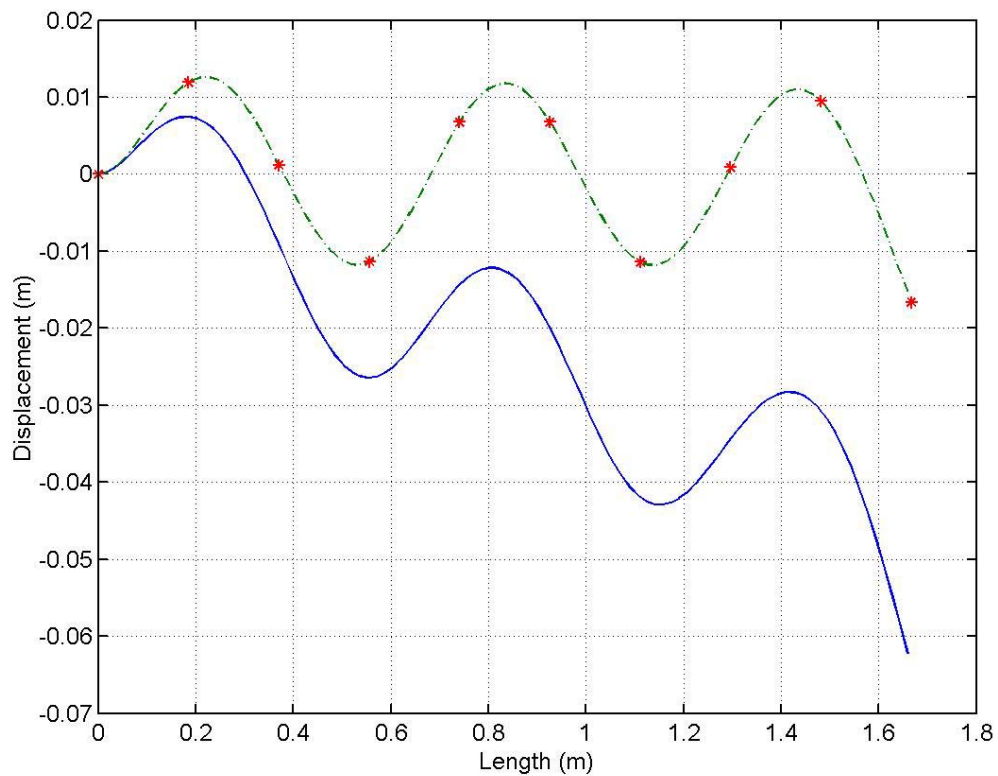
Figure 3.15: Mode 6 shape approximation with cubic spline interpolation

(*-) theoretical and (——) simulated algorithm

4   Shape Algorithm Error Analysis

This chapter of the dissertation explores various aspects of the shape measurement algorithm through numerical simulations. First, an error function is defined for comparing two shapes. This quantitative measure is used throughout the research. In the second section of this chapter, possible influences of the Taylor series expansion used in the shape algorithm derivation are explored. In the third section, analysis of the number of sensors used on the structure and the number of interpolation points between the sensors is presented. In the final section, an overview of the Pearson correlation function is given, and the reasoning for not using this comparative function for shape comparison is demonstrated.

4.1 Quantitative Error Analysis

To provide a quantitative measure for the error sources in the shape algorithm, a method to compare the results of the shape algorithm calculation to the theoretical mode shape was developed. One method would be to determine the difference in tip deflections between the predicted and calculated mode shapes. This method would be

adequate for applications concerned only with locating the end of the beam (or flexible structure) and not concerned with the structure's shape throughout the entire length. However, the objective here is to develop methods for determining accurate shapes, so a tip deflection method is not sufficient to evaluate the algorithm. Rather, an error calculation method is used that incorporates the entire length of the beam in the calculation. The beam is divided into equal sections with the error of the shape estimation being determined as a sum of squares at the end of each section. For example, shape estimate data for the mode 1 shape shown in Figure 4.1 has been divided into ten sections.
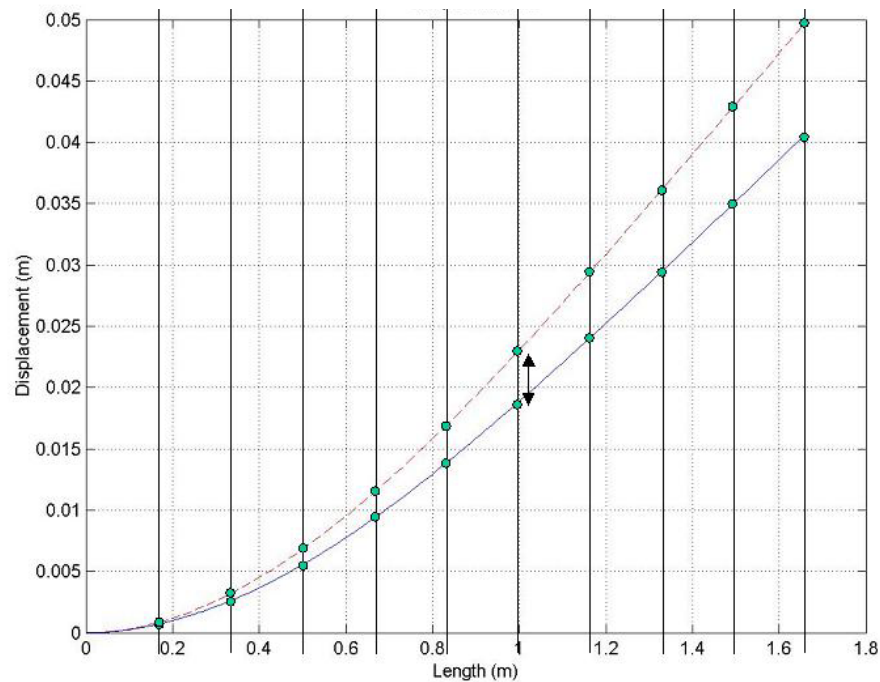
Figure 4.1: Representative illustration of error between reference and experimental data for a mode 1 shape

The differences in the deflection values are included in the error calculation given by:

$$\text{error}_n = \sqrt{\left(\left(y_{exp\_1} - y_{theory\_1}\right)^2 + \left(y_{exp\_2} - y_{theory\_2}\right)^2 + \ldots + \left(y_{exp\_n} - y_{theory\_n}\right)^2 \right)} \qquad (4.1)$$

where y_{exp} is the experimental value for the beam shape (provided by the algorithm calculation for either simulation results or experimental results) and y_{theory} is the theoretical shape value based on the mode shape analysis of Section 3.1. Equation 4.1 is the general form for the error equation. The value of 'n' is the number of equal segments into which the beam is divided. To test this error analysis equation, the hypothetical case displayed in Figure 4.2 is examined.
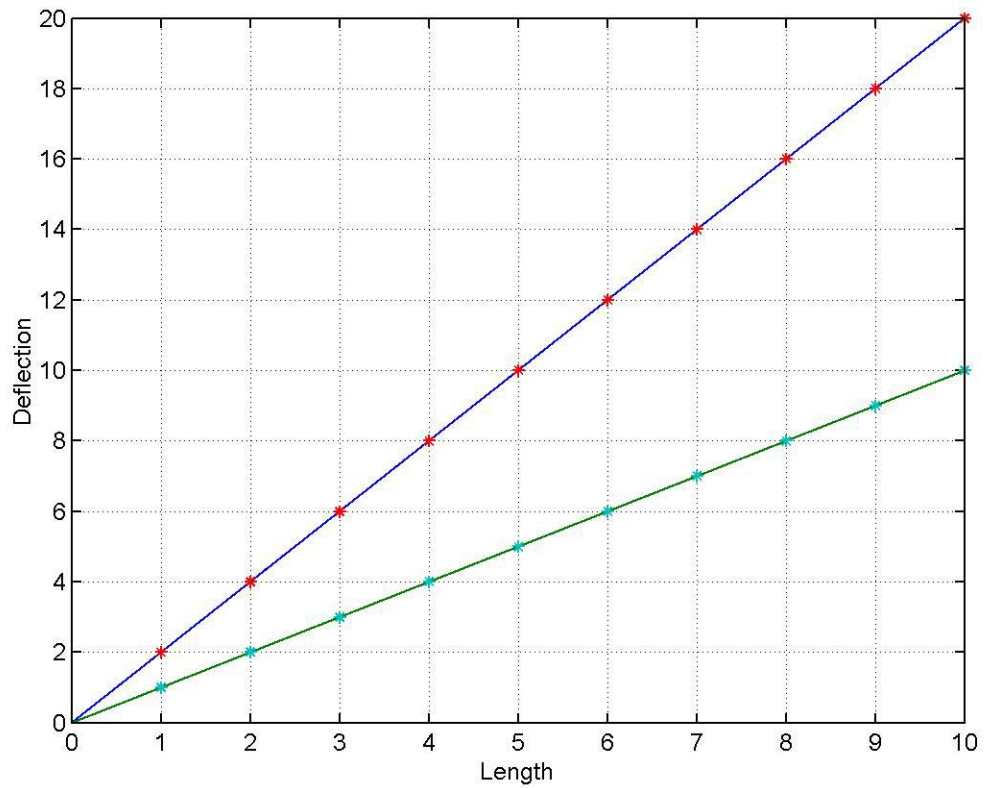
Figure 4.2: Demonstration of error calculations for two linear functions with 10 segments

(* points of data for error calculation)

The proposed error function given in Equation 4.1 is plotted against the number of error points included in the error calculation in Figure 4.3. As the value of n increases the error function given by Equation 4.1 does not converge.
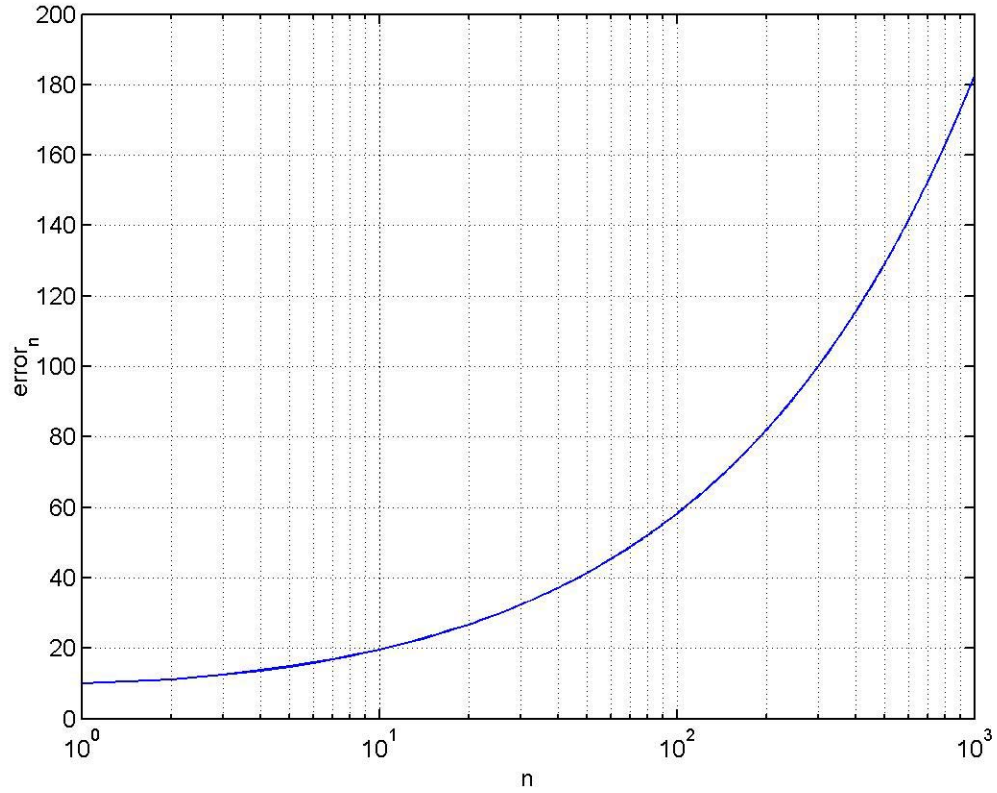
Figure 4.3: Value of error (Equation 4.1) for increasing number of calculation points

For the error function to coverage, the sum of the squared errors must be divided by n, as shown in Equation 4.2. This allows the error function to converge to an error quantity for an increasing 'n' value as shown in Figure 4.4.

$$\text{error}_n = \sqrt{\frac{\left(\left(y_{exp\_1} - y_{theory\_1}\right)^2 + \left(y_{exp\_2} - y_{theory\_2}\right)^2 + \ldots + \left(y_{exp\_n} - y_{theory\_n}\right)^2\right)}{n}} \qquad (4.2)$$

Figure 4.4 shows the error function converging at an 'n' value over 100. This calculation provides a quantitative method for determining error in the shape estimation compared to the theoretical model. This error calculation will be applied to both the analytical analysis and the experimental data in this research investigation.

67
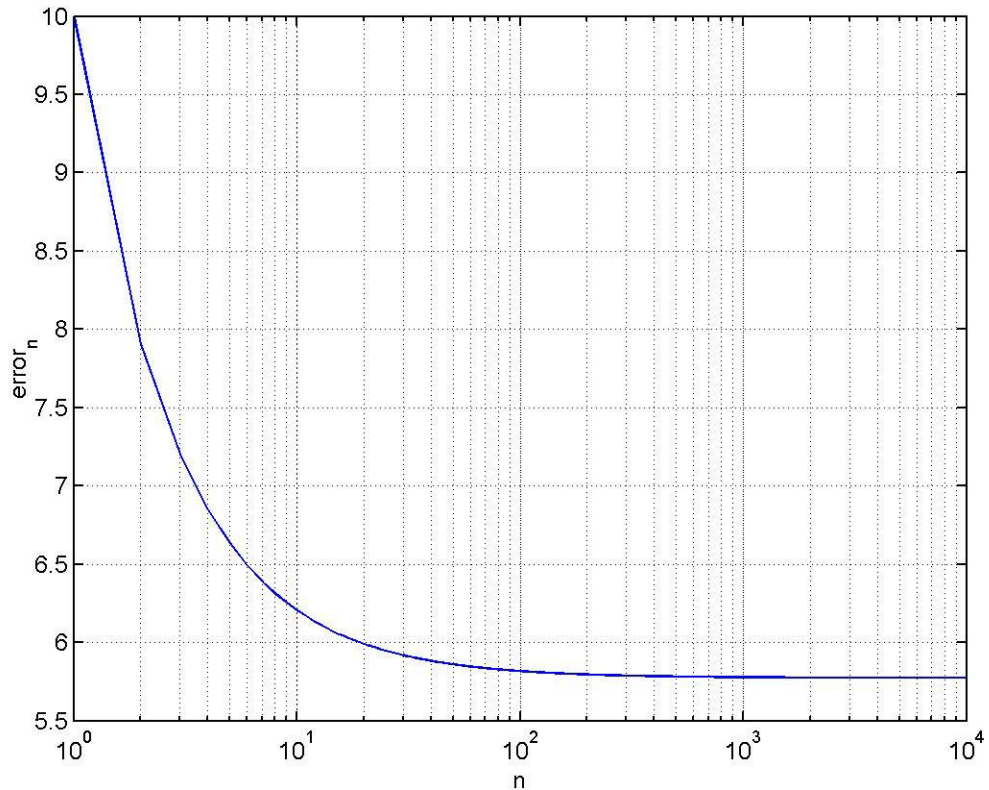
Figure 4.4: Value of error (Equation 4.2) for increasing number of calculation points

4.2 Taylor Series Expansion

An integral part of the shape determination algorithm is the use of a Taylor series to evaluate the position of the structure along the length. The Taylor series is a valuable mathematical tool used to evaluate values of functions about a "known" point using a power series based on the function's derivatives. The Taylor series approximation is used in a marching forward mode along the entire length of the

structure and hence serves as a potential source of error for the shape calculation

algorithm.

4.2.1   Example with Sine Function

As an example of the application of Taylor series to a known function, Figure

4.5 shows the sine function evaluated at $x = 2\pi$, approximated using only the first three

terms of the Taylor series expansion. Use of more terms would provide a better

approximation along a longer interval of the function. The area marked by the dashed

box in Figure 4.5 represents the estimated region of adequate approximation for the

Taylor series function.
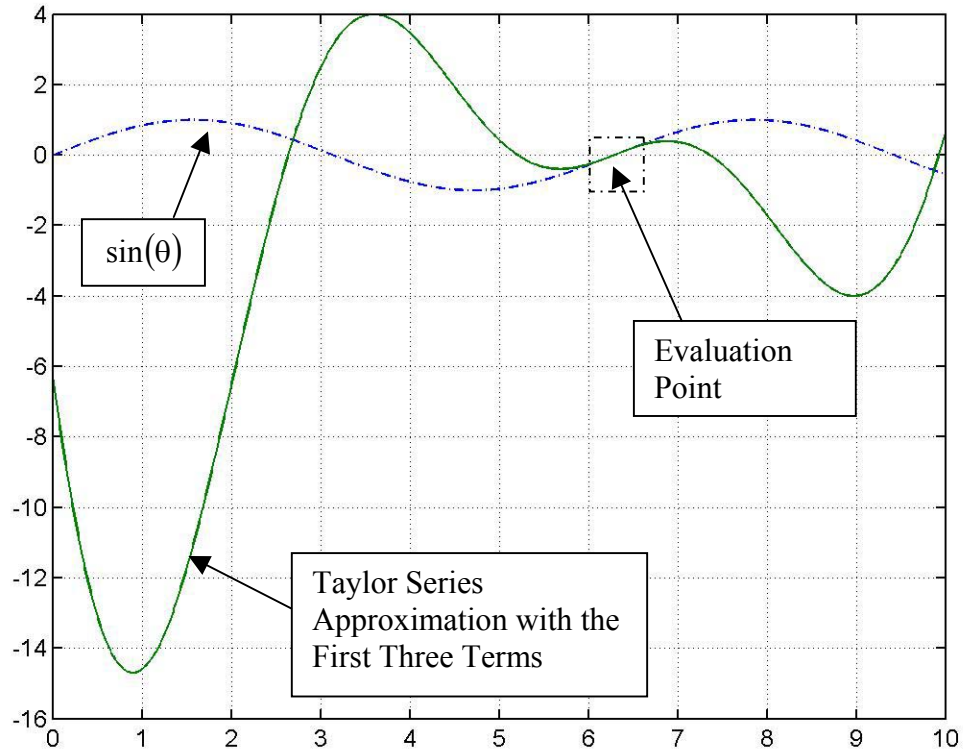
Figure 4.5: Comparison between sine function and 3-term Taylor series approximation

evaluated at $x = 2\pi$

4.2.2 Example with Beam Mode Shape

The sine function in Section 4.2.1 provides an example of a Taylor series approximation at a single point along a function. This section examines the more germane case of cantilever beam mode shapes approximated by a Taylor series at various points along the function. The second vibrational mode shape has been arbitrarily chosen for illustration.
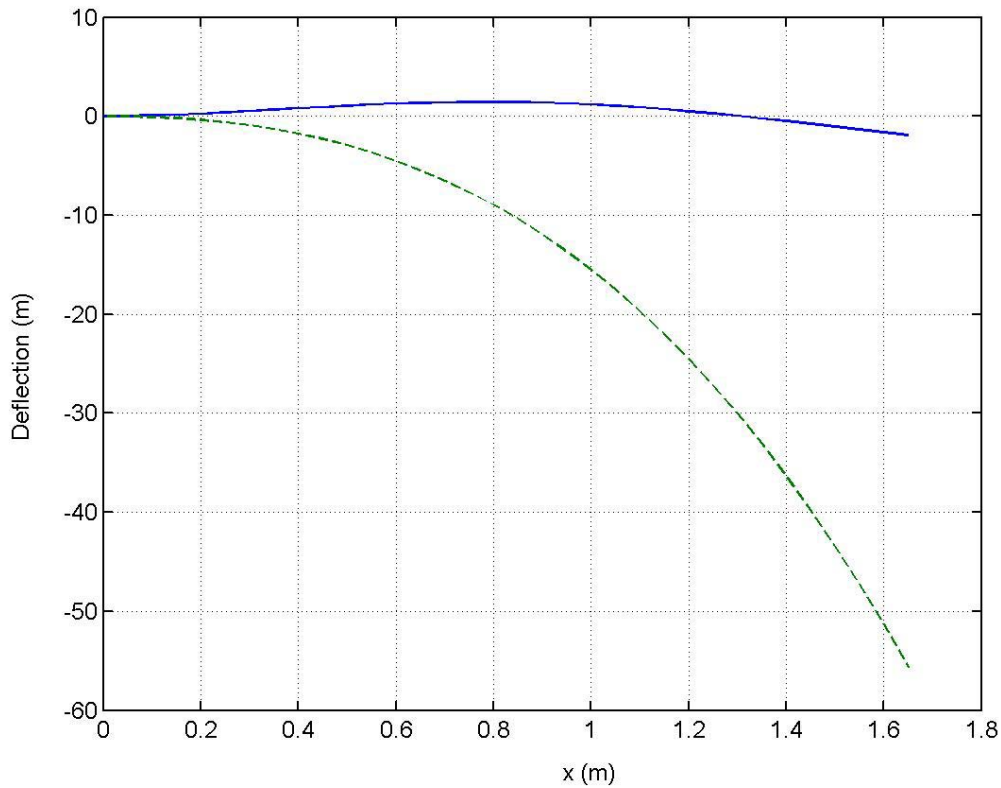
Figure 4.6: Taylor series approximation (--) of the mode 2 cantilever beam shape (—) at

location x = 0

As a start to the mode shape investigation, Figure 4.6 displays the Taylor series approximation of the mode 2 beam shape with a single evaluation point at the root of the beam (x = 0). The approximation, which uses only the first three terms, matches the mode shape for a short distance from the root of the beam. Following approximately 5% of the beam length the Taylor series approximation diverges from the mode shape. Therefore, multiple evaluation points are required to provide a better approximation along the beam length.
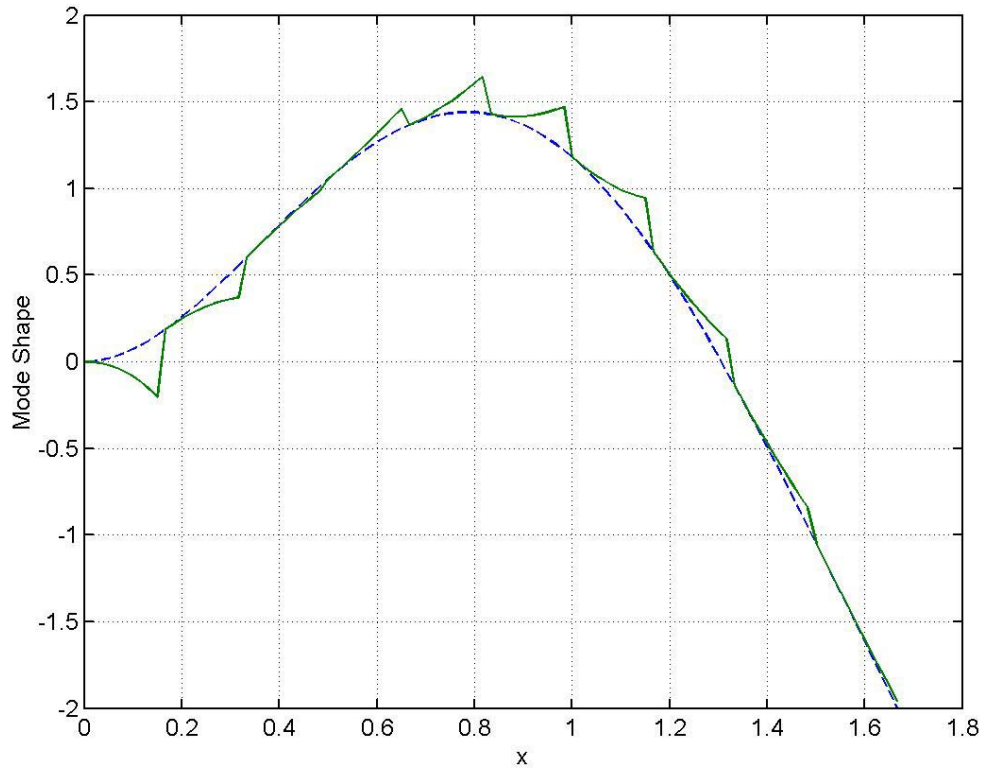
Figure 4.7: Taylor series approximation (——) of the mode 2 cantilever beam shape (--) at

10 locations along the beam length

Figure 4.7 displays the Taylor series approximation for the mode 2 shape with

10 points evaluated along the beam length. As in the previous case, the Taylor series

approximation quickly diverges from the mode shape at the root of the beam. At each

evaluation point, the Taylor series approximation matches the value of the mode shape

and then quickly diverges. The Taylor approximation matches the mode shape with

better accuracy where the derivative of the function is fairly constant; the first three

terms of the Taylor series include up to the second derivative of the mode shape

function. In regions that contain high rates of change of structure shape, the three-term

Taylor approximation quickly diverges from the shape function. Hence, an adequate number of evaluation points will be required for a low-order Taylor approximation to represent the mode shape. The mode 2 shape shown has a high amplitude deflection to illustrate the Taylor series effect.
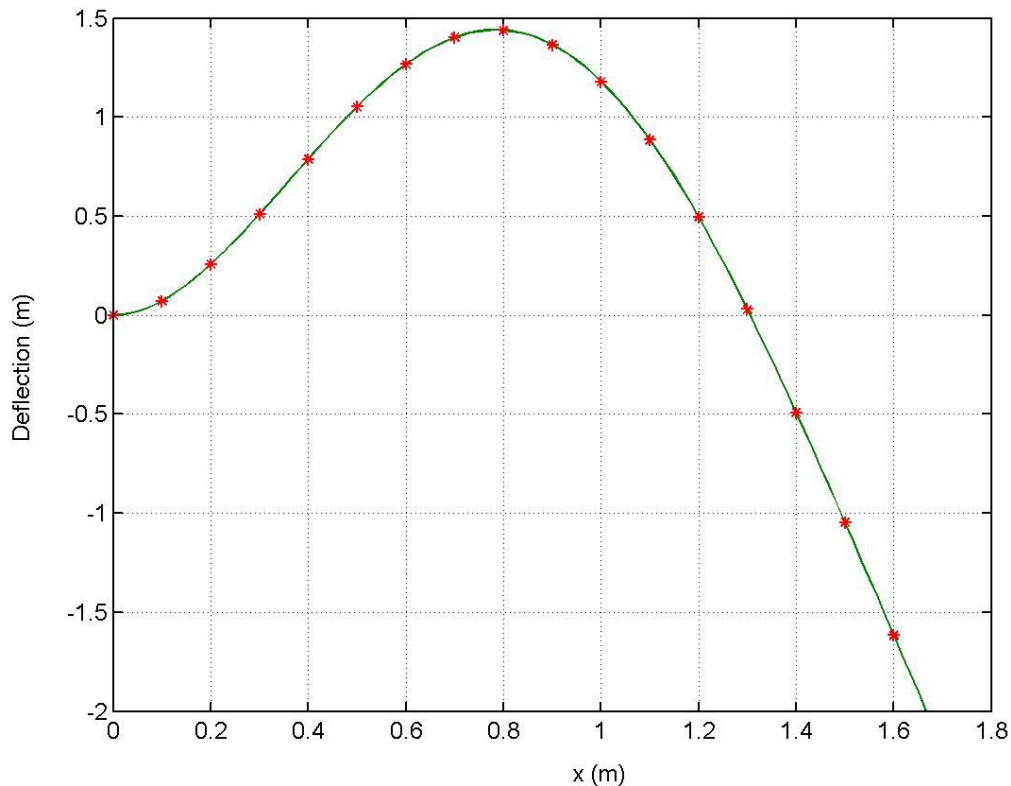
Figure 4.8: Taylor series approximation (—) of the mode 2 cantilever beam shape (*-) at 100 locations along beam length

Increasing the number of evaluation points to 100 along the beam length provides a very close match to the mode 2 shape function as shown in Figure 4.8. In the derivation of the shape algorithm in Section 3.2, the derivative of the Taylor series

expansion of the vector **R**(s) is used to determine the tangent (**T**) and normal (**N**)

vectors at each evaluation point. The tangent vector is then used to direct the algorithm

to the position of the next evaluation point. As will be discussed further in the next

section, increasing the number of points used in the shape algorithm improves the

accuracy of the algorithm.

4.3 Evaluation of the Number of Sensors

This section examines how the number of sensors along the length of the beam

affects the results of the shape algorithm. For the purpose of this analysis the number of

interpolation points between sensors is set to 9, segmenting the beam into 10 segments

between each sensor location and the cubic spline method (Section 3.3) is used in the

interpolation. The end of the beam is free and is assumed to have a strain value of zero.

The length of the beam for these simulations was chosen to be 65.625 inches (167 cm),

which is the length of the beam used in the experimental investigations discussed in

Chapter 5. The simulations discussed in this section assume that there is no random

sensor error.

4.3.1   One Sensor Case

With only one sensor, the sensor location must be at the root of the beam. A

strain reading is required at this location to "start" the shape calculation algorithm.

Additional data points are then interpolated between the root strain value and the beam tip. Shown in Figure 4.9, the comparison between the calculated and theoretical mode 1 shape with only one sensor appears to be in good agreement, with an error_{10} value of 0.0082. If the number of interpolation points is increased from 9 to 99 the error_{10} value remains 0.0082, indicating no change in the shape calculation compared to the theoretical mode shape.
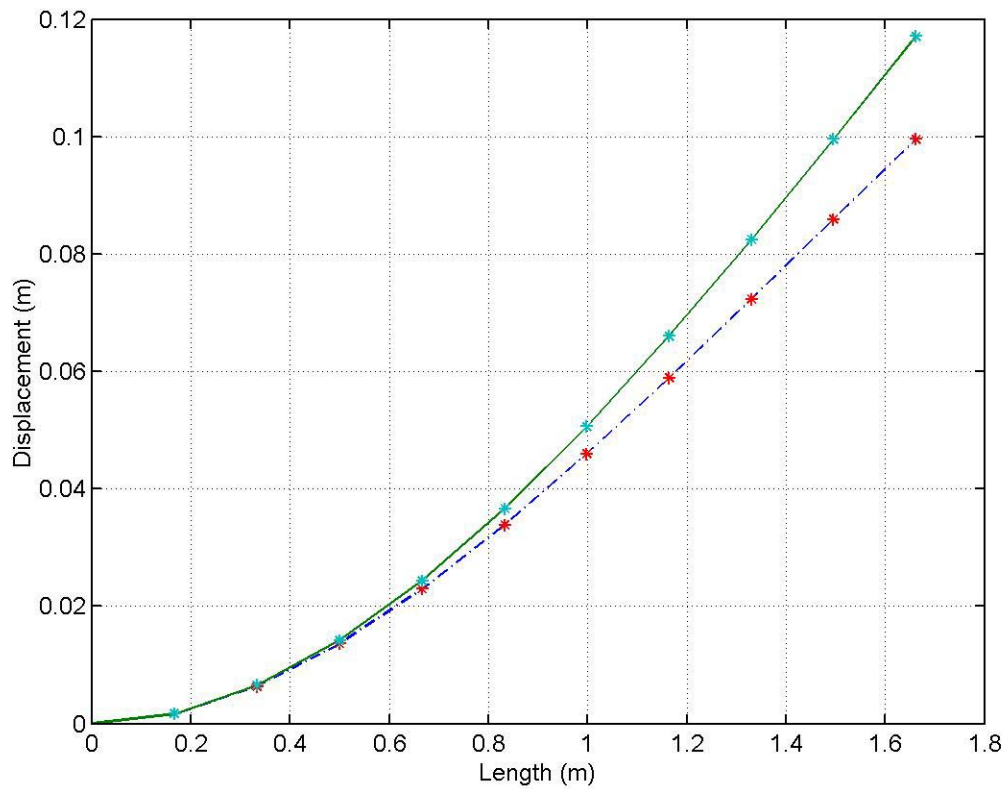
Figure 4.9: Mode 1 shape calculation (——) compared to analytical result (- -), one sensor

Figure 4.10 examines the case of one sensor at the root of the beam for a mode 2 shape. The asterisks in the figure represent the locations used to calculate the error_{10}

values. The calculated shape maintains the mode 1 shape because the only sensor data used to determine the shape is interpolated from the root strain value and the tip strain value (tip strain equal to zero). Hence, there is not enough information going to the algorithm to allow for the determination of the higher order mode. This concept will be highlighted in the examples in this section, where the algorithm can not determine a mode shape higher than the number of sensors used on the beam. This, of course, leads to a higher $error_{10}$ value of 0.1994, close to two orders of magnitude higher than the $error_{10}$ value for one sensor and mode 1 shape. A similar result is given for the mode 3 shape comparison leading to an $error_{10}$ value of 0.3593
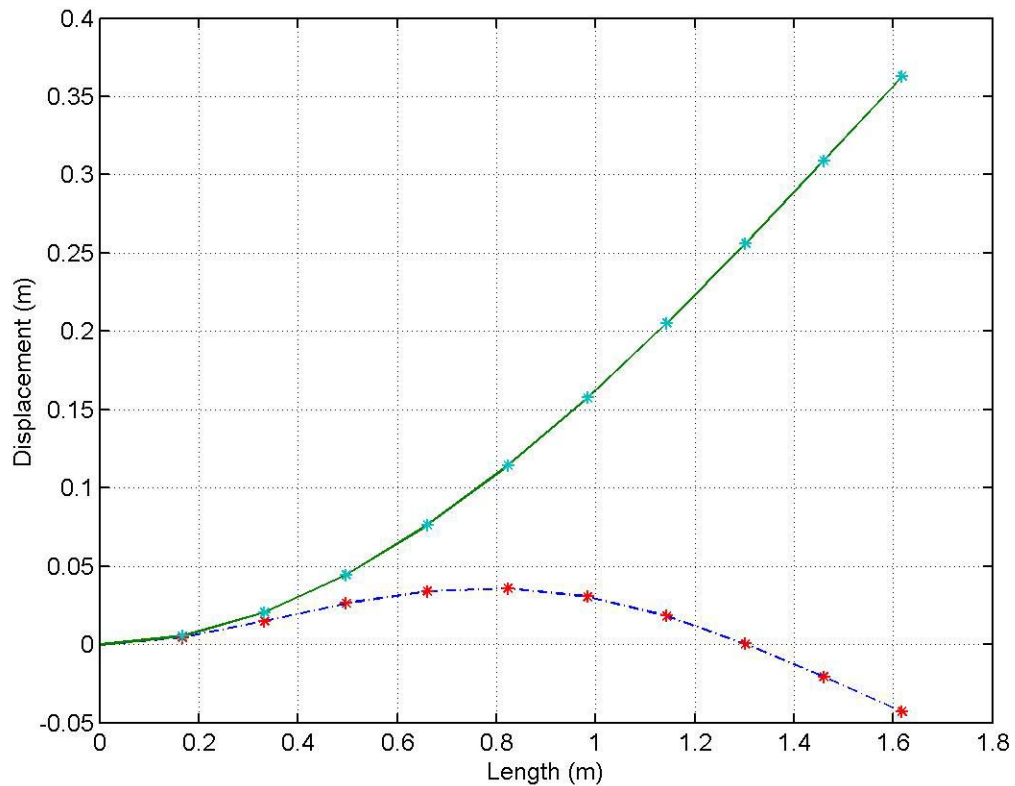
Figure 4.10: Mode 2 shape calculation (——) compared to analytical result (- -), one sensor

4.3.2 Two Sensors Case

The case with two sensors includes a sensor at the root of the beam and a sensor at the mid-span of the beam. The results from the mode 1 shape calculation are shown in Figure 4.11 based on 9 interpolation points between sensors. By increasing from one to two sensors the $error_{10}$ value is decreased to 0.0011. If the number of interpolation points is increased from 9 to 99 the $error_{10}$ value remains 0.0011. Interpolating more times between the data points does not improve the shape measurement accuracy for the case of a small number of sensors.
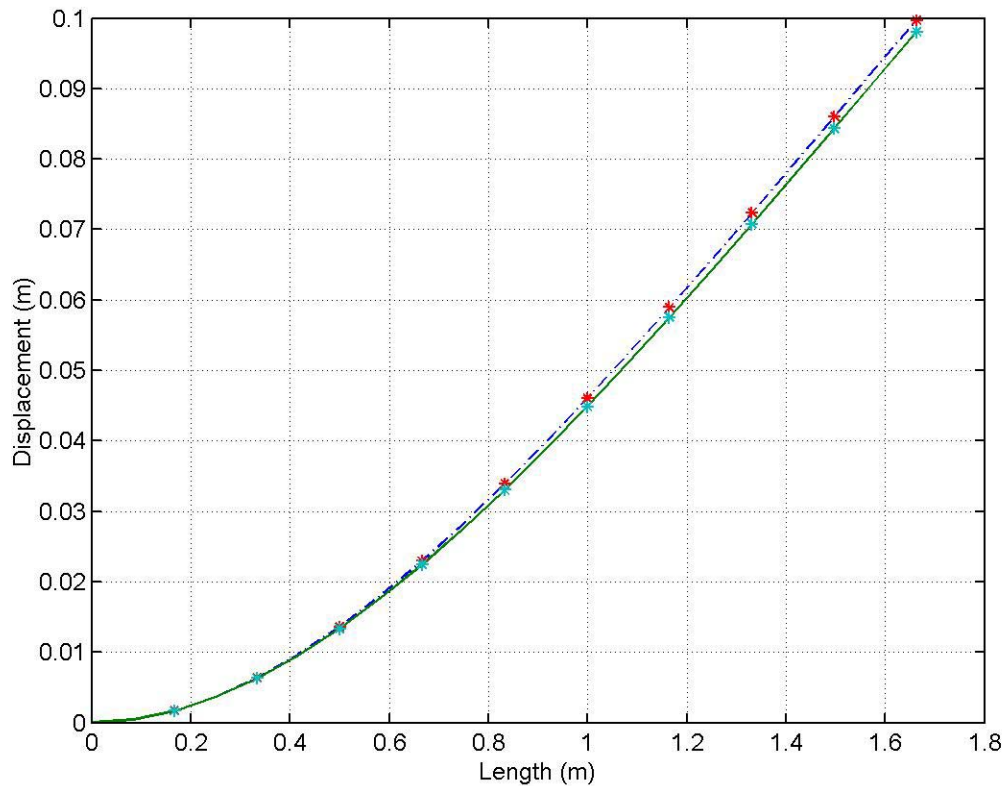
Figure 4.11: Mode 1 shape calculation (——) compared to analytical result (- -), two
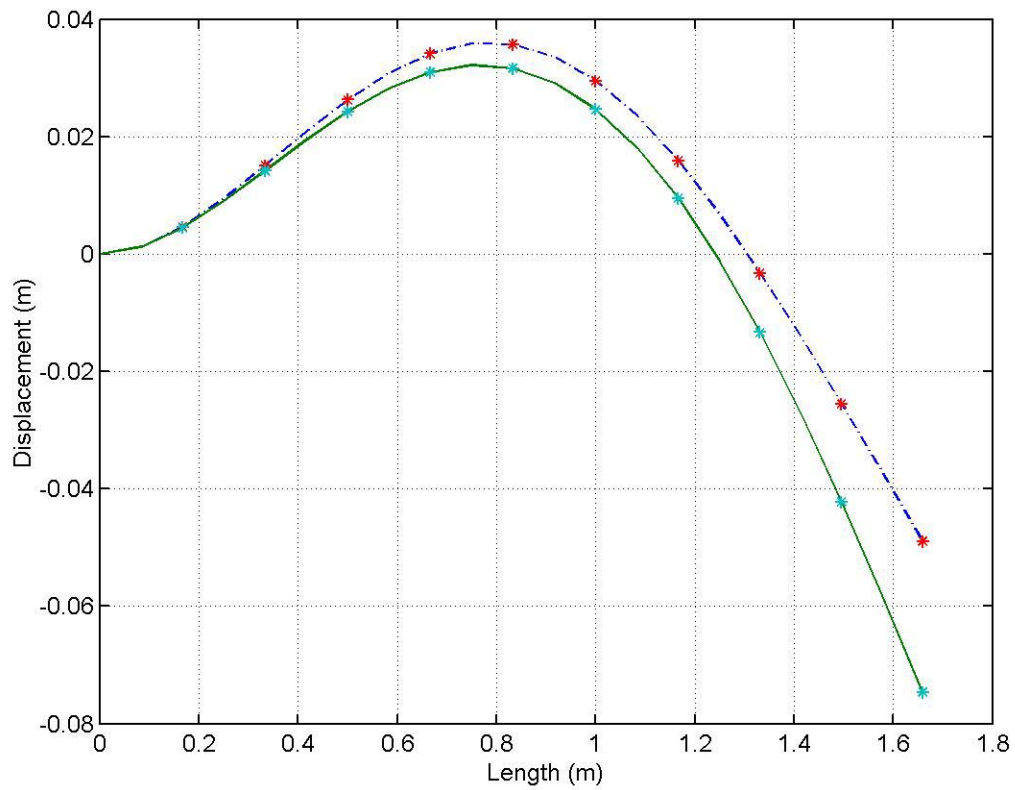
sensors

Figure 4.12: Mode 2 shape calculation (——) compared to analytical result (- -), two

sensors

For the mode 2 comparison, the shape measurement algorithm provides an

error$_{10}$ value of 0.0107. The shape comparison, shown in Figure 4.12, displays an

adequate representation of the mode 2 cantilever beam shape but does not match the

mode 2 shape precisely.

Figure 4.13 examines the case of a mode 3 beam shape with only two sensors.

Again, the limitation of requiring at least the same number of sensors as modes of

78

interest is seen. The midspan sensor for this case measures a strain of approximately

zero which leads to a curvature value of near zero. When the algorithm reaches the

center portion of the beam, the algorithm does not diverge because there is no value of

curvature to change the tangent direction; thus creating the mode 1 type deflection.
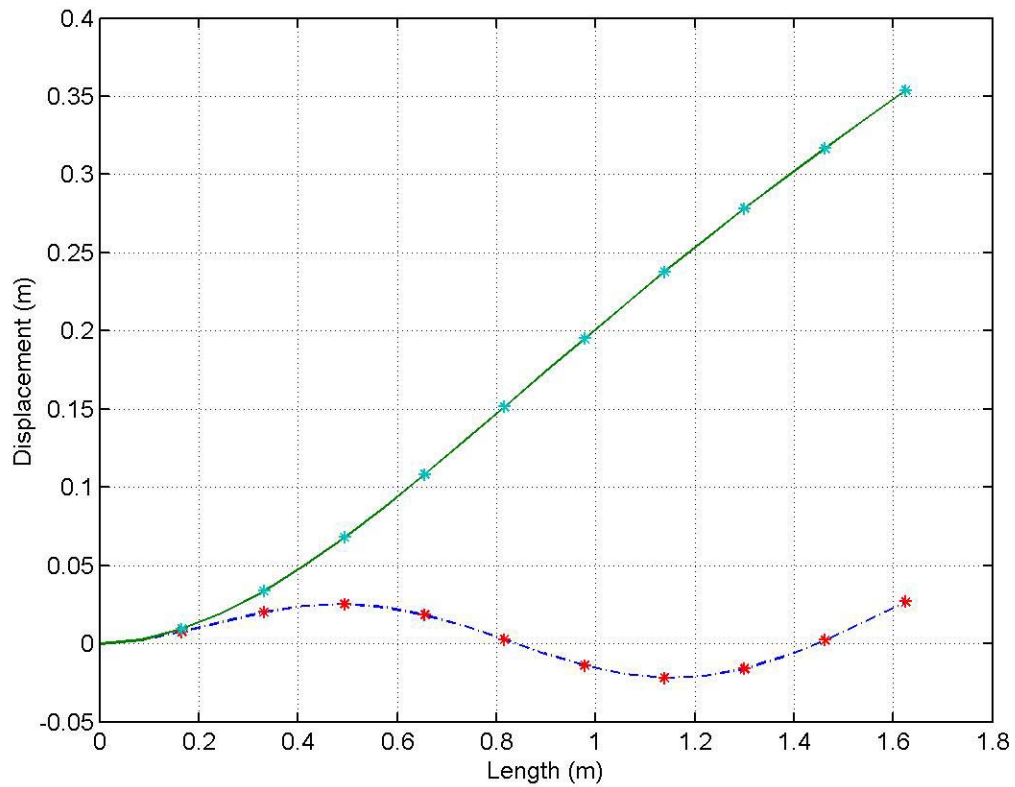
Figure 4.13: Mode 3 shape calculation (——) compared to analytical result (- -), two

sensors

4.3.3 Three Sensors Case

The previous two sections have shown that the shape algorithm can capture but not precisely model the mode shape equivalent to the number of sensors used to measure strain readings from the beam. The case of using three sensors also follows the same paradigm. When examining the case of mode 1, mode 2 and mode 3 shapes, as shown in Figure 4.14 through Figure 4.16, the error$_{10}$ values are found to be 4.68e-5, 0.0102, and 0.0615, respectively. The algorithm is unable to capture the mode 4 shape when using only three sensors, as shown in Figure 4.17.
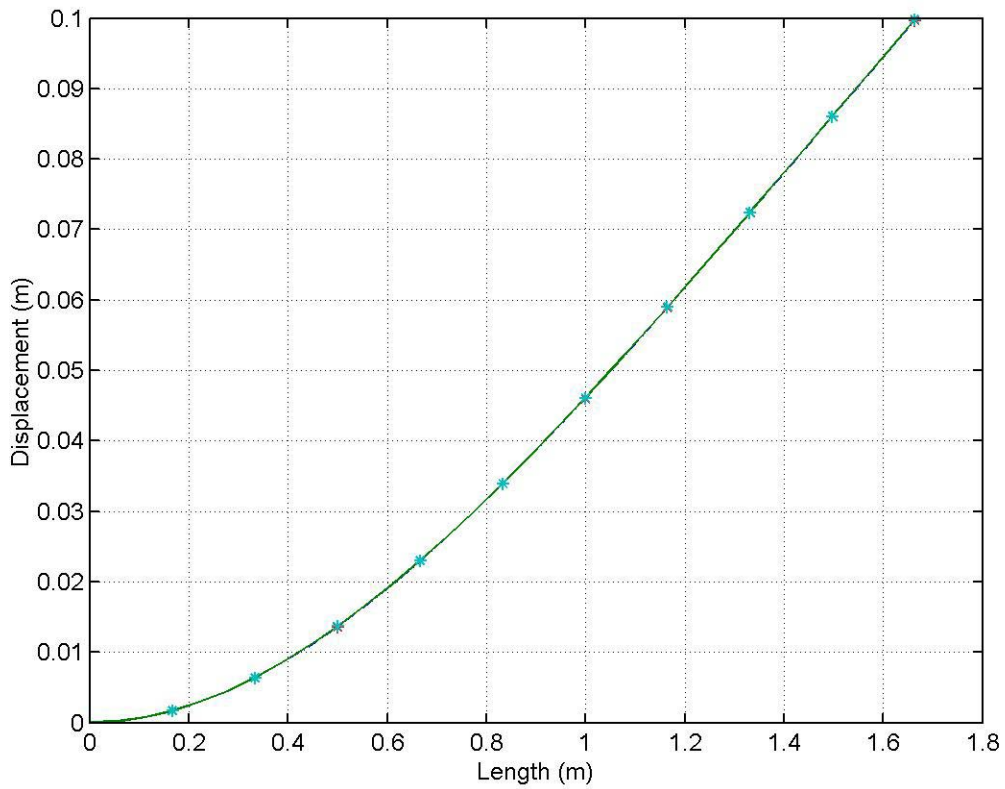
Figure 4.14: Mode 1 shape calculation (——) compared to analytical result (- -), three sensors
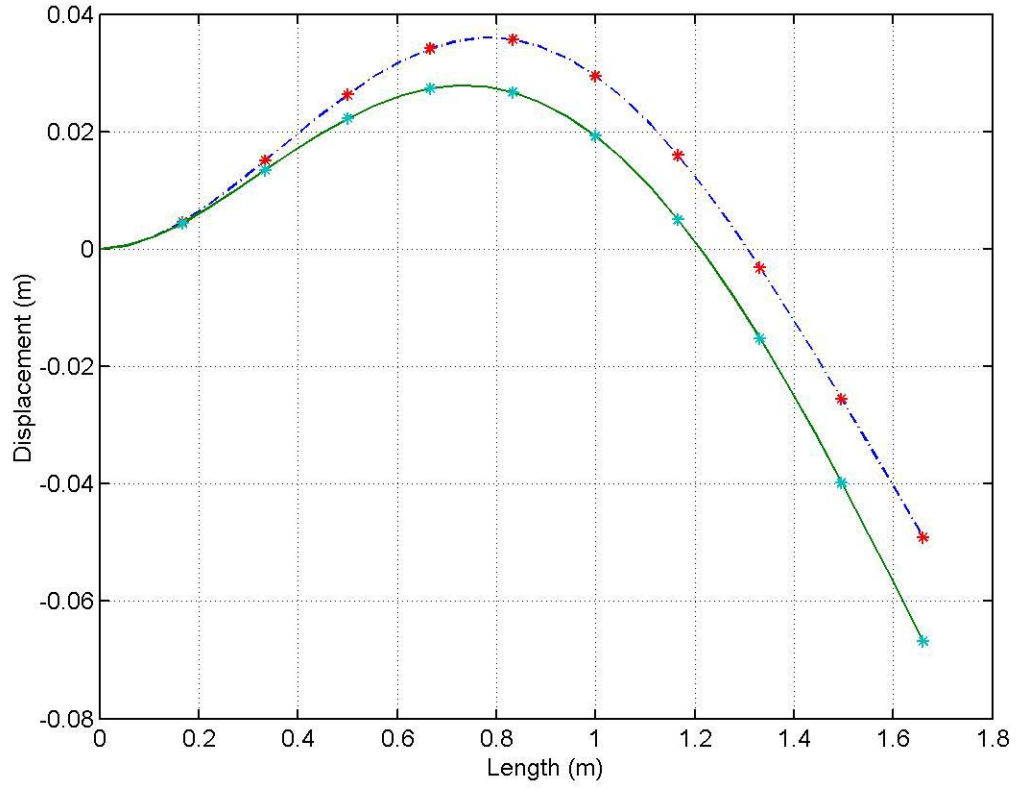
Figure 4.15: Mode 2 shape calculation (——) compared to analytical result (- -), three
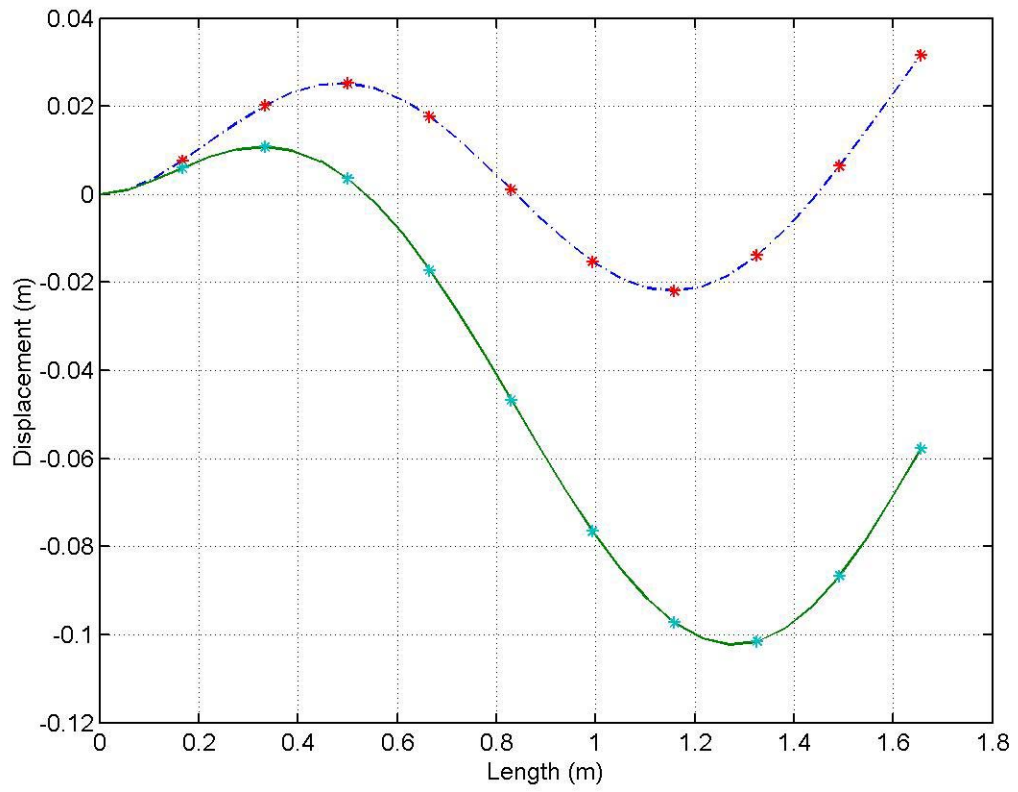
sensors

Figure 4.16: Mode 3 shape calculation (—) compared to analytical result (- -), three
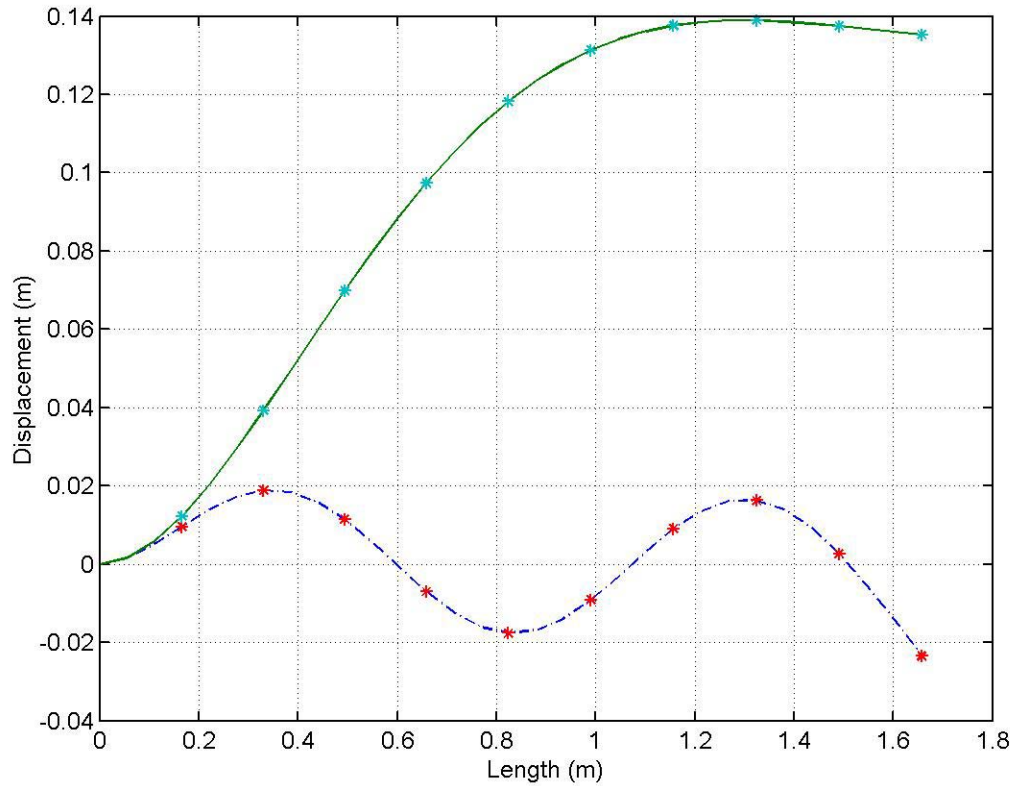
sensors

Figure 4.17: Mode 4 shape calculation (——) compared to analytical result (- -), three

sensors

4.3.4 Cases with more than 3 sensors

The analysis provided in the previous three sections could be continued until the

maximum mode shape number or allowable number of sensors is reached for a

particular application. In the interest of space, the analysis will now consider in general

terms the use of up to 9 sensors examining up to the first 8 mode shapes. Table 4.1 and

Table 4.2 provide the $error_{10}$ results for these examinations. As illustrated in the above

sections, the sensor algorithm does not adequately capture the mode shape for mode shape values greater than the number of sensors so these $error_{10}$ values are not included in the tables. The results in Table 4.1 are determined from using 9 interpolation points between sensor locations, while the results in Table 4.2 are determined from using 99 interpolation points between sensor locations. Comparing the results in the two tables generally shows an insignificant change between the use of 9 interpolation points compared to 99 interpolation points. In some cases, the $error_{10}$ value corresponding to 9 interpolation points is less than the 99 interpolation point value. This difference exists because the 10 values used to determine the $error_{10}$ value are slightly different between the 9 interpolation method and the 99 interpolation. The shape algorithm determines the x axis values as it progresses along the beam length. Therefore, different shape results will have different arrays of x axis values leading to the selection of slightly different values used for the $error_{10}$ calculation. Therefore, no conclusions can be drawn from the comparison between the 9 interpolation and 99 interpolation. Based on the error analysis in this section, a shape comparison to the theoretical will be considered accurate if the $error_{10}$ value is less than 0.001

	1 sensor	2 sensors	3 sensors	4 sensors	5 sensors	6 sensors	7 sensors	8 sensors	9 sensors
Mode 1	0.0082	0.0011	4.68E-05	1.04E-05	1.71E-05	2.01E-05	2.14E-05	2.21E-05	2.24E-05
Mode 2		0.0107	0.0102	1.53E-04	1.92E-04	6.50E-05	5.89E-05	6.69E-05	7.88E-05
Mode 3			0.0615	0.0334	0.0055	7.21E-04	7.17E-04	7.32E-04	5.65E-04
Mode 4				0.0951	0.0640	0.0202	0.0066	0.0017	4.22E-04
Mode 5					0.0321	0.0784	0.0224	0.0058	0.0036
Mode 6						0.0204	0.0992	0.056	0.0274
Mode 7							0.0669	0.1294	0.1024
Mode 8								0.085	0.1077

Table 4.1: $Error_{10}$ using 9 interpolation points between sensor locations

	1 sensor	2 sensors	3 sensors	4 sensors	5 sensors	6 sensors	7 sensors	8 sensors	9 sensors
Mode 1	0.0082	0.0011	4.29E-05	1.30E-05	1.91E-05	2.15E-05	2.24E-05	2.29E-05	2.31E-05
Mode 2		0.0123	0.0106	1.98E-04	8.56E-05	5.25E-05	8.53E-05	1.02E-04	1.09E-04
Mode 3			0.0640	0.0344	0.0063	0.001	4.12E-04	5.24E-04	4.39E-04
Mode 4				0.1076	0.0653	0.0214	0.0075	0.0024	5.75E-04
Mode 5					0.1177	0.0866	0.041	0.017	0.0073
Mode 6						0.1262	0.1061	0.064	0.0302
Mode 7							0.1226	0.1161	0.0785
Mode 8								0.1255	0.1276

Table 4.2: $Error_{10}$ using 99 interpolation points between sensor locations

4.4 Pearson Correlation Coefficient

The Pearson product moment correlation coefficient (r_P) is a dimensionless parameter that provides an indication of the linear dependence of two data sets. For the case of the shape algorithm, the two data sets are y_{exp} and y_{theory}. The Pearson coefficient is investigated in this section to provide a comparison to the $error_{10}$ value. If the two data sets being compared are indicated by X and Y and each contains n data points, then the Pearson coefficient is given as [Excel, 1997]:

$$r_P = \frac{n\left(\sum XY\right) - \left(\sum X\right)\left(\sum Y\right)}{\sqrt{\left[n\sum X^2 - \left(\sum X\right)^2\right]\left[n\sum Y^2 - \left(\sum Y\right)^2\right]}} \tag{4.3}$$

The Pearson coefficient provides a value between 1 and -1, with 1 meaning a linear relationship between the data and -1 meaning a negative linear relationship. To illustrate this fact, let Y be proportional to X by a constant C.

$$\{Y\} = C\{X\} \tag{4.4}$$

Substituting Equation 4.4 into Equation 4.3 leads to the following relation for C>0.

$$r_P = \frac{nC\left(\sum X^2\right) - C\left(\sum X\right)^2}{\sqrt{\left[n\sum X^2 - \left(\sum X\right)^2\right]\left[nC^2\sum X^2 - C^2\left(\sum X\right)^2\right]}} = \frac{nC\left(\sum X^2\right) - C\left(\sum X\right)^2}{nC\left(\sum X^2\right) - C\left(\sum X\right)^2} = 1 \tag{4.5}$$

If C<0 then $r_P = -1$.

The Pearson coefficient was calculated for the same cases as discussed in Section 4.3. Table 4.3 and Table 4.4 display the results for 9 interpolation points between sensors and 99 interpolation points between sensors, respectively. The values used for the Pearson coefficient calculation were the same 10 values used for the $error_{10}$

86

calculations shown in Table 4.1 and Table 4.2. The ineffectiveness of the Pearson coefficient for determining the accuracy of the shape algorithm results compared to the theoretical shape is illustrated by the mode 1 case with 2 sensors. The Pearson coefficient is 1 even though the comparison is not an accurate match as illustrated in Figure 4.11 with an $error_{10}$ value of 0.0011. The shape results are actually linearly dependent as indicated by the Pearson coefficient. The $error_{10}$ value provides a better indication of shape accuracy and is used throughout this dissertation.

	1 sensor	2 sensors	3 sensors	4 sensors	5 sensors	6 sensors	7 sensors	8 sensors	9 sensors
Mode 1	0.9995	1.0000	1.0000	1.0000	1.0000	1.0000	1.0000	1.0000	1.0000
Mode 2		0.9939	0.9900	1.0000	1.0000	1.0000	1.0000	1.0000	1.0000
Mode 3			0.6914	0.7932	0.9906	0.9999	0.9996	0.9996	0.9997
Mode 4				0.6269	0.6768	0.8953	0.7310	0.9984	0.9996
Mode 5					0.5932	0.3606	0.4778	0.9330	0.9889
Mode 6						0.7413	0.2483	0.5770	0.6914
Mode 7							0.4381	0.1969	0.1869
Mode 8								0.3426	0.2750

Table 4.3: Pearson Coefficient using 9 interpolation points between sensor locations

	1 sensor	2 sensors	3 sensors	4 sensors	5 sensors	6 sensors	7 sensors	8 sensors	9 sensors
Mode 1	0.9995	1.0000	1.0000	1.0000	1.0000	1.0000	1.0000	1.0000	1.0000
Mode 2		0.9924	0.9893	1.0000	1.0000	1.0000	1.0000	1.0000	1.0000
Mode 3			0.6828	0.9874	0.9874	0.9998	0.9998	0.9998	0.9998
Mode 4				0.6732	0.6732	0.8863	0.9756	0.9968	0.9996
Mode 5					0.3201	0.3317	0.5263	0.8198	0.9568
Mode 6						0.4337	0.4626	0.5490	0.7263
Mode 7							0.1854	0.1718	0.2122
Mode 8								0.3552	0.3532

Table 4.4: Pearson Coefficient using 99 interpolation points between sensor locations

5 Experimental Setup for Shape Measurement Validation

To validate the shape measurement algorithm a well-understood mechanical

system was chosen. The aluminum cantilever beam model provides a linear

deformation with well-known deformation shapes in the form of mode shapes. The

experiments discussed in this dissertation represent the first known successful

implementation of the Serret-Frenet shape algorithm discussed in Chapter 3. This

chapter provides an overview of the experimental setup employed for the investigation,

as well as the data collection methodology and post processing of the data prior to

implementation of the shape algorithm.

5.1 Experimental Setup

A cantilever aluminum structure was tested to demonstrate the concept of

measurement and analysis of dynamic deformations (mode shapes) of flexible

structures. An 6061 aluminum structure (65.625 $\times$ 2.0 $\times$ 0.125 inches,

166.69$\times$5.08$\times$0.32 cm) was fitted with eight fiber Bragg grating (FBG) sensors along its

span, used to determine the strain along the span during the experimentation. The

sensors were positioned along the centerline of the structure as depicted in Figure 5.1

and Figure 5.2. The sensors were glued to the structure using AE-10 epoxy, from

Measurement Group Inc. (www.vishay.com), following standard room temperature

curing procedures.
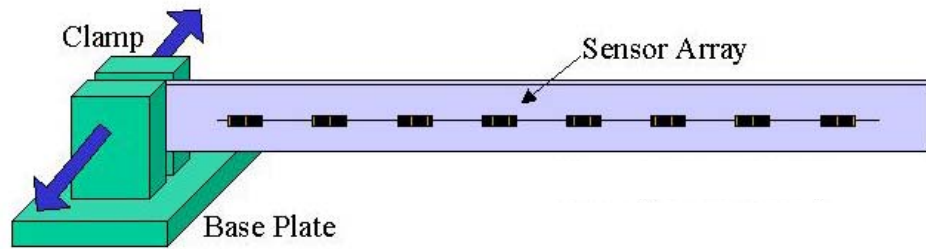
Figure 5.1: Base excitation – cantilever structure setup

Figure 5.2: Picture of cantilever structure (base excitation not shown)

The eight FBG sensors were evenly spaced at 7.65 inches (19.43 cm) along the

length of the structure, providing a uniform distribution of the FBG sensors along the

span. The spacing between the eighth FBG sensor and the tip of the structure was 10.8

inches (27.43 cm). The extra space resulted from an accidental break of the optical

fiber after bonding of the sensors but prior to testing; to solve this problem the

cantilever structured was turned around such that what was initially the root end of the structure became the tip of the structure. The extra 3.15 inches (8 cm) represents the amount of the structure that would have been enclosed in the clamping fixture as pictured in Figure 5.2. For most of the test cases, the strain variation in this region is considered negligible as the strain decreases to zero at the tip of the structure. The exact spacing of the eight FBG sensors is listed in Table 5.1.

Sensor Number	Distance from Base of Structure (inches)
FBG 1	1.25
FBG 2	8.90
FBG 3	16.55
FBG 4	24.20
FBG 5	31.86
FBG 6	39.51
FBG 7	47.16
FBG 8	54.82

Table 5.1: FBG sensor spacing from base of cantilever structure

An intensity plot of the eight unstrained FBG sensors is shown in Figure 5.3 illustrating the recorded intensity from the CMOS imager used in the DSWDM instrumentation. Hence, the abscissa (x-axis) represents the pixel number along a single row of the CMOS imager, and the ordinate (y-axis) represents the intensity value (0 to 255) for that pixel. As shown, each FBG sensor is centered about a separate

wavelength (or pixel number). This allows for each sensor to be serially multiplexed

using the DSWDM system as discussed in Chapter 2. Also discussed in Chapter 2, the

wavelength (or pixel spacing) between the sensors is adequate to ensure no crosstalk or

interference between neighboring FBG sensors.
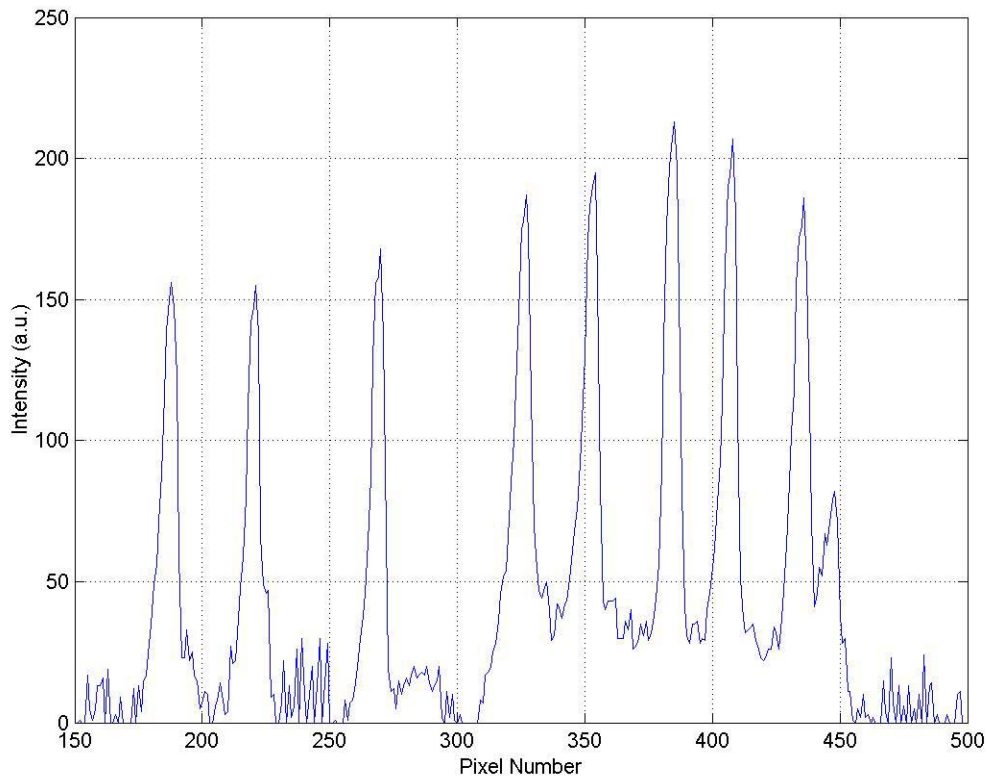
Figure 5.3: CMOS intensity plot of the multiplexed FBG sensors

The aluminum structure was excited in the horizontal plane using a shaker at the

base of the stricture. This allowed the free end of the structure to remain free and

experience the maximum deflection. During the testing cycle, an attempt was made to

visually measure the tip deflection (peak-to-peak) value of the cantilever structure using

a standard meter stick placed beneath the beam tip. Both the accuracy and resolution of

92

this methodology is poor (on the order of ± 1 cm), and the measurements taken in this fashion are only to provide rough measurement of the actual structural deformation.

Figure 5.4 displays a schematic of the experimental setup used to monitor the vibrational mode shapes of the cantilever structure. A function generator created a sinusoidal excitation, which was amplified and passed to the shaker. The cantilever structure was clamped to a linear translation stage to allow motion in the direction transverse to the structure base, as shown in Figure 5.5. The excitation frequencies were selected to match the resonant frequencies for the cantilever structure. The experimental process is described in detail in Section 5.2. The optical fiber lead exited the cantilever structure at the root. This region experiences the minimum deflection during the test and was chosen as the best option for the egress of the lead line from the cantilever structure. The first sensor was placed at a distance of 1.25 inches from the base of the structure/clamp interface in order to minimize the attenuation that could otherwise result from tightly bending the optical fiber at the clamp.
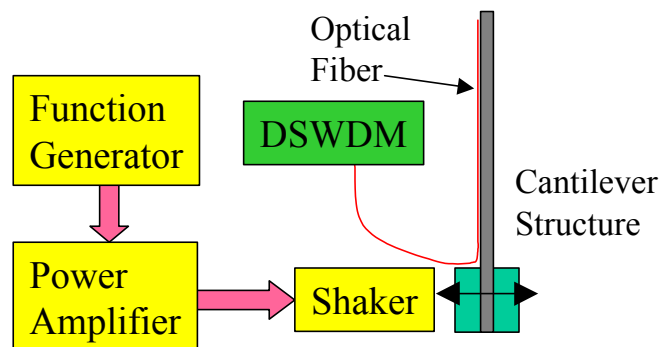
Figure 5.4: Experimental setup

93
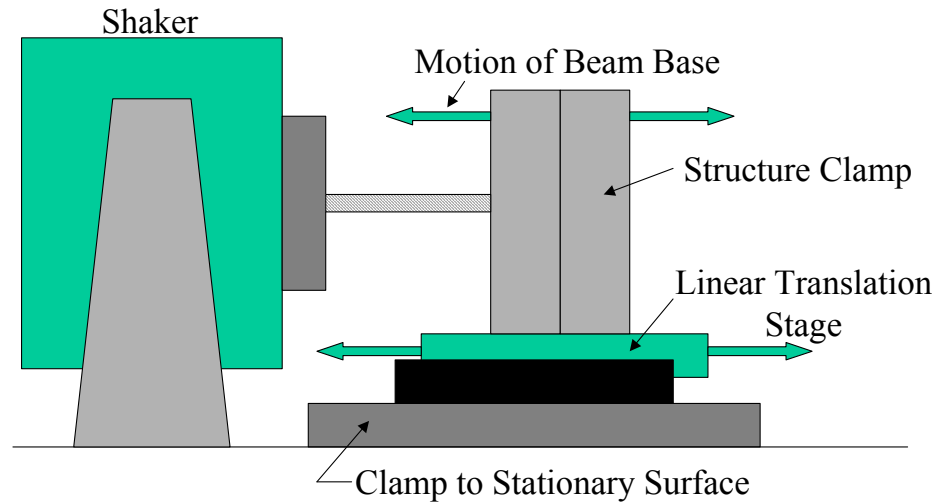
Figure 5.5: Linear motion of structure base setup

5.2 Strain Data Collection

Each test began with a check of the linear translation stage to ensure that it was able to slide freely and that all components were tightly bolted down. A vibration mode for the cantilever structure was selected and this frequency was programmed into the sinusoidal function generator. The gain on the power amplifier was set to a minimal level to ensure that the shaker and structure system was not overdriven. As the actuation system was powered on, the gain on the power amplifier was slowly increased until an adequate vibration deflection was reached based on the tip deflection. If necessary, the frequency of the function generator was shifted slightly to obtain a visually "clean" vibration state. Table 5.2 displays the observed resonant frequencies for the cantilever structure modeled as a beam. The goal of the test was to excite a single resonant mode of vibration for the cantilever beam structure. The structure was

allowed to vibrate in this state for several minutes to ensure that all transient vibrations

had died away. Strain data was then collected from the eight FBG sensors

simultaneously using the DSWDM instrumentation. The data collection typically lasted

for 30 seconds. The tip deflection of the vibrating cantilever structure was also

measured using a meter stick.

Mode Number	Observed Resonant Frequency (Hz)
1	1
2	6
3	17
4	33
5	56
6	82
7	115

Table 5.2: List of observed resonant frequencies

The DSWDM instrumentation generates data files that contain the time, the

sensor name, the centroid value of the sensor, and the corresponding strain value.

Shown in Table 5.3 is an example of the data file structure taken from a test of the

cantilever structure in the mode 3 resonant state. The data shown is truncated to show 2

out of the 8 sensors. The left most column is the time in seconds. The columns

containing the sensor names are 1-chris and 2-chris. The two columns following the

sensor names are the centroid value and strain value for the sensor, respectively. These

data files are tab delimited and are easily read into data processing programs such as

Excel and MATLAB. All post-processing of the experimental data was performed in

MATLAB.

Time	Sensor Name	Centroid	Strain (με)	Sensor Name	Centroid	Strain (με)	
0.060354	1-chris	176.5763	82	2-chris	209.7714	95	…
0.060874	1-chris	176.5528	78	2-chris	209.7972	100	…
0.061394	1-chris	176.5277	73	2-chris	209.787	98	…
0.061915	1-chris	176.5415	75	2-chris	209.7689	94	…
0.062435	1-chris	176.5522	77	2-chris	209.7689	94	…
0.062955	1-chris	176.5259	73	2-chris	209.7416	90	…
0.063476	1-chris	176.4915	66	2-chris	209.7418	90	…
0.063996	1-chris	176.483	65	2-chris	209.7048	83	…
0.064516	1-chris	176.4825	65	2-chris	209.7089	84	…
0.065036	1-chris	176.4658	62	2-chris	209.6667	76	…
0.065557	1-chris	176.4391	57	2-chris	209.6381	71	…
0.066077	1-chris	176.4386	57	2-chris	209.625	68	…
0.066597	1-chris	176.4079	51	2-chris	209.5735	59	…
0.067118	1-chris	176.4089	51	2-chris	209.5512	55	…
0.067638	1-chris	176.4141	52	2-chris	209.532	52	…

Table 5.3: DSWDM data file example

The data was collected from all eight FBG sensors on one optical channel

simultaneously, allowing the DSWDM to sample the data at the maximum frequency of

1928 Hz for all tests. The sampling frequency is limited by the speed of the frame grabber card that collects data from the CMOS imager and transmits it to the computer system.

5.3 Post Processing

The shape determination algorithm requires a strain reading at the root of the structure. Without this value, the shape determination algorithm would begin at the first sensor reading at 1.25 inches (3.2 cm) from the root. This would incur an unacceptable level of error, especially given that this is the region of the highest strain gradients. Therefore, strain values must be interpolated between the root of the beam and the second sensor location. To accomplish this, the value of the root strain is estimated from the first FBG sensor. Based on theoretical strain determination (discussed in Chapter 3), the root strain should be slightly higher than the strain recorded at the first sensor. The values shown in Table 5.4, determined from theory, were used to multiply the strain reading of the first sensor to obtain an estimate for the root strain.

Mode	Multiplication Value
1	1.026
2	1.100
3	1.176
4	1.264

Table 5.4: Multiplication values for the first FBG sensor to estimate the root strain

Chapter 6 and Chapter 7 cover analysis of the data collected during these tests. Chapter 6 shows the results of processing the data with the shape determination algorithm discussed in Chapter 3. This process involved taking the recorded strain data from a time of maximum deflection (and hence maximum strain) and processing the data at this one time through the shape determination algorithm. As will be shown, the resulting experimental shape compares well qualitatively with the expected mode shape, but significant differences between the experimental and theoretical mode shapes were observed, especially at higher order mode shapes. Fourier transforms of the strain data for these tests indicated that more than one modal response was influencing the cantilever beam during the testing. Chapter 7 then investigates the influence of the extraneous resonant modes on the cantilever beam. In this chapter, modal analysis techniques are employed that allow for the determination of modal influence coefficients for the many resonant modes of the cantilever beam. It will be shown that the beam shape determined from the experimental data and the shape determination algorithm matches the theoretical beam shape based on the determined modal analysis coefficients.

6 Shape Determination from Experimental Data

The following sections describe the data analysis for the first five mode shapes of the cantilever structure. Data was recorded up through the seventh resonant mode of the structure. The graphs for mode 6 and mode 7 are presented in Appendix B. The graphs for shape comparison display a reference mode shape (based on a single mode assumption) derived from the analysis in Chapter 3 using the maximum tip deflection visually recorded during the experiment as a basis for setting the amplitude. The experimental shape refers to the shape obtained from the Serret-Frenet algorithm by using the recorded strain values from the cantilever structure. For each case, the interpolated values for curvature are given along with the location of the FBG sensors. The time trace for the first sensor along the structure (nearest the root) is presented as well. Fast Fourier Transforms (FFTs) for selected strain data recorded from the FBG sensors are also presented. The FFTs are used to explain discrepancies between the theoretical and experimental shapes. Based on the FFT results, it appears that neighboring vibration modes are affecting the recorded strain data and hence the experimentally determined shape. This will be analyzed further in Chapter 7 using modal analysis techniques.

6.1 Mode 1 Testing: Excitation Frequency Close to the First Natural Frequency

Testing of the cantilever structure setup for mode 1 deflections consisted of actuating the base of the structure using the shaker as shown in Figure 5.5. The structure was excited near the first resonant frequency of ~1 Hz. Strain data for the eight FBG sensors was recorded at a sampling rate of ~1928 Hz , more than adequate for this low frequency vibration. During the test, the tip displacement of the structure was measured visually for comparative analysis. Using the tip deflection the theoretical mode 1 shape can be closely approximated using the analysis discussed in Section 3.1. Figure 6.1 displays the reference shape for mode 1 and the experimental shape obtained from the recorded strain data. The experimentally determined shapes, shown throughout this chapter, are from a selection of data at one instance of time (corresponding to a maximum amplitude of deflection).
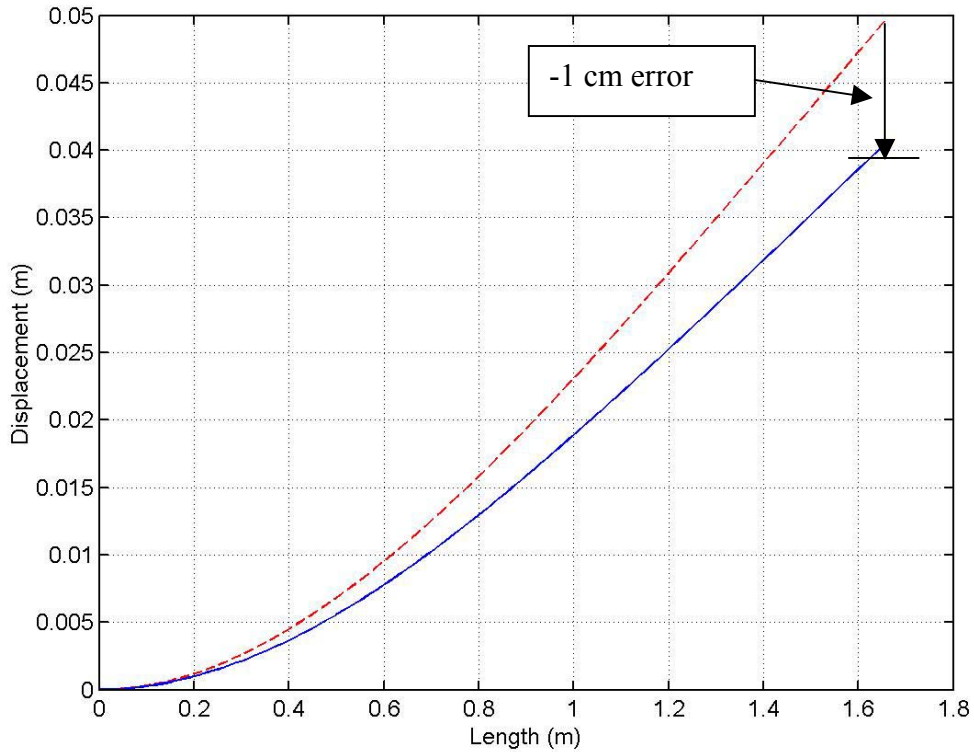
Figure 6.1: Mode 1 reference mode shape (--) and experimental shape (—) at a

maximum deflection point

The comparison of the tip deflection between the reference and experimental

shapes is within 1 cm of each other, as seen in Figure 6.1. Reasons for this discrepancy

include the method of measuring the tip deflection and noise in the recorded strain data.

The $error_{10}$ value for the comparison is 0.005, which indicates an inaccurate match

according to the $error_{10}$ value criteria.
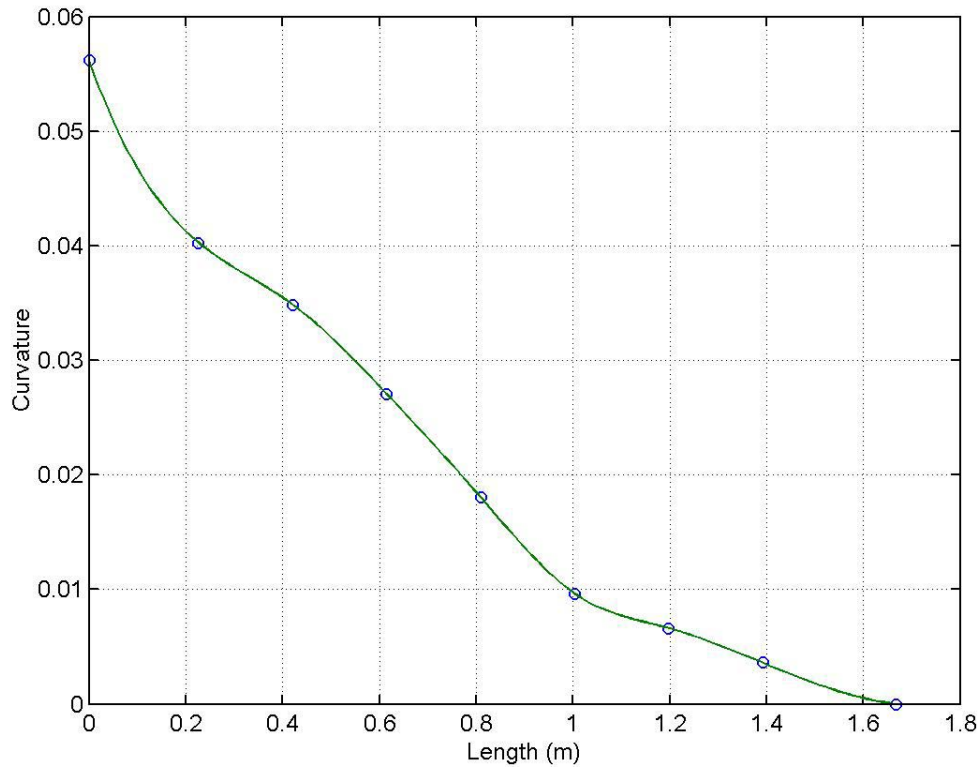
Figure 6.2: Mode 1 curvature data and positions of FBG sensors (O)

Examining the curvature data in Figure 6.2, the curvature values obtained at each of the sensor locations form an approximately linear relationship along the structure length, as expected for a mode 1 deflection of a cantilever beam. Note, there is no sensor at the tip of the structure and the data point located there is based on the assumption of zero strain and hence zero curvature. The sensor located at the root of the structure is the extrapolated strain value based on the first sensor located at 1.25 in (3.2 cm) from the root.
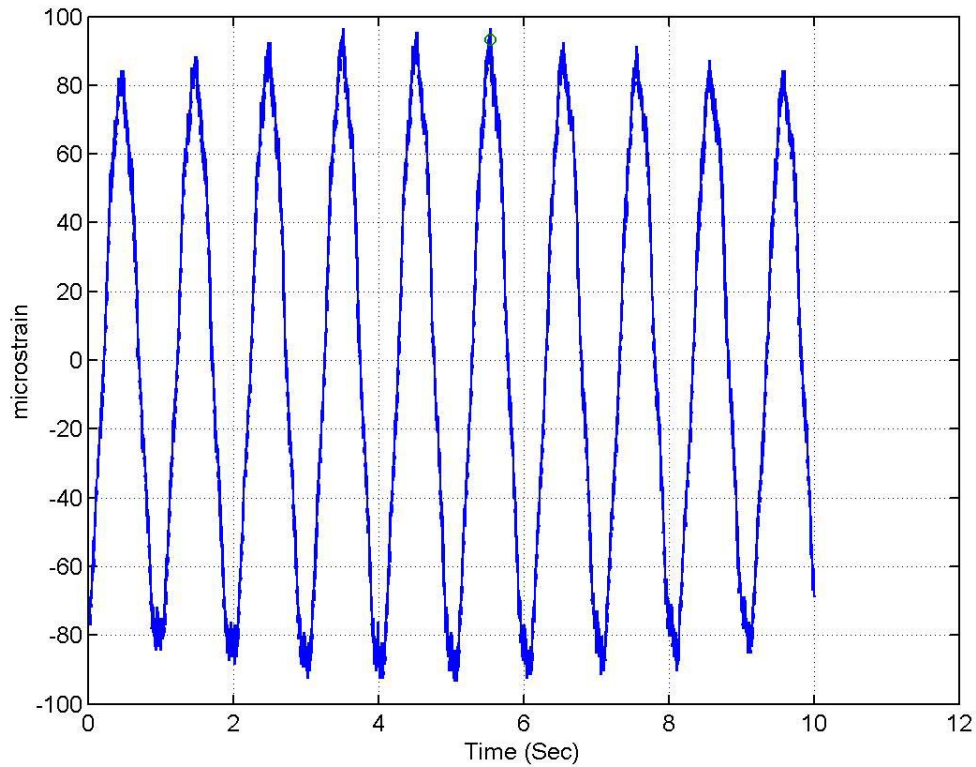
Figure 6.3: Time trace for a FBG sensor during mode 1 excitation

Ten seconds of strain data collected for sensor 1 of the mode 1 excitation is shown in Figure 6.3. Some higher frequency noise exists in this data that affects the overall accuracy of the calculated results. The FFTs of the sensor data displayed in Figure 6.4 and Figure 6.5 show a strong sensor response at approximately 1 Hz. There are also spikes in the FFT plots at 6 Hz, 17 Hz, and 32 Hz corresponding to the second, third, and fourth modal frequencies of the beam, respectively. These higher order vibrations were clearly evident when the amplitude of vibration was increased during the testing of the mode 1 response. The higher the amplitude of the input excitation the more evident these vibrations became. Strain data for each test was only recorded when the beam was vibrating in a visually stable single mode state.

103
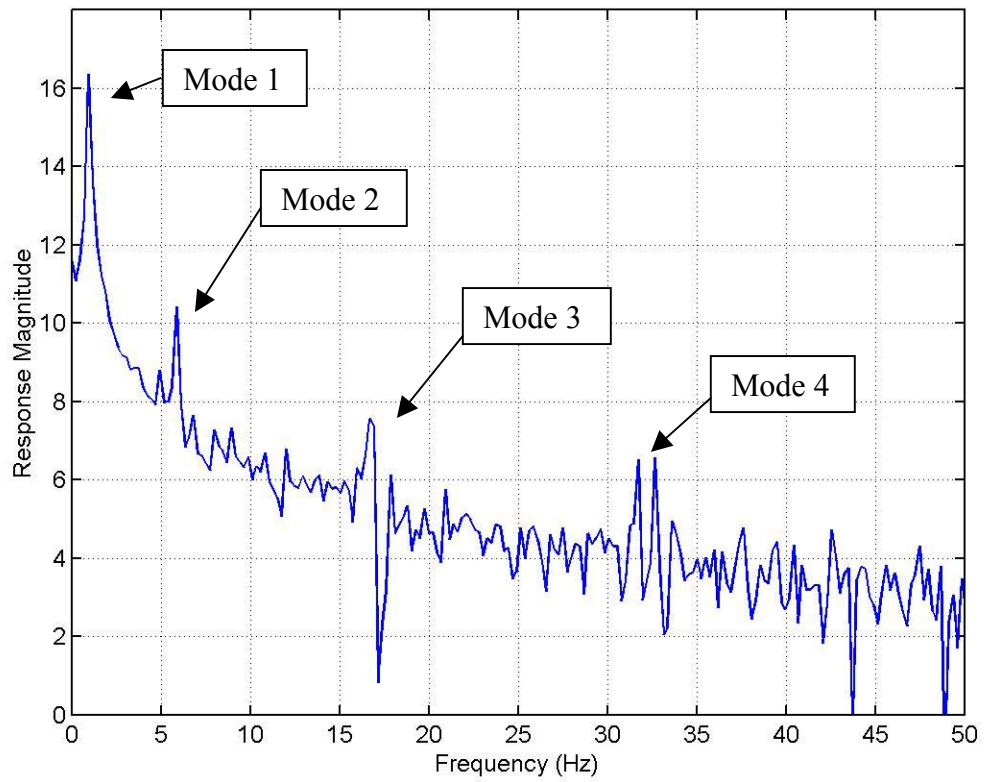
Figure 6.4: FFT plot for sensor #1 (mode 1 excitation)
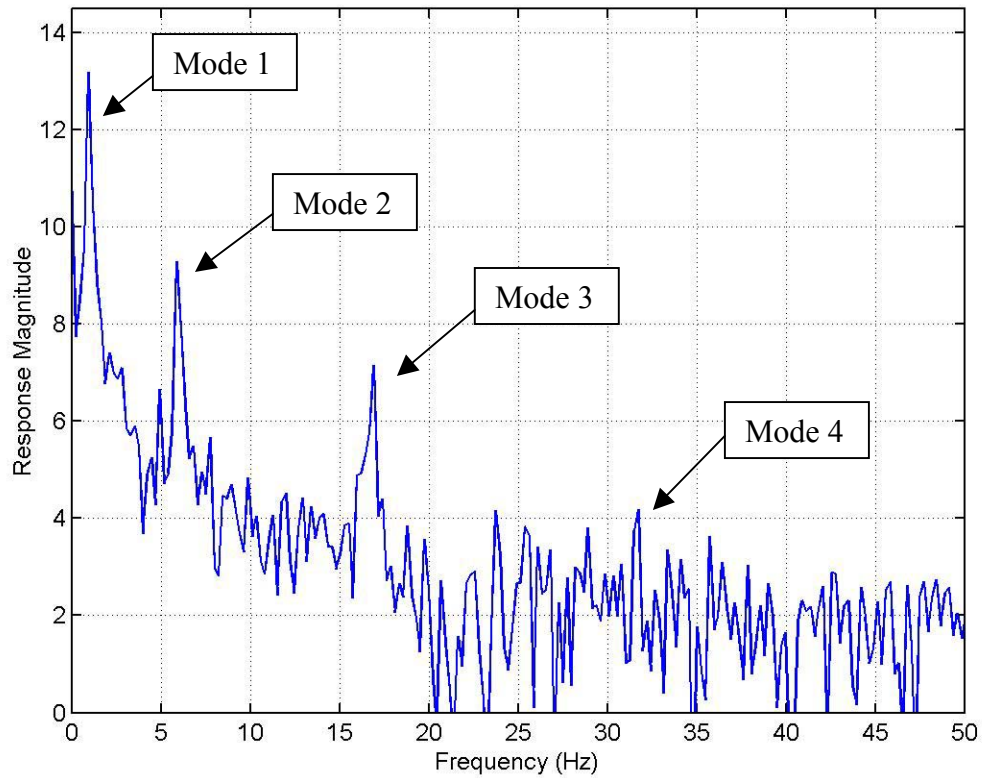
Figure 6.5: FFT plot for sensor #6 (mode 1 excitation)

6.2 Mode 2 Testing: Excitation Frequency Close to the Second Natural Frequency

Figure 6.6 displays the comparison between the mode 2 reference shape and the experimentally determined shape at a time of maximum deflection. The visually determined tip deflection and the mode 2 experimental tip prediction are within 3 mm of each other. This is approximately a factor of 3 better than the mode 1 approximation of the tip displacement. However, the discrepancy between the reference and experimental shape can clearly be seen at the mid-span of the beam length. Therefore,

using tip displacement alone is not a valid measurand to compare the accuracy of the shape determination method. The $error_{10}$ value determined for this comparison is equal to 0.006, which indicates that the comparison is not an accurate match according to the criteria established in Chapter 4.
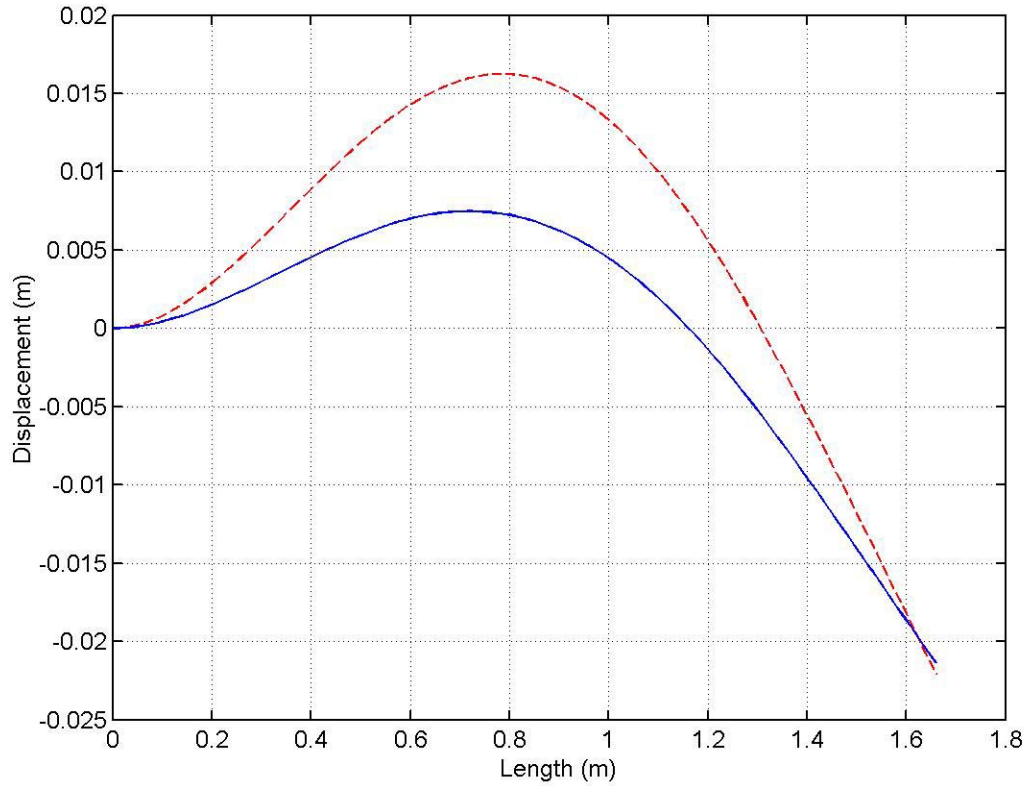
Figure 6.6: Mode 2 reference mode shape (--) and experimental shape (—) at a maximum deflection point
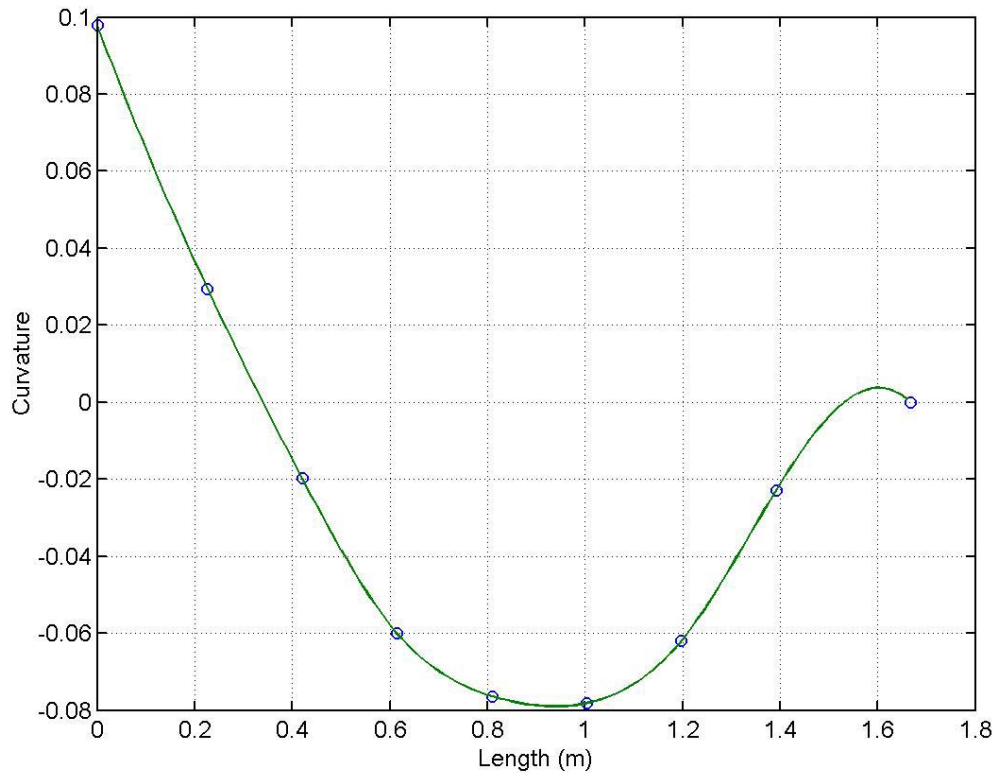
Figure 6.7: Mode 2 curvature data and positions of FBG sensors

The curvature data obtained for the mode 2 experiment is shown in Figure 6.7. A point of interest appears at the tip of the beam where the curvature goes from negative to positive before returning to zero at the tip, a result of the interpolation of values between the eighth sensor and the tip of the structure. The result has very little bearing on the overall shape determined from the experimental data because the curvature values at this location are very small, and the location of the curvature inversion is near the tip of the beam.
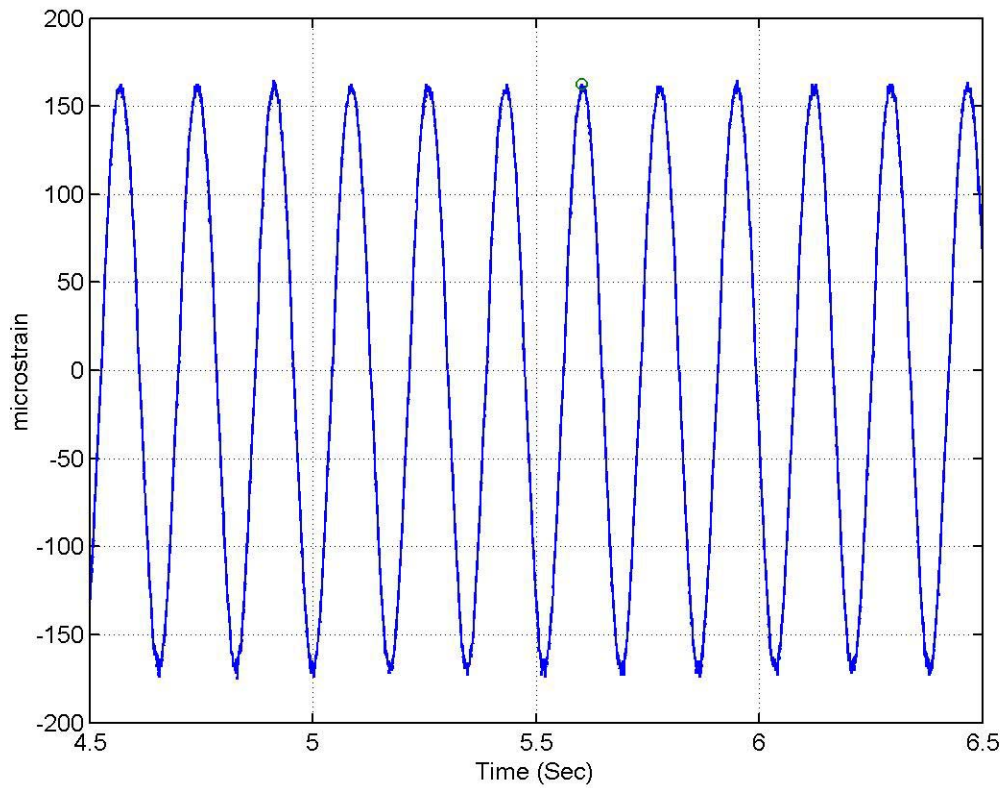
Figure 6.8: Time trace for a FBG sensor during mode 2 excitation

A portion of the time trace for the strain data collected for sensor #1 is shown in Figure 6.8. The presence of higher frequency noise is difficult to detect in this graph. FFTs of the sensor data, displayed in Figure 6.9 through Figure 6.11, show higher frequency components of the strain signal. Each FFT displays a response near 6 Hz corresponding to the frequency of the second mode.
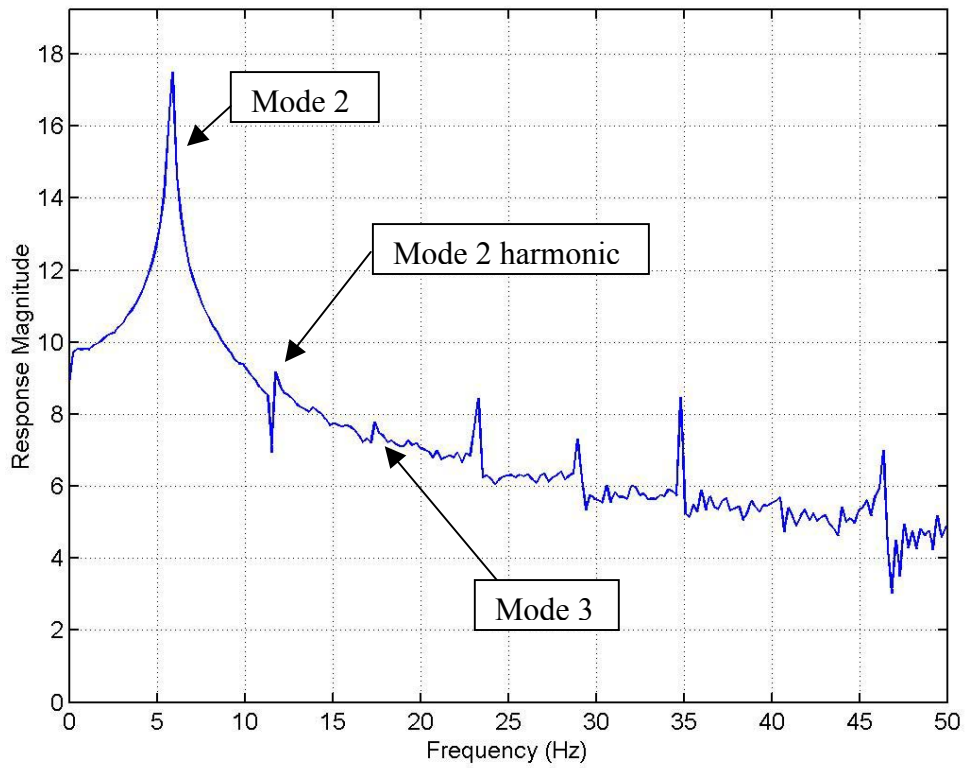
Figure 6.9: FFT plot for sensor #1 (mode 2 excitation)

The FFT response plot for sensor #1 data is shown in Figure 6.9. There is a strong mode 2 response at 6 Hz, as well as some harmonic frequencies at 12 Hz and 24 Hz. The other peaks in the frequency spectrum can be attributed to frequency mixing.
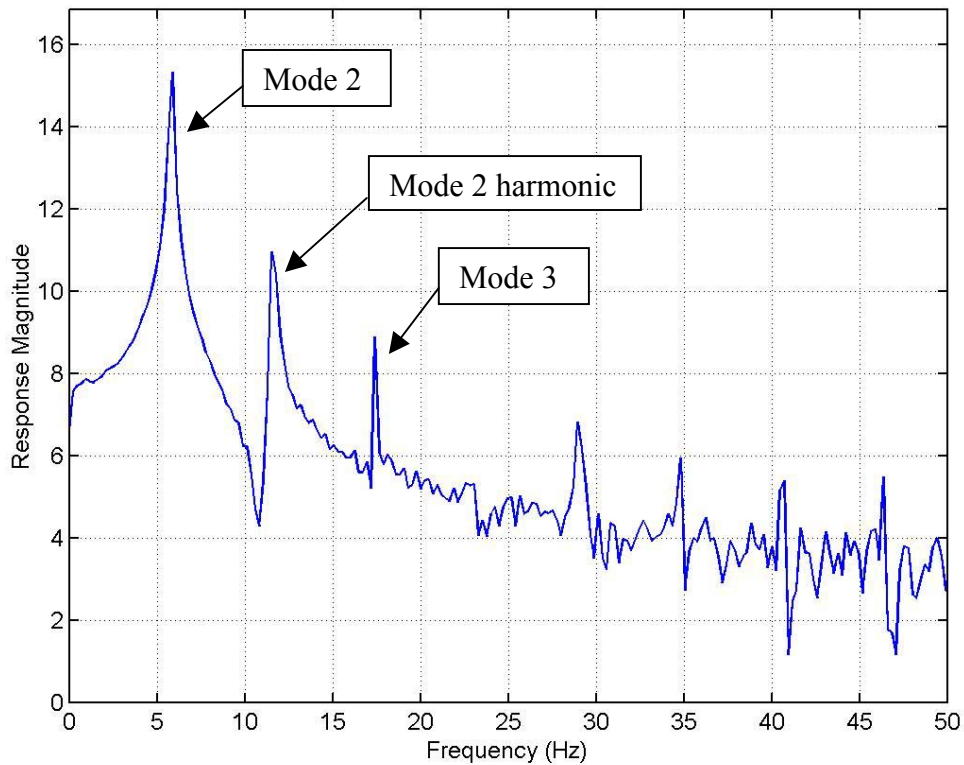
Figure 6.10: FFT plot for sensor #2 (mode 2 excitation)

Figure 6.10 displays the FFT for the second sensor for the mode 2 test. There is a peak in the FFT at 17 Hz corresponding to the third modal frequency of the beam model. There are also peaks near 12 Hz and 28 Hz (due to mixing of the mode 2 and mode 4 frequencies). These higher order vibrations were clearly evident during the testing of the mode 2 data when the amplitude was increased beyond the level used for this test.
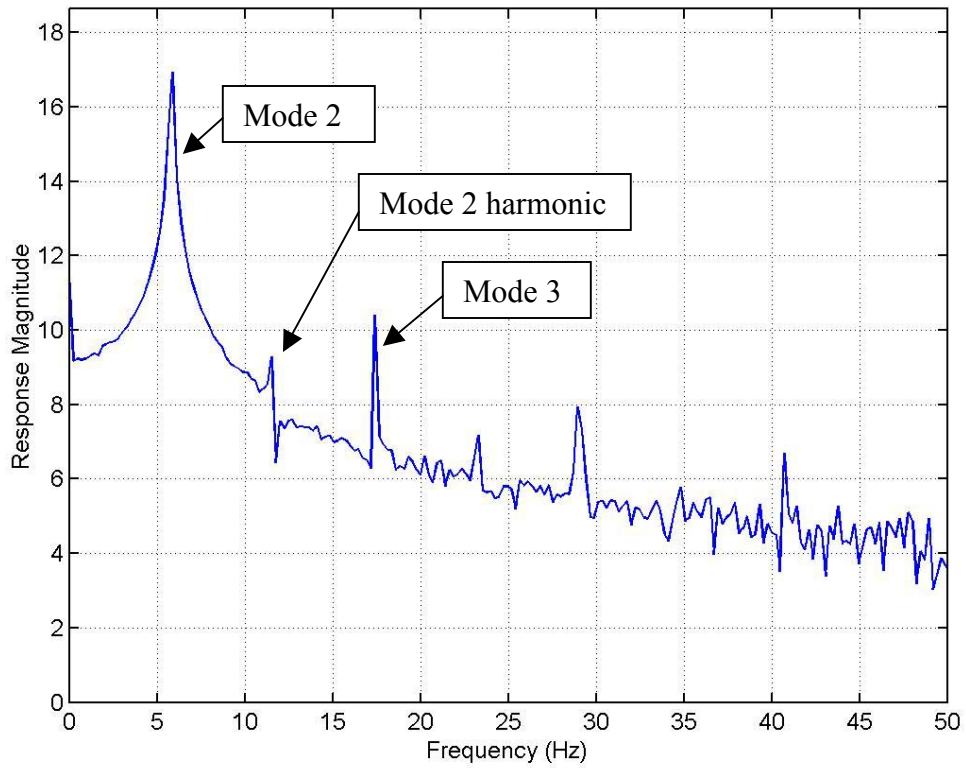
Figure 6.11: FFT plot for sensor #6 (mode 2 excitation)

Figure 6.11 displays the FFT for sensor #6 during the mode 2 test, with the main response at 6 Hz as expected. Again, a peak near 28 Hz is observed in the response spectrum. Peaks near 12 Hz and 24 Hz are also observed, and suspected to be due to harmonics of the excitation frequency of 6 Hz.

111

6.3 Mode 3 Testing: Excitation Frequency Close to the Third Natural Frequency

Figure 6.12 shows the comparison between the reference mode 3 shape and experimental shape. The tip deflection between the two is within 7 mm; however, while the experimental shape displays the reference mode 3 shape, it is displaced in the negative direction and has a lower amplitude, due to an influence from the other modes. The $error_{10}$ value for this comparison was found to be 0.0028.
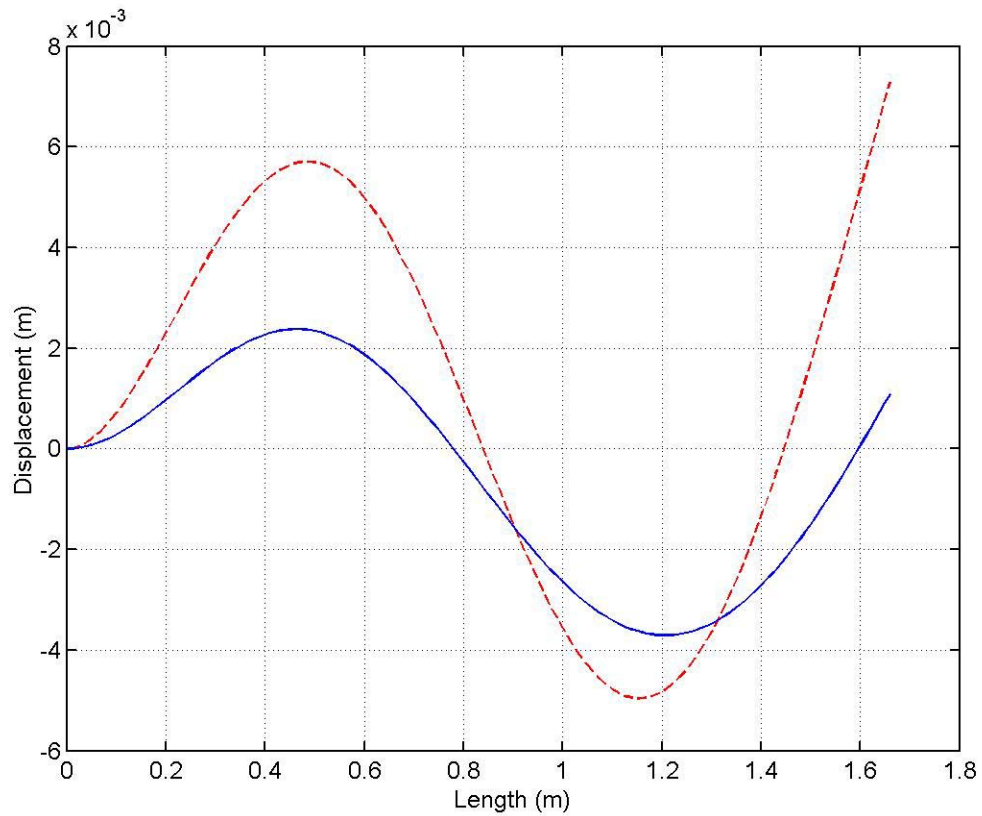
Figure 6.12: Mode 3 reference mode shape (--) and experimental shape (—) at a maximum deflection point

The curvature data for the mode 3 experiment is shown in Figure 6.13. This data appears to adequately represent a mode 3 curvature function with no apparent anomalies with the maximum curvature at the root and two inflection points.
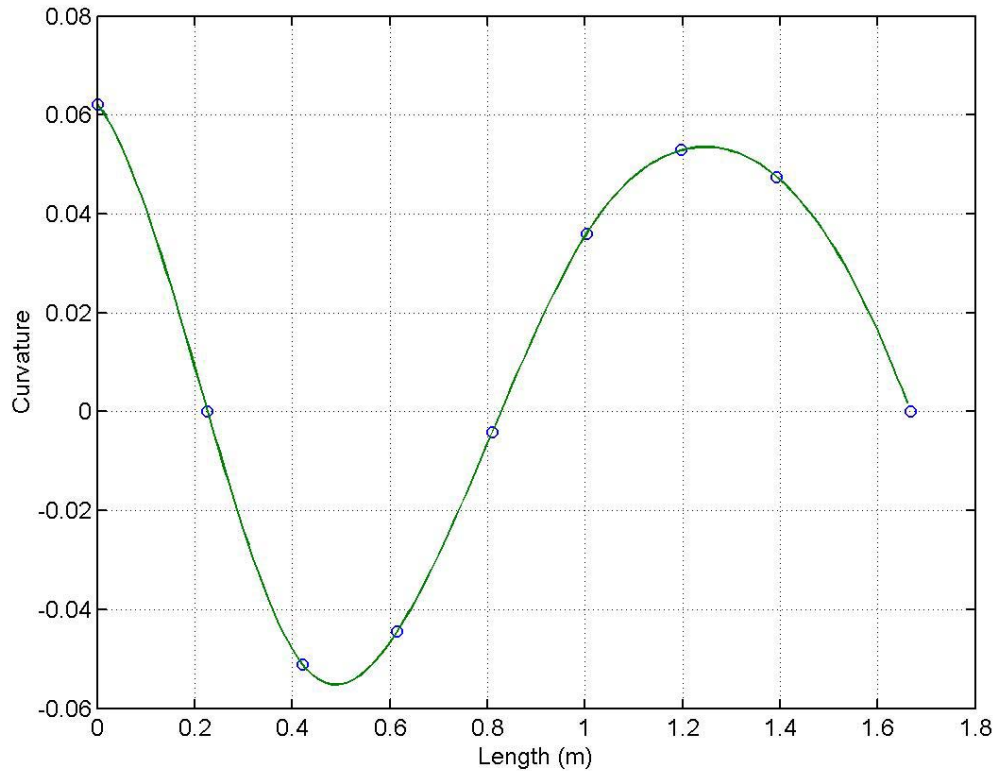
Figure 6.13: Mode 3 curvature data and positions of FBG sensors

The time trace for the strain data collected for sensor #1 is shown in Figure 6.14. The probable cause for the negative shift in the experimental shape displayed in Figure 6.12 is the influence of the other modes. In these experiments, there was no data filtering techniques used during data collection or analysis. The presence of higher frequency noise is difficult to detect by examining Figure 6.14; examining the Fourier

113

transforms of the sensor data displayed in Figure 6.15 through Figure 6.17 shows the

presence of signals at higher frequencies.
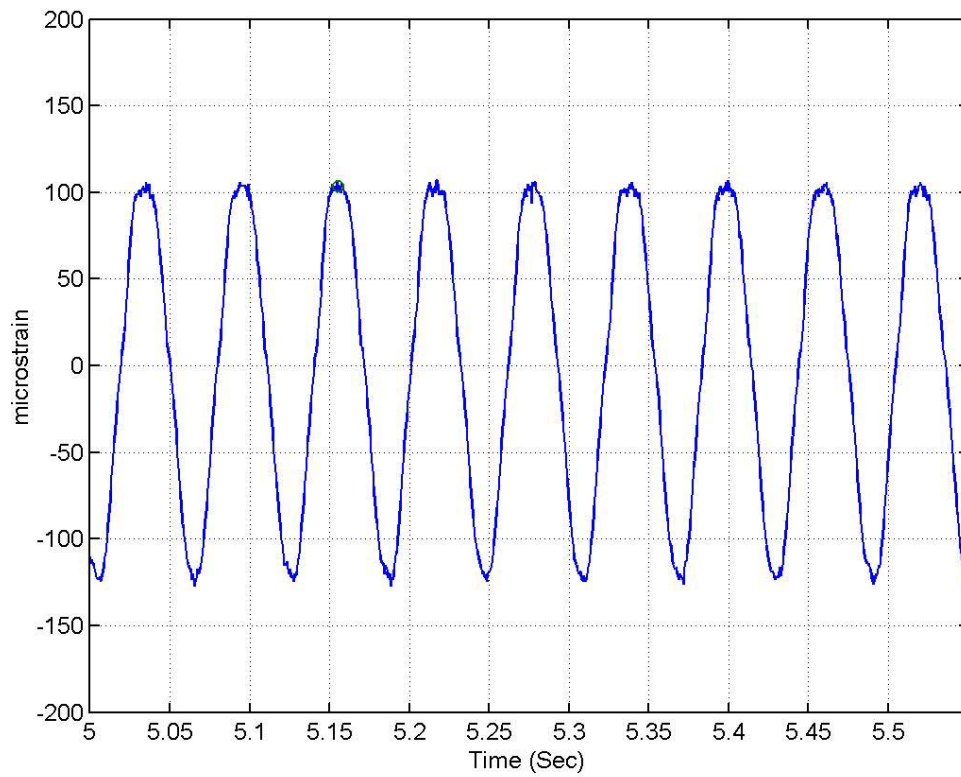
Figure 6.14: Time trace for a FBG sensor during mode 3 excitation
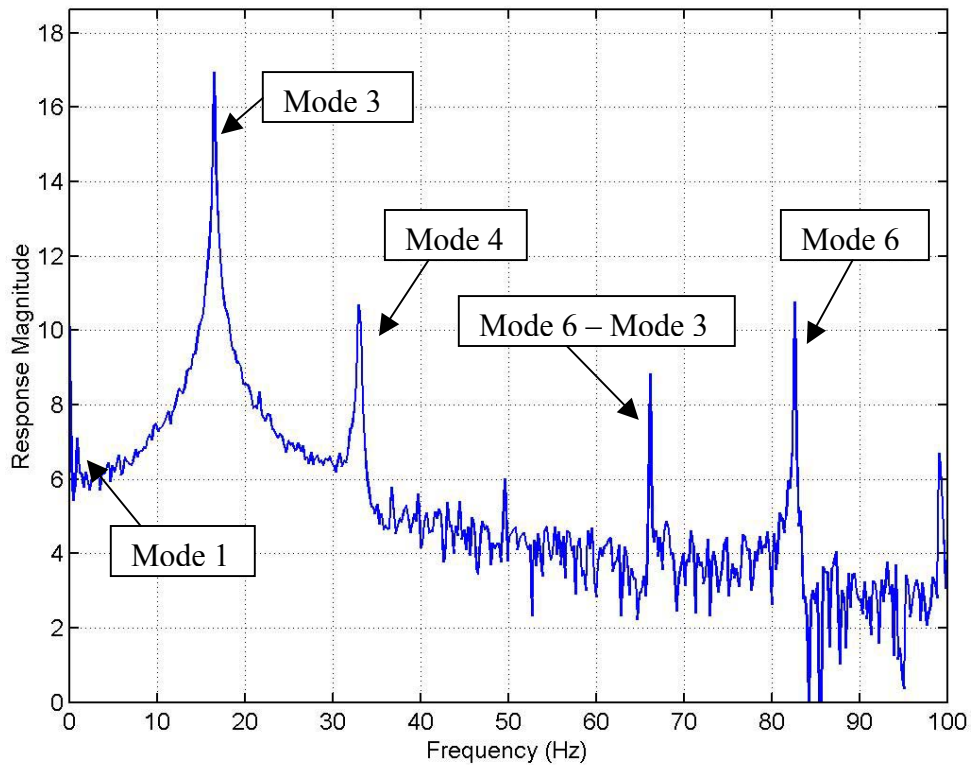
Figure 6.15: FFT plot for sensor #1 (Mode 3 excitation)

Figure 6.15 displays the FFT for sensor #1 during the mode 3 test with a prominent response peak at 17 Hz corresponding to the third resonant mode. Another peak appears near 33 Hz corresponding to the fourth mode and one at 82 Hz corresponding to the sixth mode. There are also peaks at 50 Hz, 66 Hz and 99 Hz, which are attributable to frequency mixing of the modes. For example, the frequency at 66 Hz is result of the difference between the sixth and third modes.
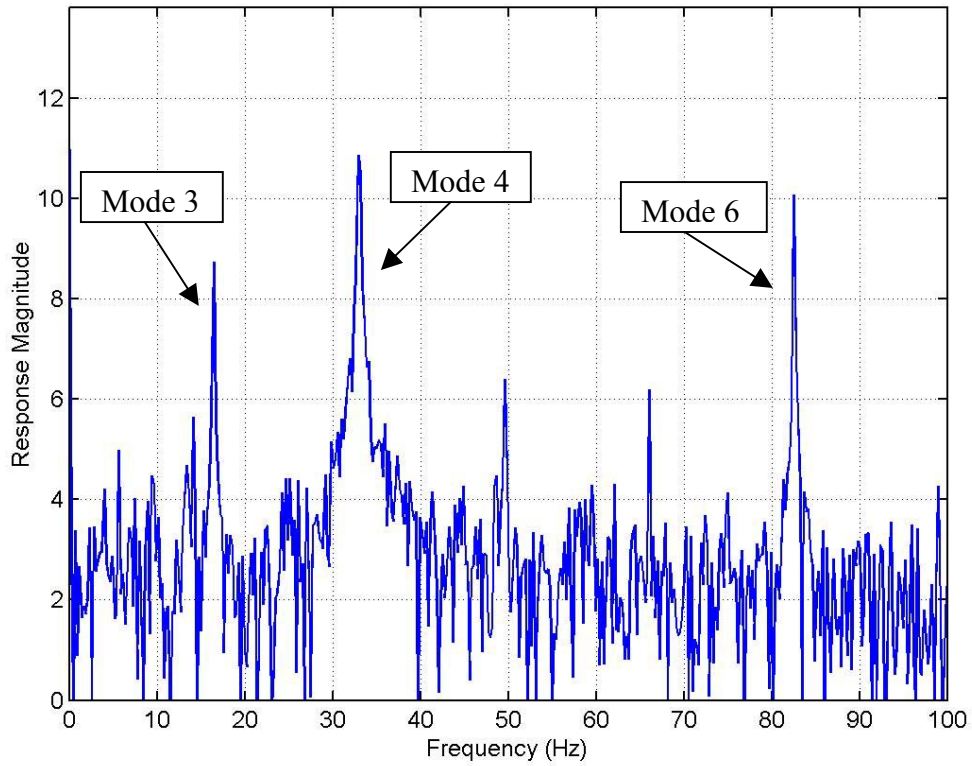
Figure 6.16: FFT plot for sensor #5 (mode 3 excitation)

Figure 6.16 shows the response data for sensor #5 during the mode 3 test. This sensor is located near the first node location for this mode shape. Therefore, there is a decrease in the response function at 17 Hz (the third resonant frequency) as compared to both Figure 6.15 and Figure 6.17. This sensor also detects the frequencies corresponding the fourth (33 Hz) and sixth (82 Hz) modes of the beam.
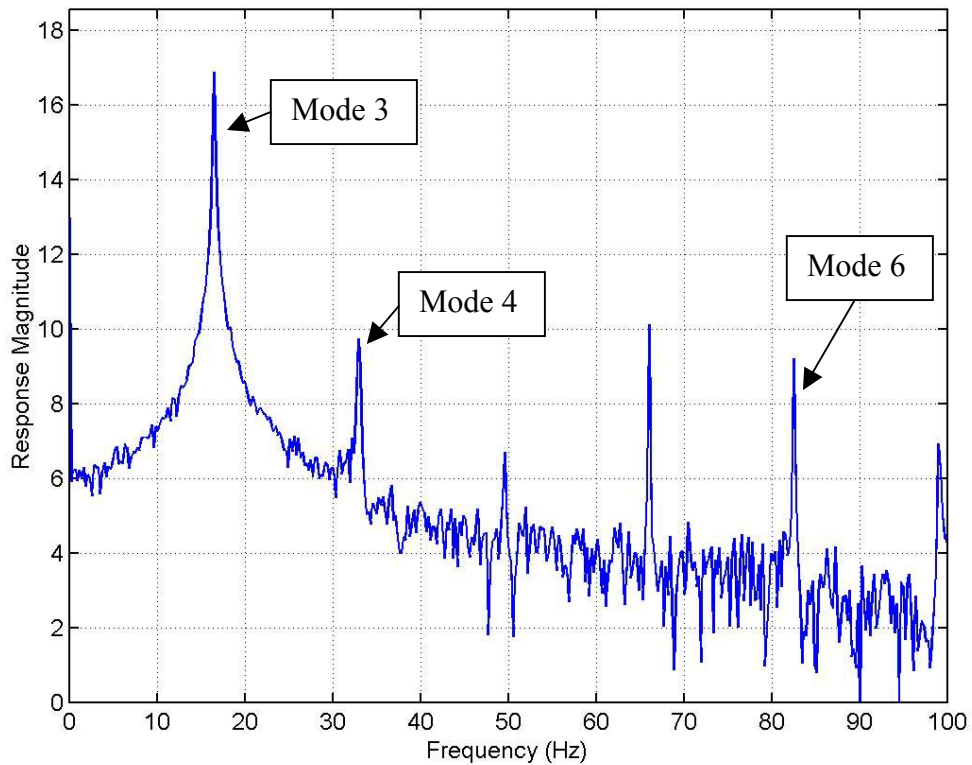
Figure 6.17: FFT plot for sensor #7 (mode 3 excitation)

Figure 6.17 displays the FFT for sensor #7 during the mode 3 test. This response is very similar to that of sensor #1 shown in Figure 6.15. It is clear that during this test as well as the previous tests that neighboring modes were influencing the response of the cantilever beam.

6.4 Mode 4 Testing: Excitation Frequency Close to the Fourth Natural Frequency

Figure 6.18 shows the comparison between the reference mode 4 shape and the experimental shape. The tip deflection between the two is within 3 mm of each other, but the experimental prediction is only 45% of the observed tip deflection. The error[10] value for this comparison was found to be 0.0016, which is not a low enough value for an accurate match. It is shown in the FFT analysis that a substantial mode 2 was influencing the structure during this excitation frequency.
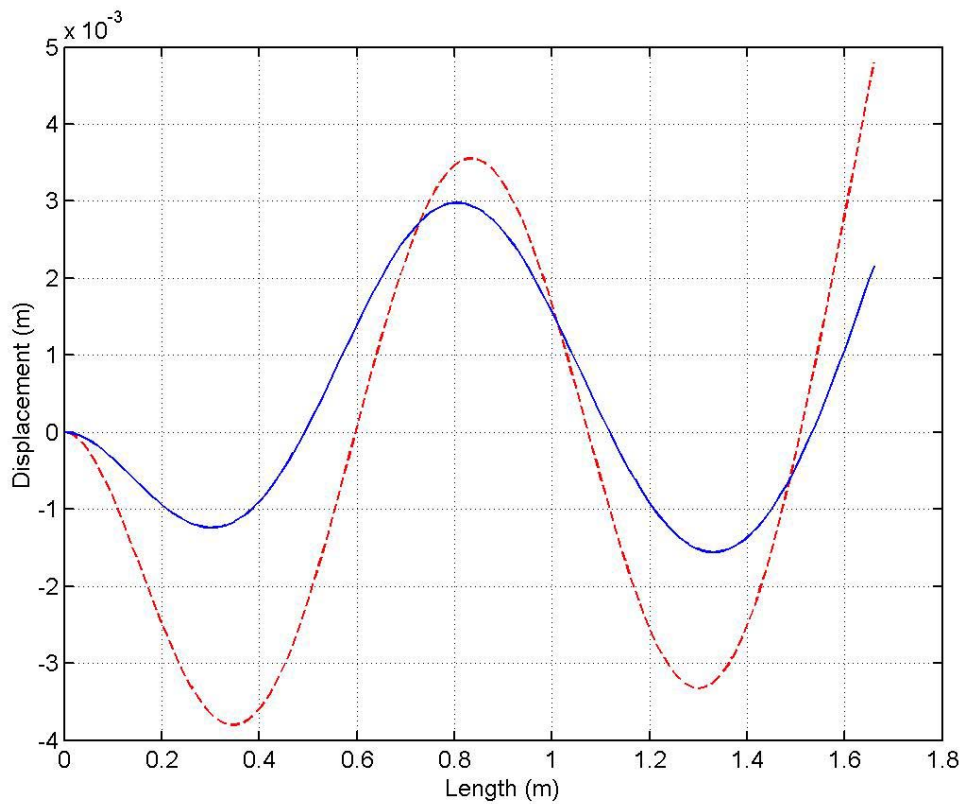
Figure 6.18: Mode 4 reference mode shape (--) and experimental shape (——) at a maximum deflection point

The curvature data for the mode 4 experiment is shown in Figure 6.19. This data appears to adequately represent a mode 4 curvature function (with three inflection points) with no apparent anomalies.
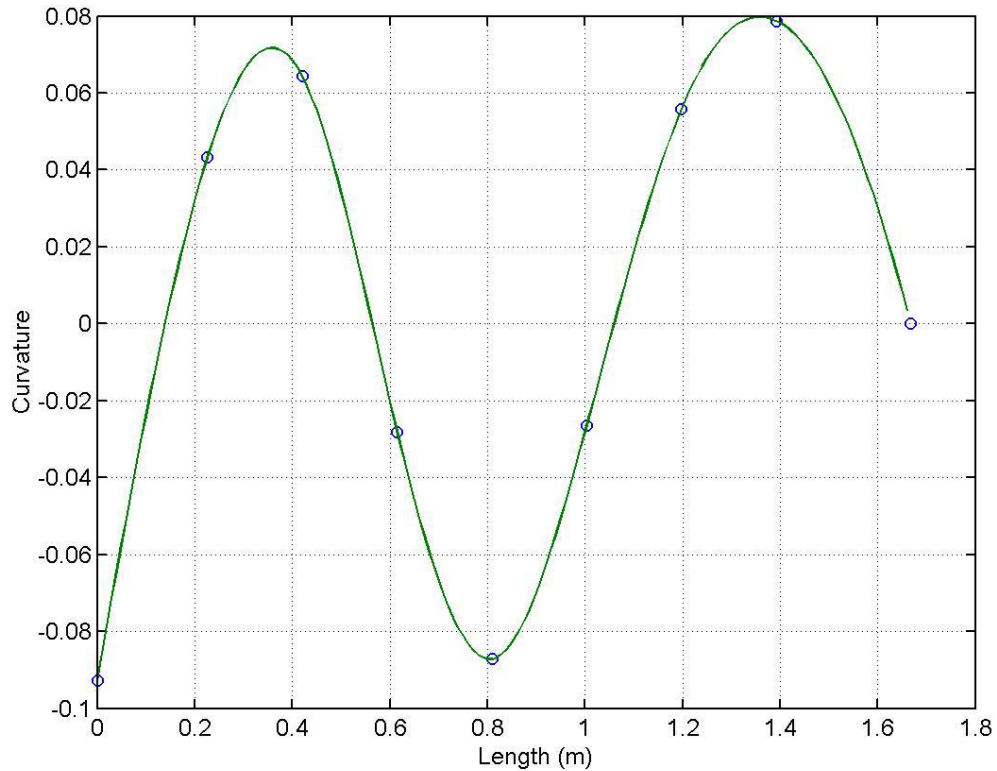
Figure 6.19: Mode 4 curvature data and positions of FBG sensors

The time trace for the strain data collected for sensor #1 for this test is shown in Figure 6.20. Examining the Fourier transforms of the sensor data displayed in Figure 6.21 through Figure 6.23 shows the presence of signals at higher frequencies. A lower frequency component can be observed in the strain data by examining the variation in

the peak amplitudes. As will be seen in the FFT analysis, this frequency corresponds to the second mode.
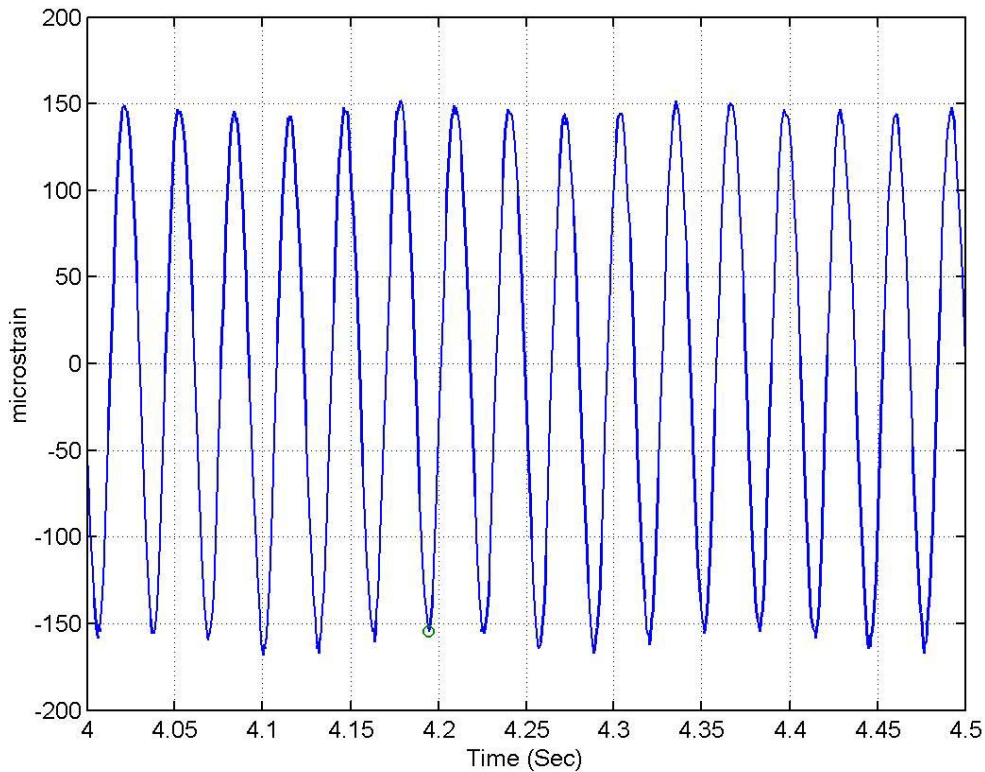
Figure 6.20: Time trace for a FBG sensor during the mode 4 excitation

The FFT plots for sensors #1, #5, and #7 is shown in Figure 6.21, Figure 6.22, and Figure 6.23, respectively. Each of the plots displays a strong response at the fourth resonant mode frequency of 33 Hz. A small response is also seen at the second mode at 6 Hz. Peaks in the frequency spectrum are also seen at near 66 Hz and near 99 Hz, which could be associated with harmonics of the 33 Hz excitation frequency.
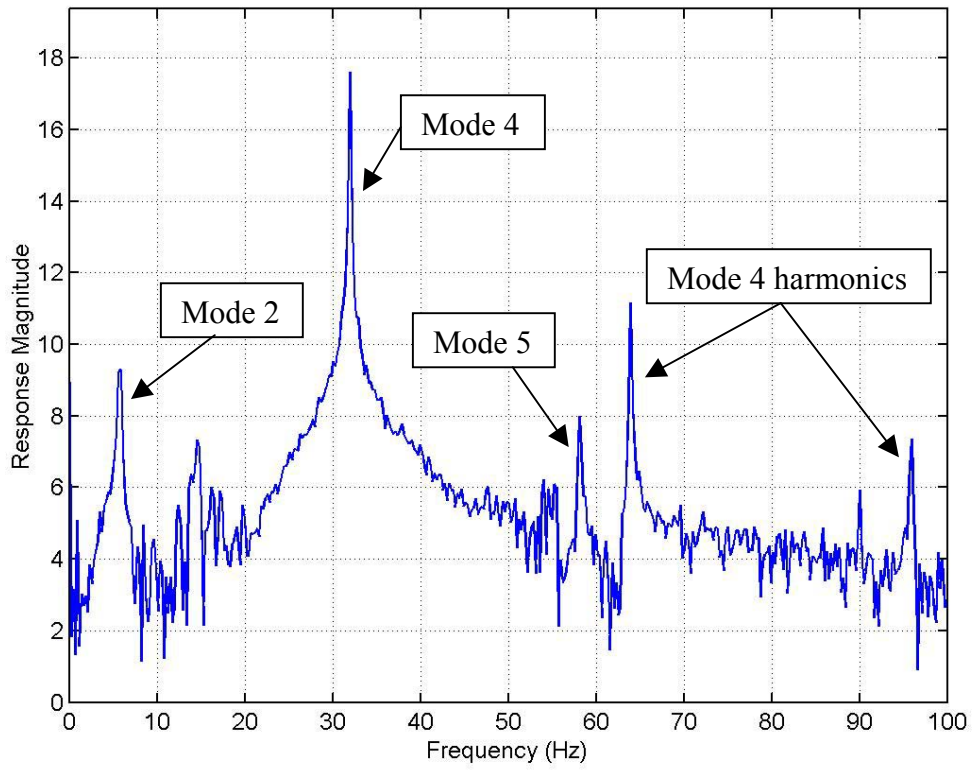
Figure 6.21: FFT plot for sensor #1 (mode 4 excitation)
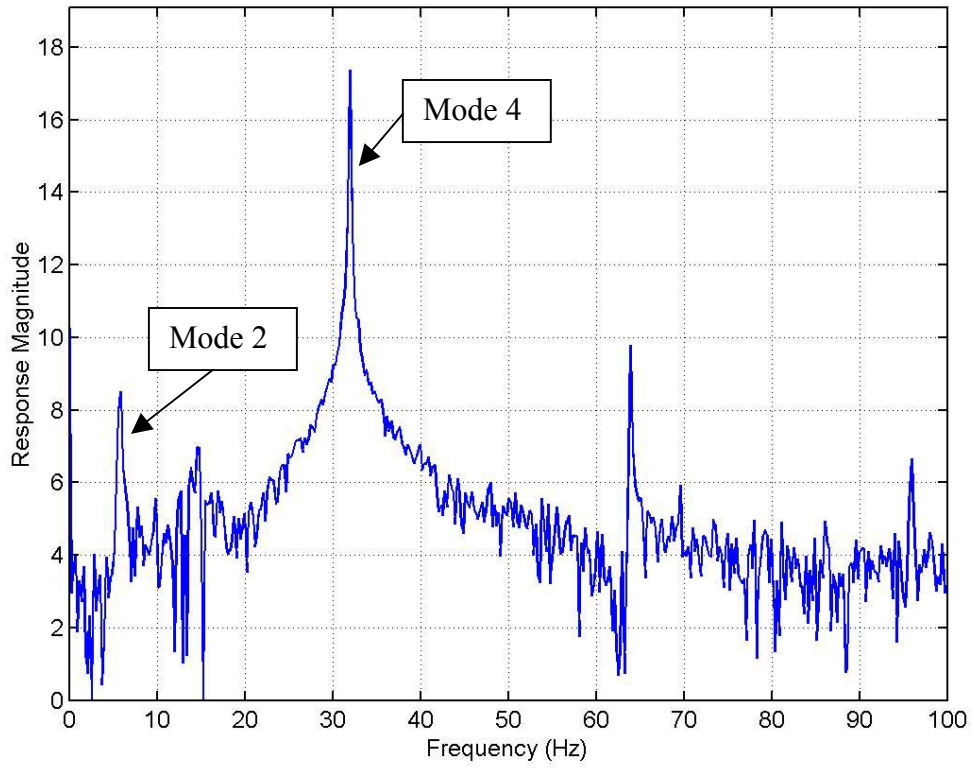
Figure 6.22: FFT plot for sensor #5 (mode 4 excitation)
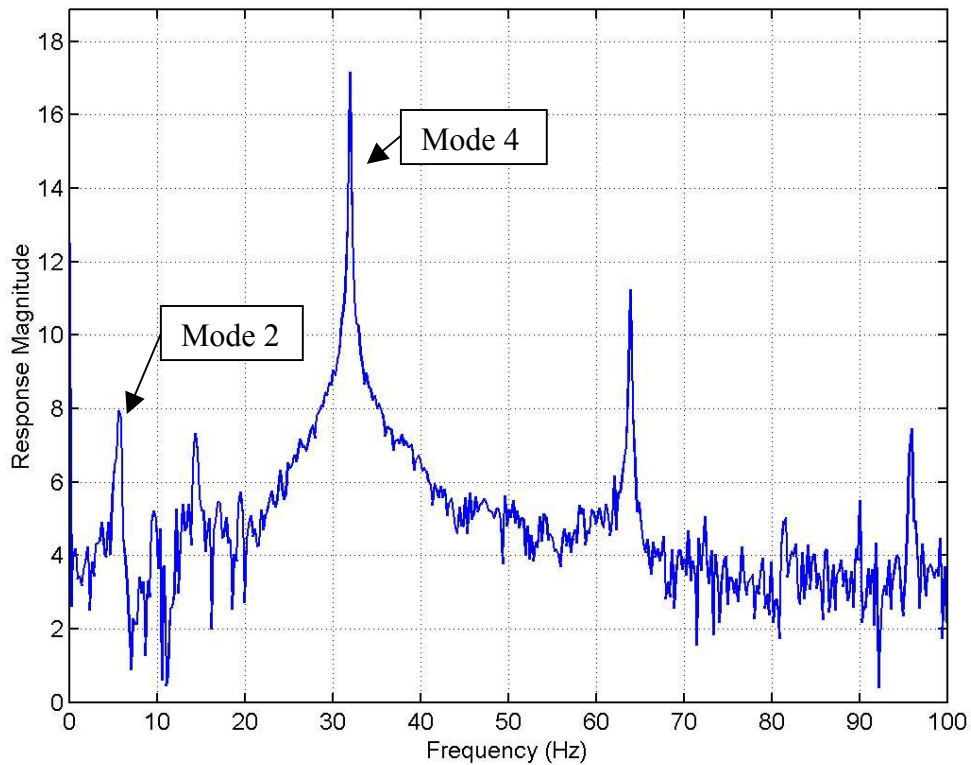
Figure 6.23: FFT plot for sensor #7 (mode 4 excitation)

6.5 Mode 5 Testing: Excitation Frequency Close to the Fifth Natural Frequency

Figure 6.24 displays the comparison between the reference mode 5 shape and the experimentally determined shape. The experimentally determined shape has the characteristics of a mode 5 shape, but obviously does not follow the reference shape. The $error_{10}$ value for this comparison was found to be 0.0032. The FFT plots show a large response of lower frequencies especially mode 2, which attribute to this effect.
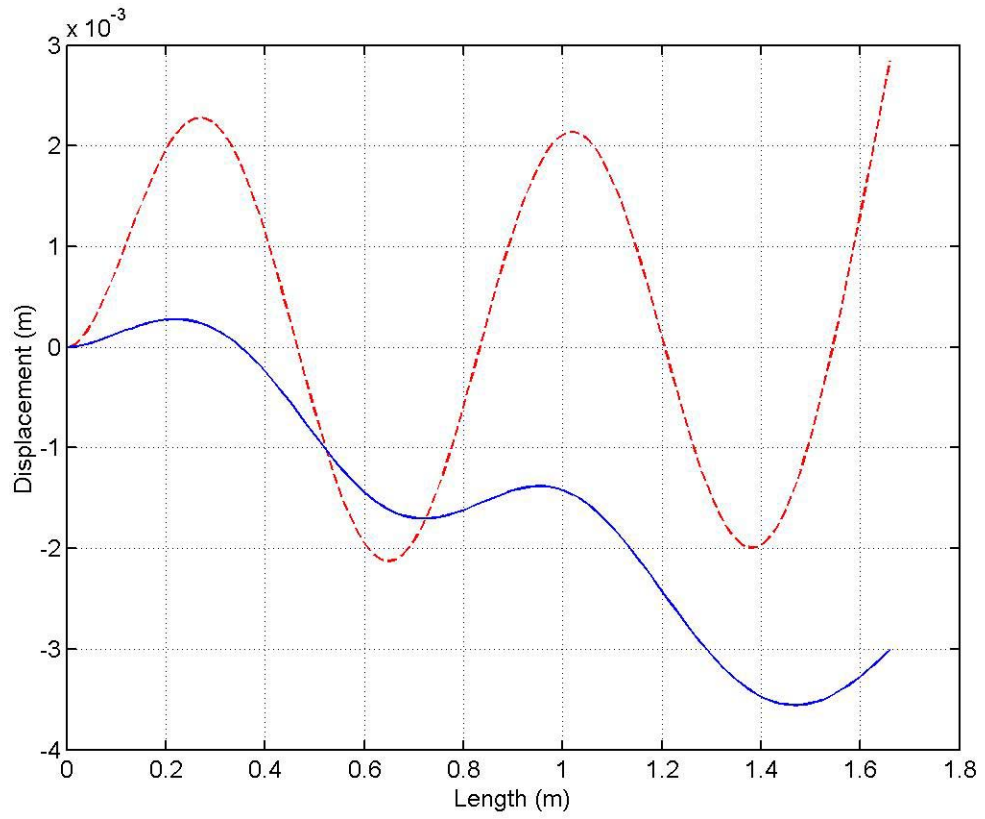
Figure 6.24: Mode 5 reference mode shape (--) and experimental shape (—) at a

maximum deflection point
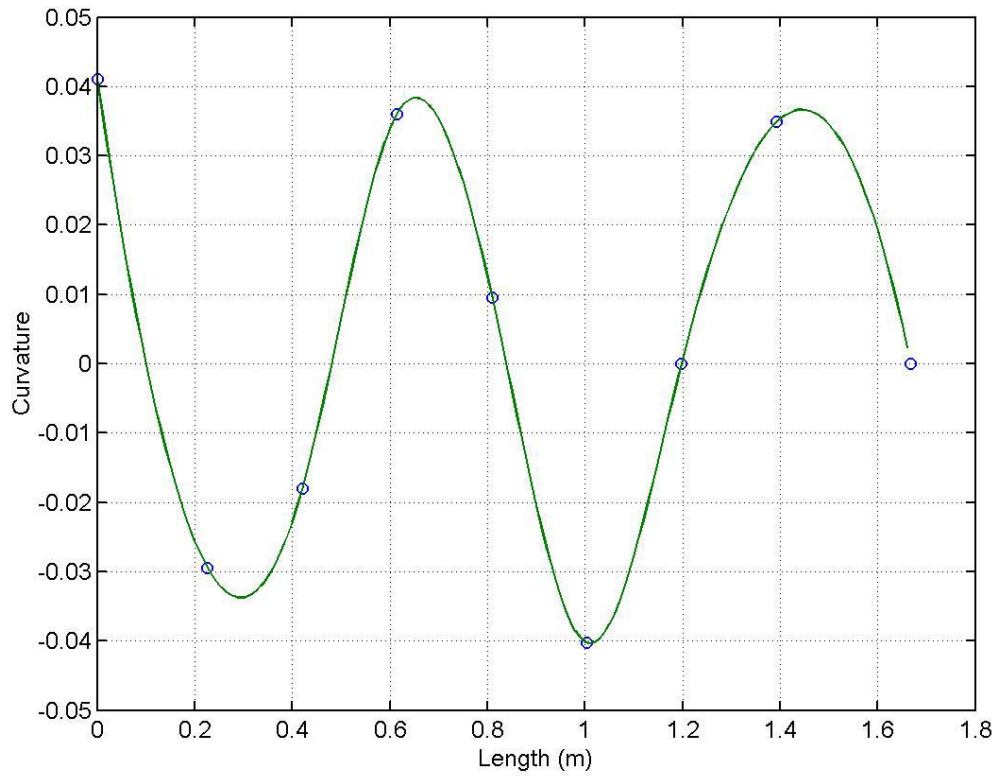
Figure 6.25: Mode 5 curvature data and positions of FBG sensors

Figure 6.25 shows the curvature data obtained for the mode 5 excitation experiment. This data appears to adequately represent a mode 5 curvature shape with 4 inflection points and no apparent anomalies.
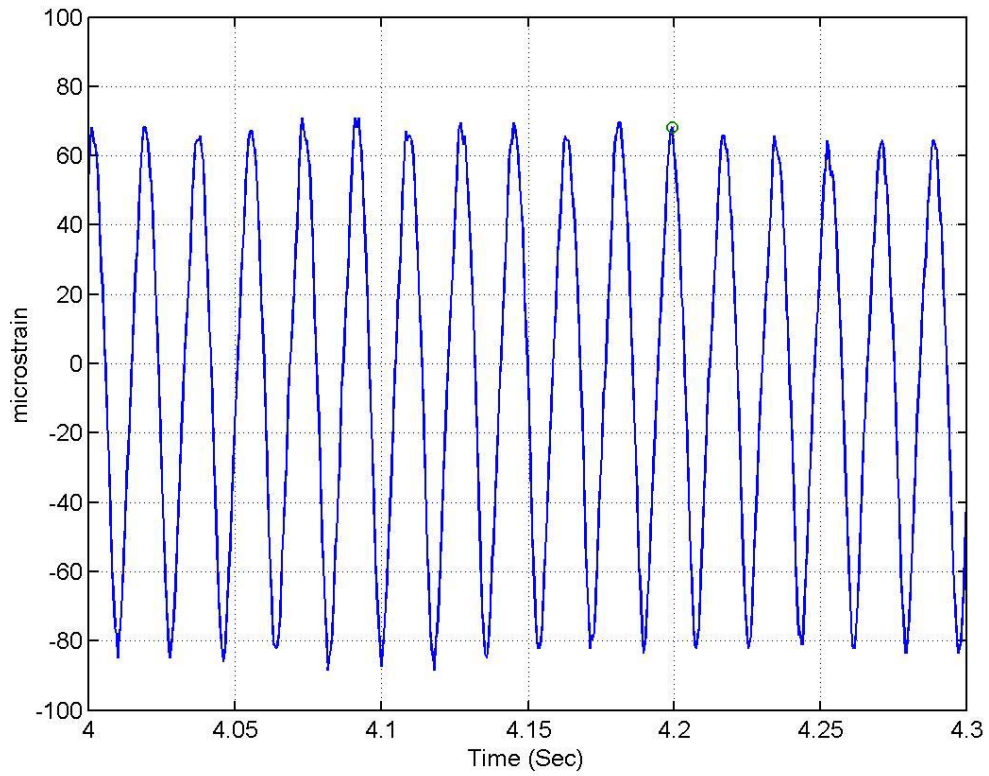
Figure 6.26: Time trace for a FBG sensor during the mode 5 excitation

Figure 6.26 displays the time trace for the recorded strain data of sensor 1 for the mode 5 excitation. A low frequency component is observable in the variation in the amplitude of the sensor data. This low frequency is also evident in the FFT of the sensor data shown in Figure 6.27.
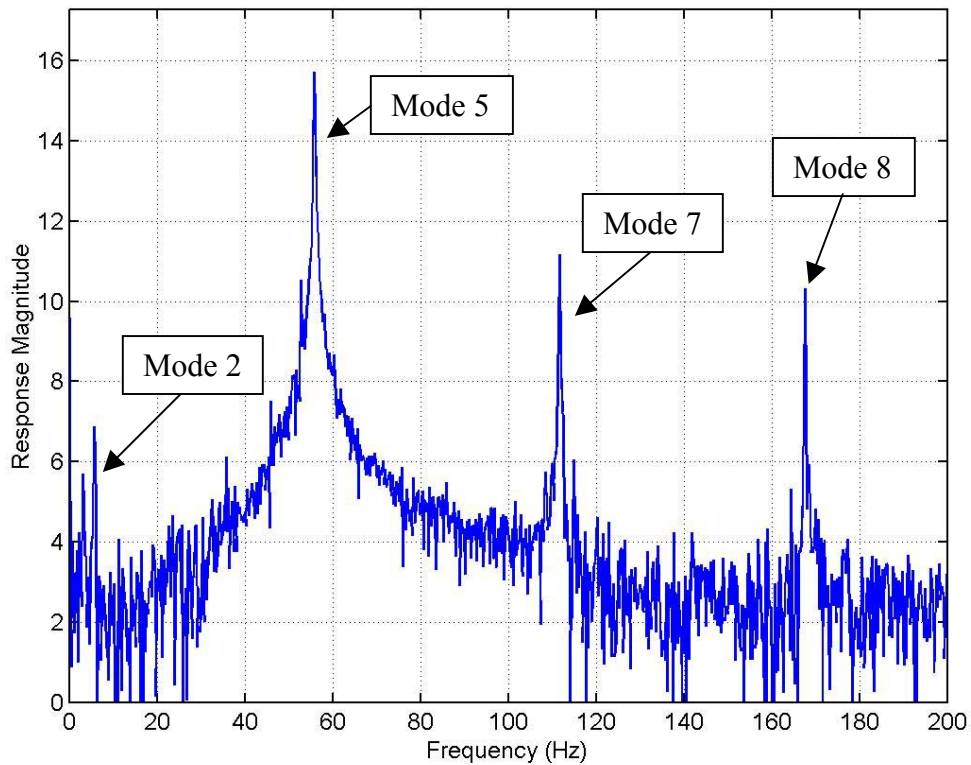
Figure 6.27: FFT plot for sensor #1 (mode 5 excitation)

The FFT response for the sensor #1 data shown in Figure 6.27 displays a strong response peak at the fifth resonant frequency of 56 Hz. There is also a response at frequencies less than 10 Hz (second mode ~ 6 Hz). The response peak for the fifth resonant frequency is spread over a wide frequency range as compared to the resonant frequencies shown for modes 1 through 4. The frequencies for the seventh (~115 Hz) and eighth (~165 Hz) modes are observed in the FFT response plot. A similar FFT response is observed for sensor #5 data shown in Figure 6.28.
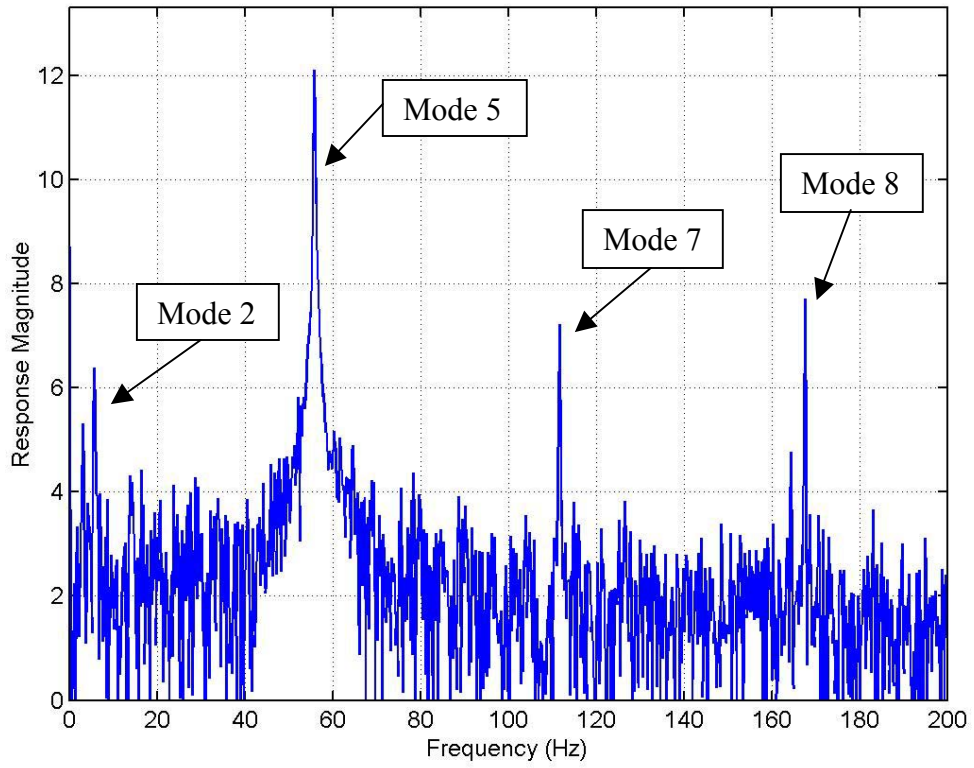
Figure 6.28: FFT plot for sensor #5 (mode 5 excitation)
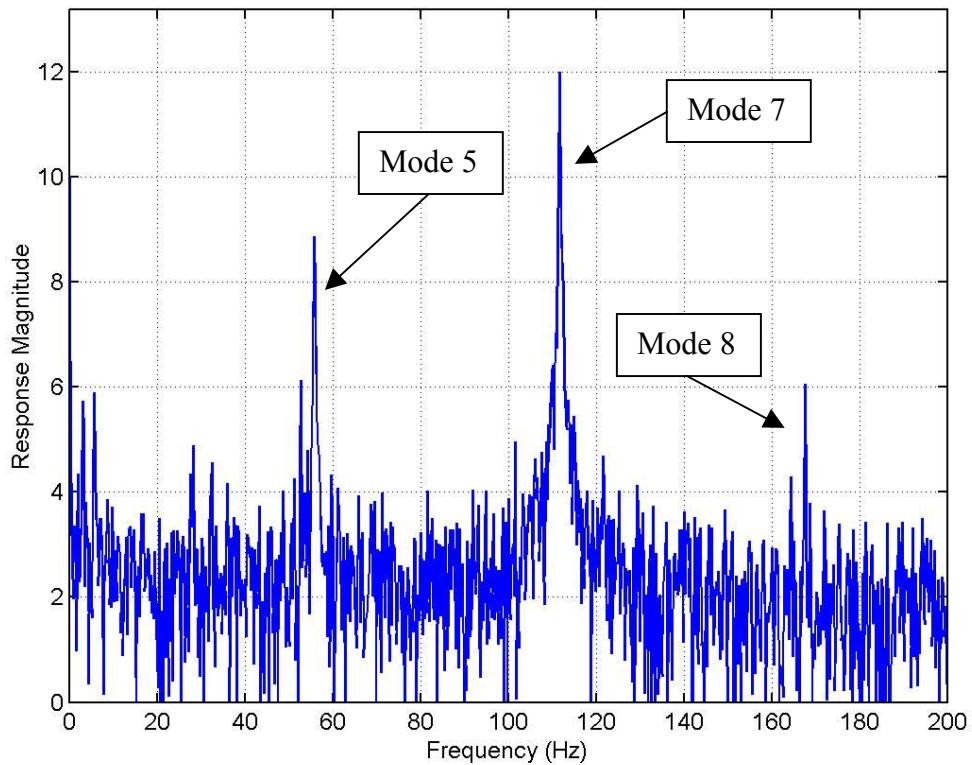
Figure 6.29: FFT plot for sensor #7 (mode 5 excitation)

The FFT response for the sensor #7 data shown in Figure 6.29 does not display a strong response peak at the fifth resonant frequency of 56 Hz. This is because sensor #7 is located near a node location for this mode shape. The mode 7 and mode 8 frequencies are evident in the FFT data, as was the case with the other sensor data.

6.6 Sources of Experimental Error

Discrepancies are observed between the experimental shapes and the reference mode shapes presented in this Chapter. Possible sources for error in the experimentally determined shape discussed in this section include strain measurement error, tip deflection measurement error, and the influence of multiple active modes of the structure.

The strain measurement error can be attributed to random noise in the strain monitoring instrumentation ($\pm 5 \ \mu\varepsilon$). Also, the location of each FBG sensor along the cantilever structure is used as input to the shape calculation algorithm. This measurement has a level of error ($\sim \pm 5$ mm) associated with it that will affect the experimental shape result. Another aspect of measurement error is the lack of a sensor at the exact root of the cantilever structure. As discussed in Chapter 5, the measurement for the bending strain at the root of the cantilever structure is determined from the first sensor multiplied by a calibration factor determined from beam theory. These measurement error sources are recognized as possible contributors to the discrepancy between the experimental shape and the reference mode shape. The influence of the measurement error on the experimental shape is considered minimal compared to the influence from other structural modes. For example, variations of $\pm 5 \ \mu\varepsilon$ in strain values and ± 5 mm in sensor position correspond to roughly a 5 mm uncertainty in the tip position for a mode 1 vibration under conditions of Figure 6.1.

In Chapter 7, the primary influence affecting the experimentally determined shape, extraneous modal components, is investigated. If the cantilever structure were to experience a linear response due to the single frequency excitation, then only the nearest resonant mode would be observed in the experimental data. The extreme length of the structure allowed the single frequency excitation to excite a nonlinear response; thus, allowing several modal components to influence the dynamics of the structure. For each of the first five mode shapes discussed in this chapter (and for mode 6 and mode 7 shown in Appendix B), frequency components from other modes are evident in the FFT analysis. The following chapter investigates the use of modal analysis techniques to obtain a more accurate representation of experimentally determined beam shape as a combination of several fundamental modes.

7 Modal Analysis

In Chapter 6, experimental beam shape results were examined and compared to reference mode shapes. In most cases, the experimental results resembled the reference mode shapes but did not match them exactly. FFTs of the recorded strain data demonstrated that more than one mode was being excited during the experiment. This chapter investigates modal analysis techniques to determine the influence of several modes on a given structural vibration.

As discussed in Section 3.1, the dynamic shape of a structure at any time is determined from a summation of mode shapes (ϕ), as:

$$y(x) = \sum_{r=1}^{m} A_r \phi_r(x) \qquad (7.1)$$

The objective of the research presented in this dissertation is to determine the shape of a vibrating structure at a particular time based on the measured strain readings along the structure. From the measured strain information, details regarding the modal deflection of the structure cannot be easily extracted. FFTs are used to analyze the frequency spectra of the strain readings, providing a means of determining the modal characteristics of the structure averaged over a particular sample time, not at a particular

132

time during the structural vibration. This chapter outlines a method of determining the modal coefficients (A_r) for experimentally determined deflection shapes at any given time within the data set. To accomplish this, the structure is assumed to be a linear combination of theoretical normal mode shapes. The discussion in this dissertation is restricted to the case of cantilever structures that can be modeled as beams, but the analysis could be expanded to more complex structures with mode shapes that are known. Because theoretical mode shapes are used, a well-behaved structure with known modal dynamic behavior will provide better results from this analysis than a complex structure with undefined mode shapes.

7.1 Derivation of Modal Influence Determination

As discussed in Section 4.1, the error between the reference shape and the experimentally determined shape is given by the following function:

$$\text{error}_n = \frac{\sqrt{\left(y_{exp}(x_1) - y_{theory}(x_1)\right)^2 + \cdots \left(y_{exp}(x_n) - y_{theory}(x_n)\right)^2}}{n} \tag{7.2}$$

where x_i are positions along the structure and n is the number of evaluation points used to determine the error. The methodology for determining the best modal coefficients involves minimizing the error function with respect to the modal coefficients.

$$\frac{d\,\text{error}_n}{d\,A_r} = 0 \tag{7.3}$$

This relation is used to determine a unique set of A_r values such that the error function is minimized. Allowing u to equal the quantity under the square root, as

$$u = \left(y_{exp}(x_1) - \sum_{r}^{m} A_r \phi_r(x_1)\right)^2 + \cdots \left(y_{exp}(x_n) - \sum_{r}^{m} A_r \phi_r(x_n)\right)^2 \qquad (7.4)$$

then the error function minimization is found to be

$$\frac{d\,error_n}{d\,A_r} = \frac{1}{2n} \frac{1}{\sqrt{u}} \left[2\left(y_{exp}(x_1) - \sum_{r}^{m} A_r \phi_r(x_1)\right)\left(-\sum_{r}^{m} \phi_r(x_1)\right) + \cdots\right] = 0 \qquad (7.5)$$

where the term in the square bracket must be zero. One manner that this may be achieved is that the term in the first parenthesis may be zero for each data point x_i.

$$y_{exp}(x_1) - \sum_{r}^{m} A_r \phi_r(x_1) = 0$$
$$\vdots \qquad\qquad (7.6)$$
$$y_{exp}(x_n) - \sum_{r}^{m} A_r \phi_r(x_n) = 0$$

Equation 7.6 states that the error function is minimized when the theoretical value at each data point (x_i) is equivalent to the experimental value. The set of equations can be written in matrix form as:

$$\begin{bmatrix} \phi_1(x_1) & \cdots & \phi_m(x_1) \\ \vdots & \ddots & \vdots \\ \phi_1(x_n) & \cdots & \phi_m(x_n) \end{bmatrix}\begin{bmatrix} A_1 \\ \vdots \\ A_m \end{bmatrix} = \begin{bmatrix} y_{exp}(x_1) \\ \vdots \\ y_{exp}(x_n) \end{bmatrix} \qquad (7.7)$$

The matrix on the left of Equation 7.7 contains the theoretical mode shapes, and will be denoted as the matrix **H** in subsequent analysis. Allowing **A** to represent the modal coefficient vector and **Y** to represent the deflection data vector, Equation 7.7 is written as:

$$[H][A] = [Y] \qquad (7.8)$$

If **H** is a square matrix and an inverse exists, then the modal coefficients can be found as:

$$[A] = [H]^{-1}[Y] \tag{7.9}$$

To determine a unique solution set of A_r values, **H** must be square for an inverse to be determined, hence m = n (the case of a pseudo-inverse with n > m will be discussed in Section 7.4). For the square matrix, values for A_r can be determined from examining the number of x data points equal to the number of modes of interest. For example, if only the first four modes are of interest, then only four deflection values along the beam are required. The **H** matrix must also have constraints that allow an inverse to exist; i.e. each row of the matrix must be independent. Therefore, the selection of the x_i values must be chosen with regard to the independence of the **H** matrix. If the value $x_1 = 0$ were chosen, then for the case of a cantilever beam the boundary condition of $\phi(0,t) = 0$ would necessitate a row of zero values in **H**, such as:

$$[H] = \begin{bmatrix} 0 & \cdots & 0 \\ \vdots & \ddots & \vdots \\ \phi_1(x_n) & \cdots & \phi_m(x_n) \end{bmatrix} \tag{7.10}$$

The inverse of this matrix is undefined, and therefore can not be used to determine the modal coefficients in Equation 7.9.

7.2 Analytical Modeling with Beam Functions

A MATLAB program was written for analysis of the first 8 mode shape functions. Multiple combinations of mode shapes were examined using the analysis method discussed in Section 7.1. For each case examined, the algorithm was able to exactly determine the modal coefficients from simulated deflection data based on beam

theory. The analytical tests assumed an even distribution of points (x_i) along the beam

shape for inclusion in the **H** matrix formulation. Following this successful test, the code

was exercised with the experimentally determined shape data.

7.3 Experimental Data Modal Analysis using Square Inverse

The experimentally determined shape data discussed in Chapter 6 was processed

using the modal determination analysis derived in Section 7.1. For the first four mode

shapes, the analysis considers the influence of the first four modes. The fifth resonant

mode is examined to determine the influence of a variable number of modes (up to 8

modes).

7.3.1   Mode 1 Vibration

Based on the shape determination discussed in Section 6.1, the modal

coefficients for the first mode vibration should reflect a strong influence of the first

mode and very little influence from the higher modes. The experimentally determined

shape was processed with the modal analysis technique to determine the modal

coefficients of the first four modes. The four x positions chosen for input to the modal

analysis algorithm were arbitrarily selected along the length of the structure. The A_r

values for the test case were determined to be: A_r = [**0.9829**   0.0004   0.0104

0.0074]. The coefficient for the first mode is shown in bold to indicate that it is the

mode of interest for this case. As expected the first mode is dominant. Figure 7.1

shows the mode shape determined from the modal coefficients (A_r) for the mode 1 test

case. This is compared to the reference mode shape for the mode 1 deflection and the

experimental shape, as discussed in Section 6.1. The agreement between the shape

determined from the Ar values and the experimental shape is quite good. The $error_{10}$

value derived from this comparison is 1.405 e-4, which is an order of magnitude

improvement compared to an $error_{10}$ value of 0.005 found when the shape measurement

is compared to the reference mode 1 shape. Although difficult to discern in Figure 7.1,

the shape measurement and the theoretical modal response shape do show small

differences near the tip of the beam. These differences will be shown to arise from the

arbitrary selection of the four experimental values used in the modal analysis algorithm.
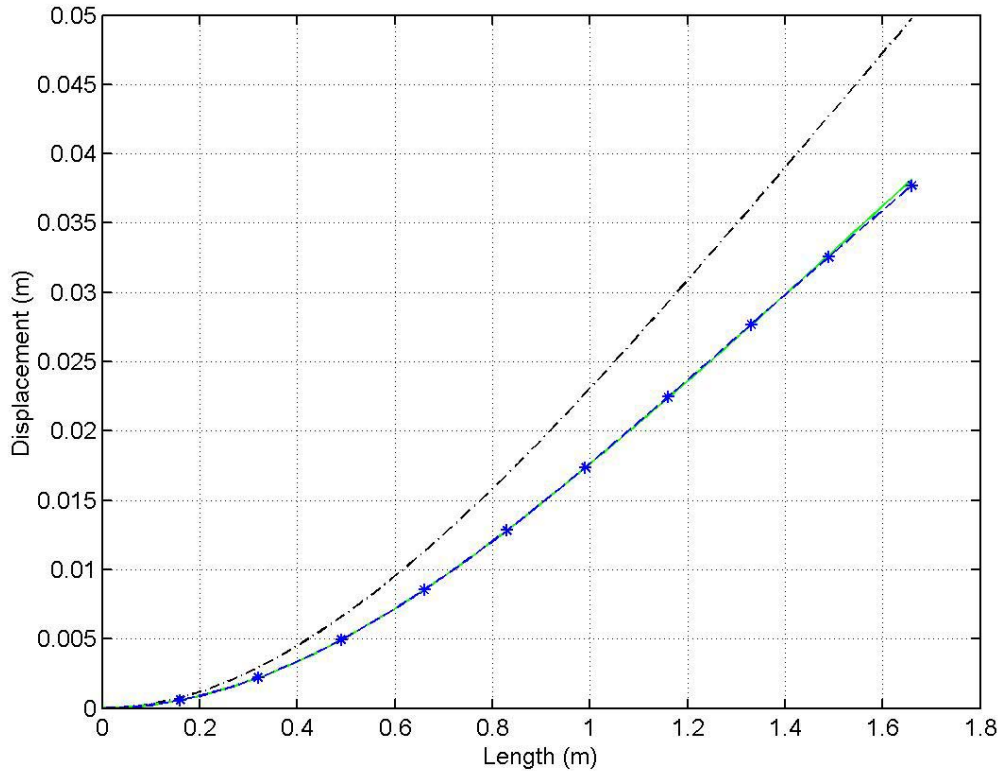
Figure 7.1: Shape comparison between reference mode 1 shape (-··-), experimentally

determined shape (——), and the shape based on modal coefficients (*-)

Figure 7.2 displays the dynamic variation in the A_r values versus time for a few cycles of the mode 1 excitation. The modal coefficient representing the mode 1 resonance is dominant during most of the vibration cycle. The times when the influence of higher order modes increase are associated with the beam crossing the zero position (i.e. $y_{exp}(x) \approx 0$) leading to an arbitrary solution of Equation 7.9. At times of a zero crossing, the structure is in the equilibrium position; hence, no modal components are influencing the structure to obtain that particular shape.
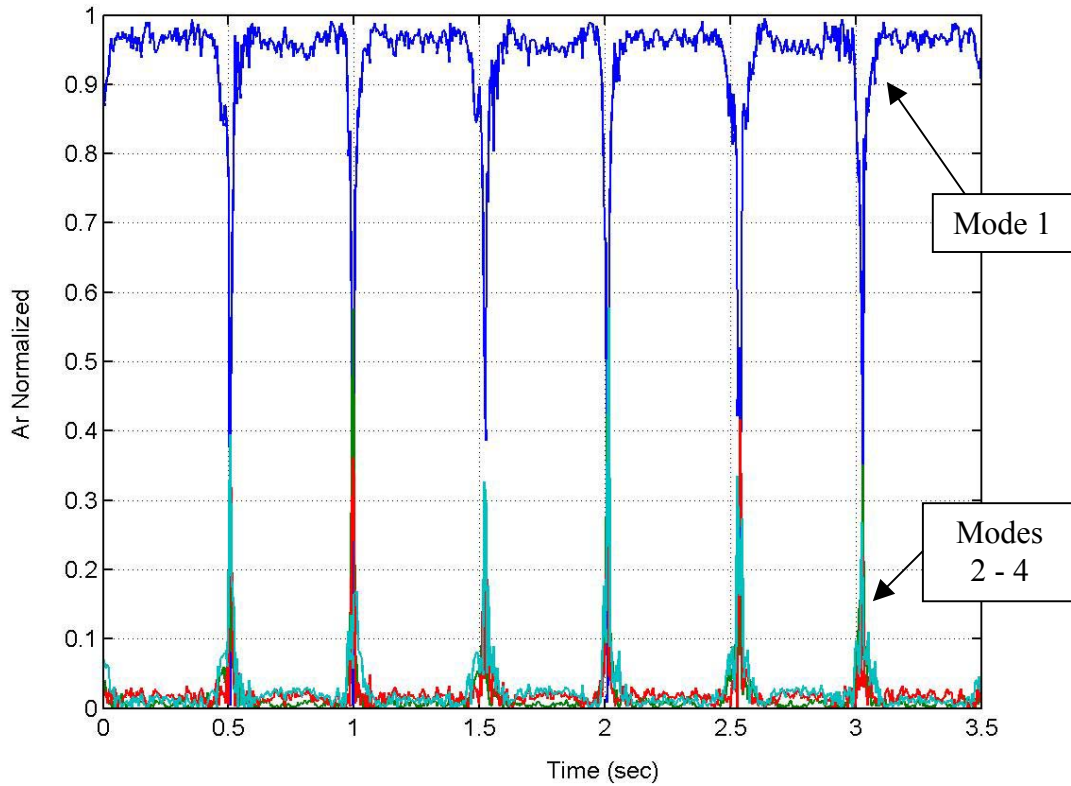
Figure 7.2: Modal coefficients versus time for mode 1 excitation

7.3.2   Mode 2 Vibration

Results similar to those for mode 1 are found for the mode 2 case. The

experimentally determined shape was processed with the modal analysis technique to

determine the modal coefficients of the first four modes at an arbitrary time within the

data set. The A_r values for this case were determined to be: A_r = [0.0652   **0.9218**

0.0034   0.0096]. Figure 7.3 graphically shows the fit of the mode 2 test case discussed

in this section; the mode shape determined from the modal coefficients (A_r) compares

quite accurately to the shape measurement, as shown in Figure 7.3. The error$_{10}$ value

determined for this comparison is 3.36 e-5, which is two orders of magnitude lower

compared to an error$_{10}$ value of 0.006 found when the shape measurement is compared

to the reference mode 2 shape in Section 6.2.
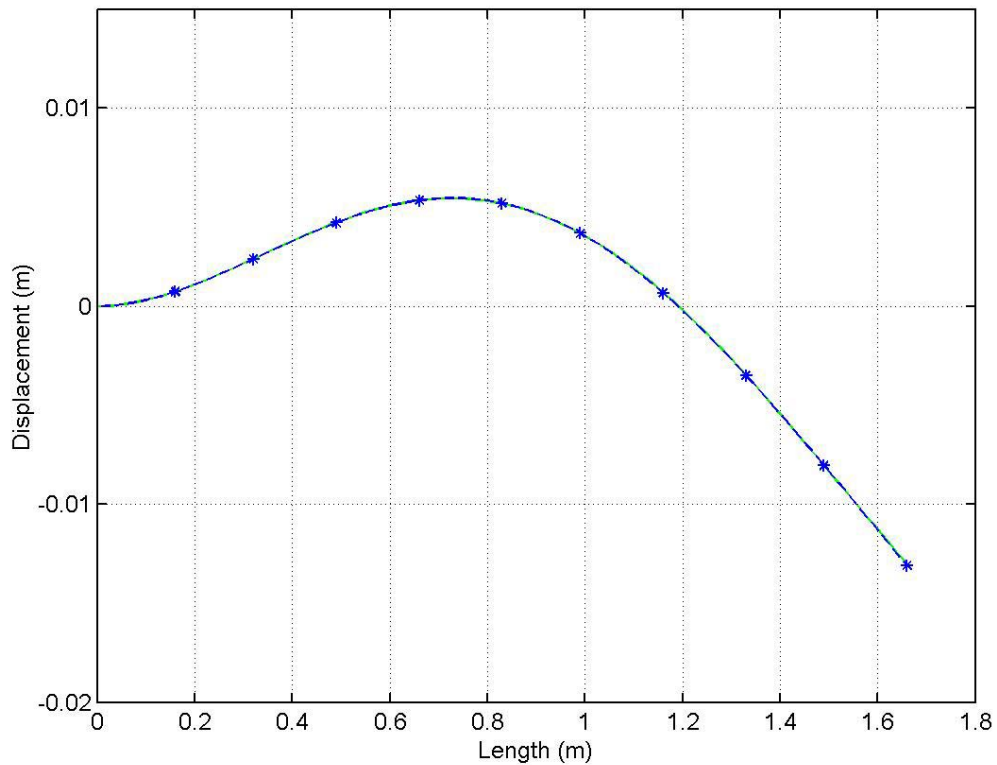
Figure 7.3: Shape comparison between the experimentally determined shape (—) and

the shape based on modal coefficients (*-)

Figure 7.4 displays the variation in the modal coefficients as a function of time.

As observed with the mode 1 excitation, the modal coefficients for extraneous modes

increase at times when the cantilever beam has a zero crossing. During other times, the

mode 2 coefficient is the dominant modal parameter.
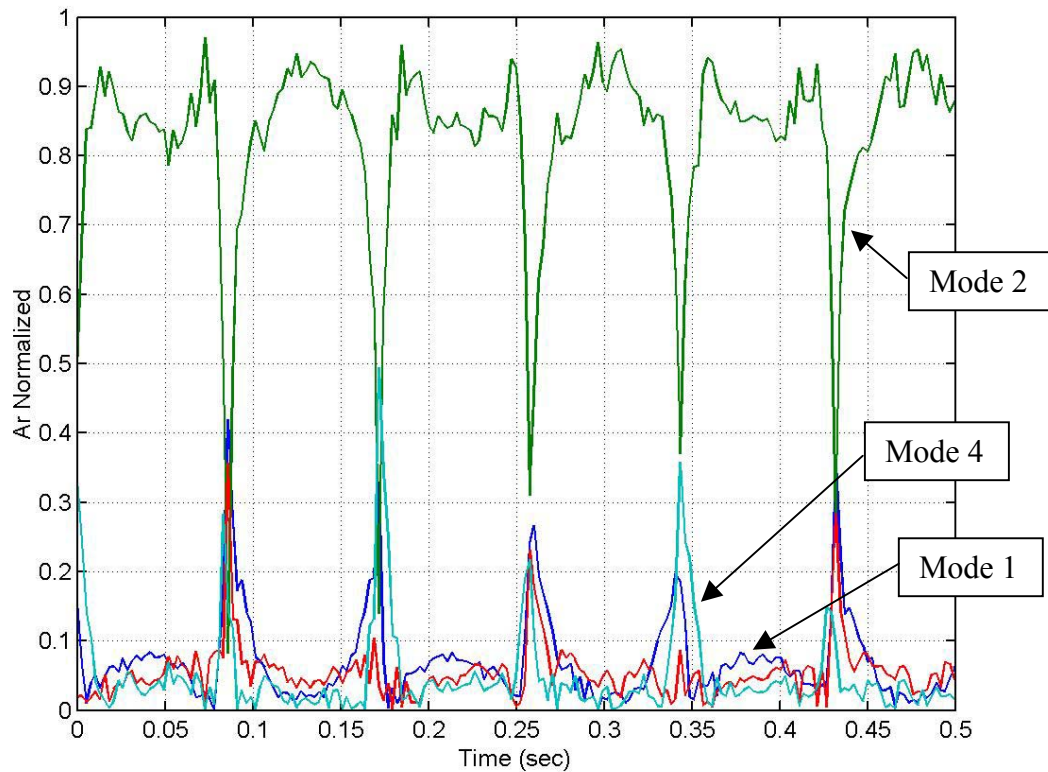
Figure 7.4: Modal coefficients versus time for mode 2 excitation

7.3.3   Mode 3 Vibration

The experimentally determined shape was processed with the modal analysis

technique to determine the modal coefficients of the first four modes. The A_r values for

an arbitrary time of the data set were determined to be: $A_r = [0.0411 \quad 0.0028 \quad \mathbf{0.9326}$

0.0235]. Figure 7.5 shows the comparison of the mode shape determined from the modal coefficients (A_r) and the experimental shape measurement. The error$_{10}$ value derived for this comparison is 1.989 e-4, which is an order of magnitude improvement compared to an error$_{10}$ value of 0.0028 found when the shape measurement is compared to the reference mode 3 shape in Section 6.3. Again, the tip region of the two shapes does not show good agreement, this is attributed to the arbitrary selection of four experimental data points along the beam length, which will be discussed further in Section 7.3.5.
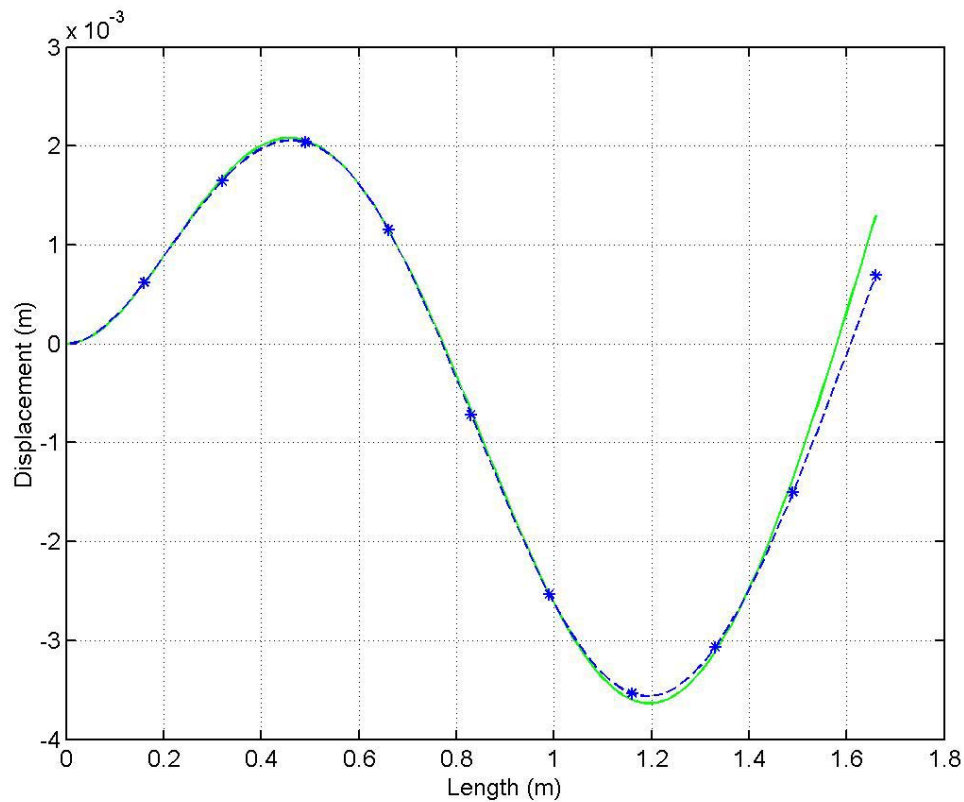

Figure 7.5: Shape comparison between the experimentally determined shape (——) and the shape using modal coefficients (*-)

Figure 7.6 displays the variation of the modal coefficients as a function of time through a few oscillations of the structure. The points when the third resonant mode coefficient decreases are associated with the zero crossings of the beam. There are instances when the second and fourth modes increase their respective modal participation, as indicated in the figure.
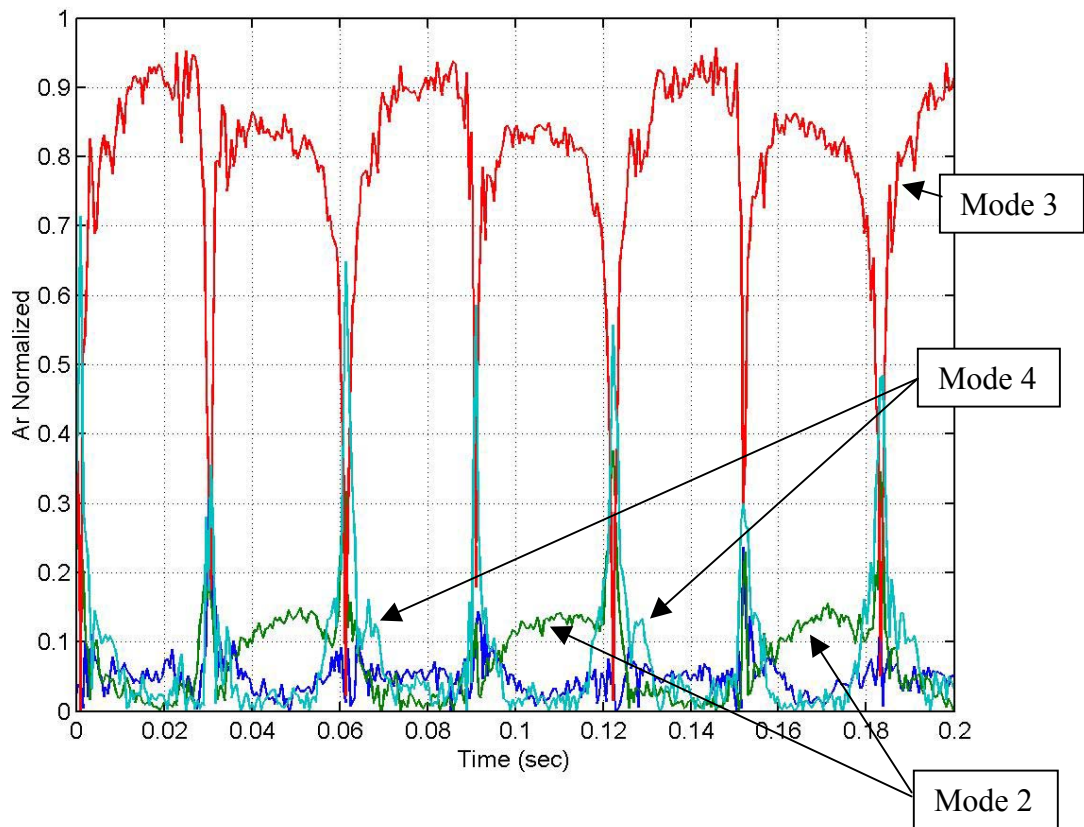
Figure 7.6: Modal coefficients versus time for mode 3 excitation

7.3.4 Mode 4 Vibration

Based on the data analysis of Section 6.4, the modal parameters for the fourth mode vibration should have an influence from the second and third modes with the strongest influence from the fourth mode. The experimentally determined shape was processed with the modal analysis technique to determine the modal coefficients of the first four modes. The A_r values for this case were determined to be: A_r = [0.0149 0.1089 0.0805 **0.7958**]. As suggested, there is also influence observed from the second and third modes at this time. Figure 7.7 displays the comparison between the experimentally determined shape and the mode shape using the modal coefficients. This comparison yields an error$_{10}$ value of 9.36 e-5. Although this error$_{10}$ value indicates an accurate match, there are differences between the two shapes along the latter half of the beam. This is attributed to using only four data points and hence only four modes to determine the modal coefficients. Increasing the number of modes incorporated in the modal analysis provides a more accurate representation. For example, increasing the modal analysis to eight modes yields an error$_{10}$ value of 4.85 e-5 with modal coefficients of A_r = [0.0131 0.1031 0.0594 **0.6919** 0.0036 0.0404 0.0446 0.0437]. Also, a more accurate representation is obtained by incorporating more data points in the modal analysis technique while maintaining the same number of modes. This methodology is discussed further in Section 7.4.
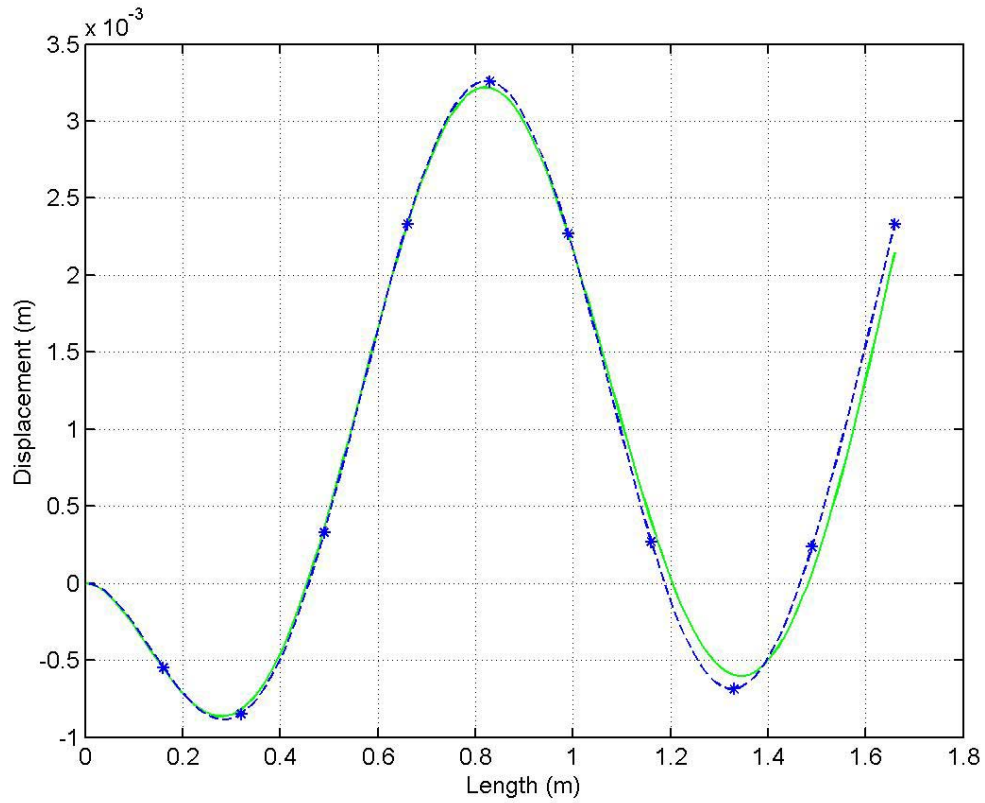
Figure 7.7: Shape comparison between the experimentally determined shape (—) and

the shape using modal coefficients (*-)

Figure 7.8 shows the modal coefficient variation through a few oscillations of

the cantilever beam being excited at the fourth resonant frequency. Although mode 4

remains dominant throughout the vibration, the figure also shows a strong response

from mode 2 and mode 3.
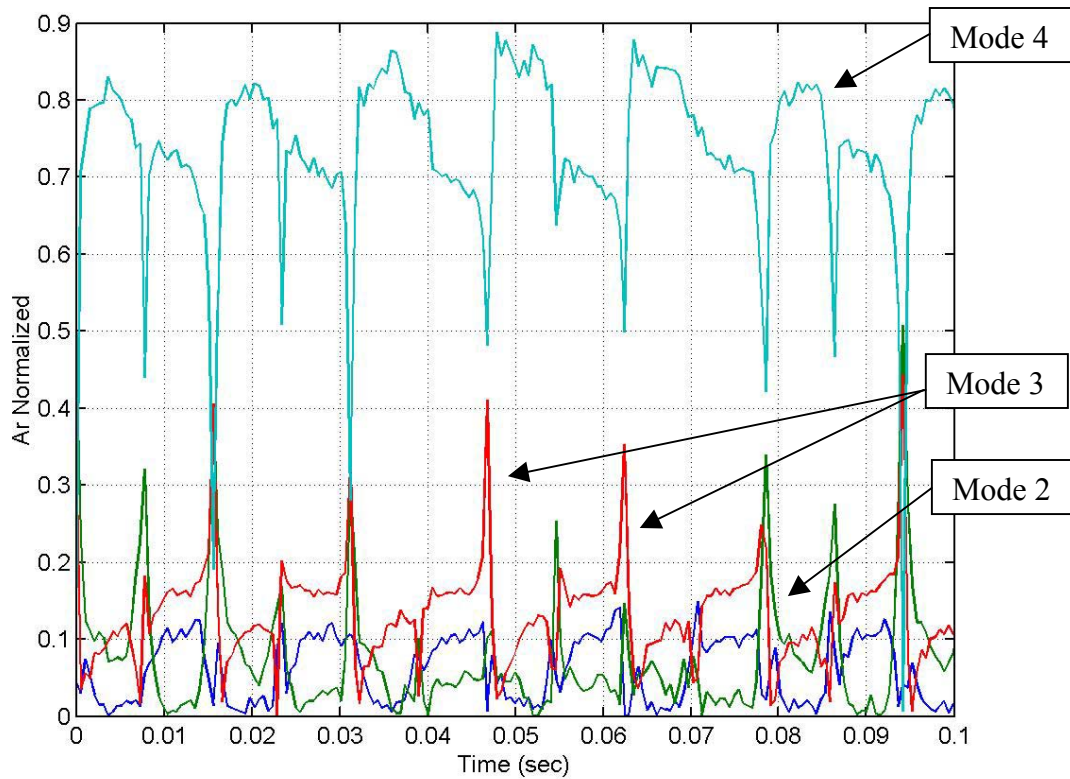
Figure 7.8: Modal coefficients versus time for mode 4 excitation

7.3.5 Mode 5 Vibration

Experimental shape data for the fifth mode excitation frequency was processed, and at a particular time of the data the following modal coefficients were determined: A_r = [0.0180 0.0035 0.0733 0.0174 **0.6161** 0.0127 0.1133 0.1456]. Figure 7.9 shows the shape comparison between the experimentally determined shape and the shape based on the modal coefficients. The $error_{10}$ value calculated from the comparison between the experimental shape and the theoretical modal coefficient shape is 3.2 e-6.

The stars along the modal coefficient shape represent the 8 locations that were used for the modal analysis algorithm.
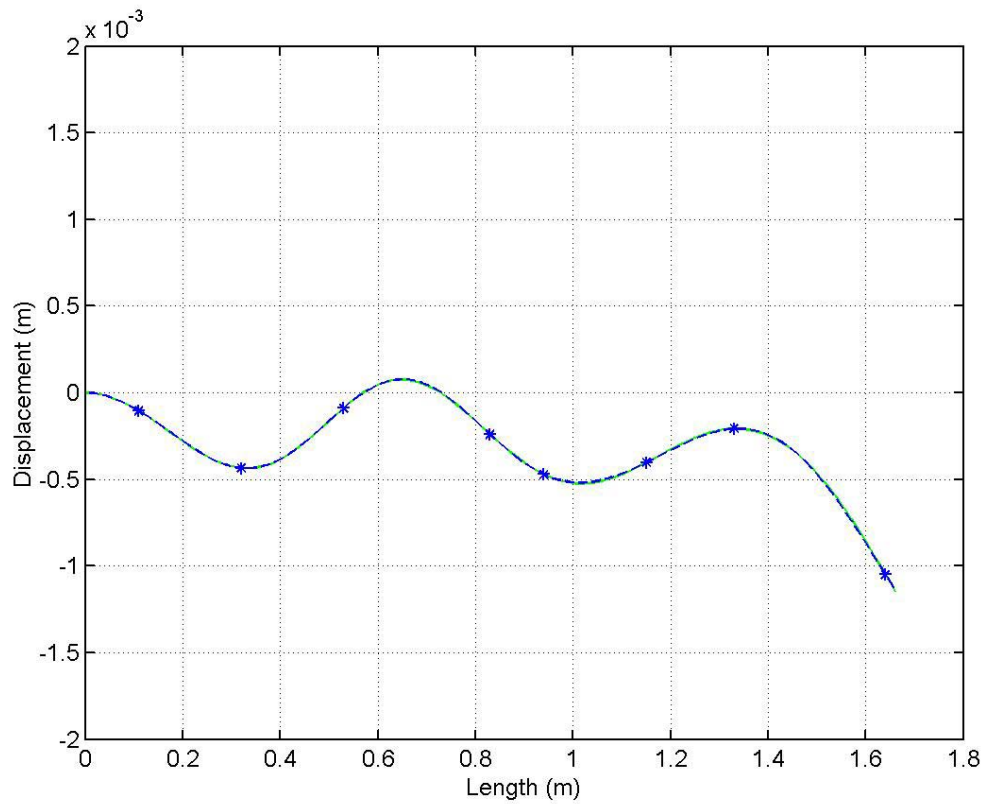
Figure 7.9: Shape comparison between the experimentally determined shape (—) and the shape using modal coefficients (*-)

An interesting case was observed when only seven mode shapes were used for the same test case. In limiting the analysis to seven modes, the last data point along the structure was removed from the analysis case. This created a situation in which the deflection data being processed by the modal coefficient determination algorithm was insufficient to accurately obtain the modal parameters. As illustrated in Figure 7.10, the

modal coefficient shape no longer matches the experimental shape at the end of the structure with an $error_{10}$ value for the comparison of 0.0015. The A_r values for this case were determined to be A_r = [0.0820   0.0808   0.1452   0.2644   **0.0234**   0.2513 0.2269]. Therefore, the square matrix inverse method of determining the modal coefficients is highly dependent on the location of the points used for the analysis, as alluded to previously. As the sensors need to be distributed along the structure's span, so must the points used to determine the modal coefficients.
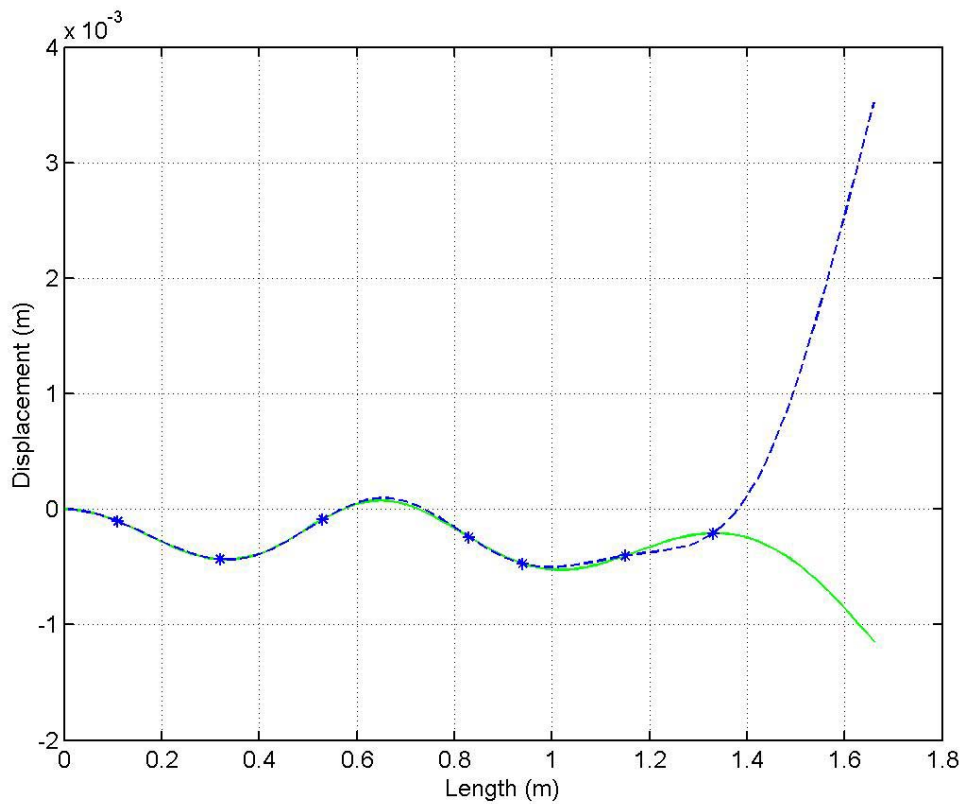

Figure 7.10: Shape comparison between the experimentally determined shape (——) and the shape using with modal coefficients (*-)

148

A different seven points were used to examine this effect, moving the second location to the end of the structure and determining the modal coefficients. The modal coefficients for this case are: $A_r = [0.0169 \quad 0.0001 \quad 0.0741 \quad 0.0333 \quad \mathbf{0.5905}$ $0.0641 \quad 0.2210]$ with an $error_{10}$ value of 3.48 e-5, which is an order of magnitude higher than the $error_{10}$ value found when using 8 mode shapes and 8 points along the beam. Based on the results of this section, the use of more data points and more modes to determine the modal coefficients leads to a better determination of the modal coefficients. The concept of using many more data points than modes of interest is investigated through the use of a pseudo-inverse method in Sections 7.4 and 7.5.
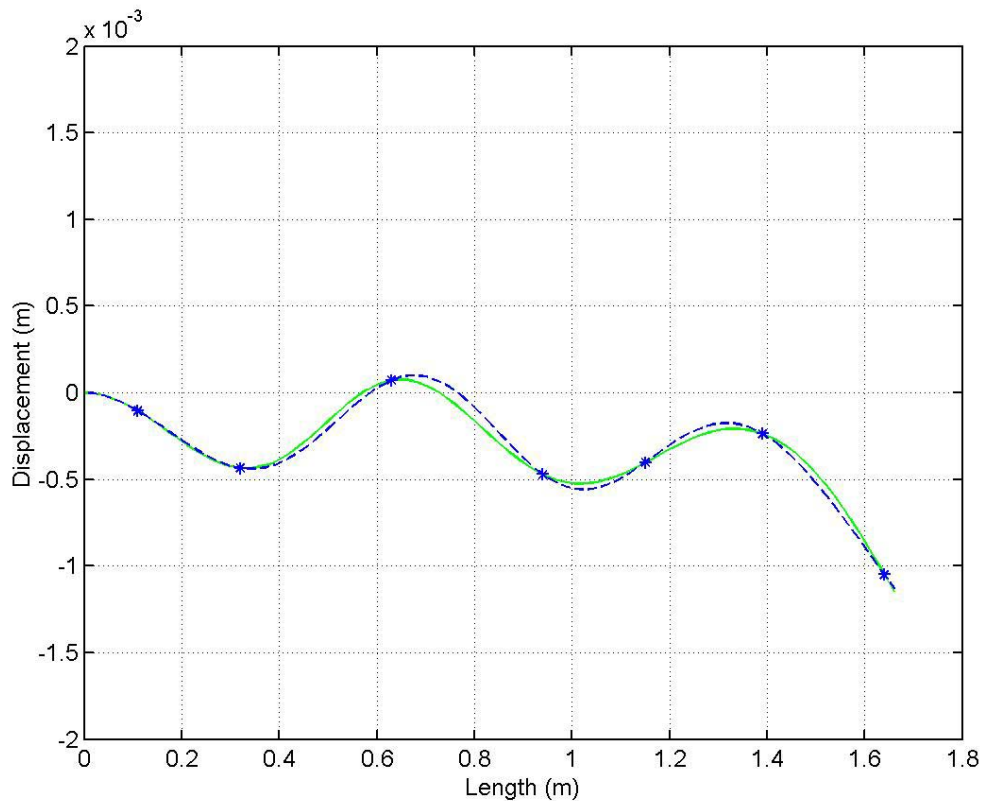

Figure 7.11: Shape comparison between the experimentally determined shape (——) and the shape using modal coefficients (*-)

149

The modal coefficient variation during a few oscillations of the cantilever beam is shown in Figure 7.12. The mode 5 coefficient is shown to be dominant through the beam's vibration with significant influences from mode 7 and mode 8.
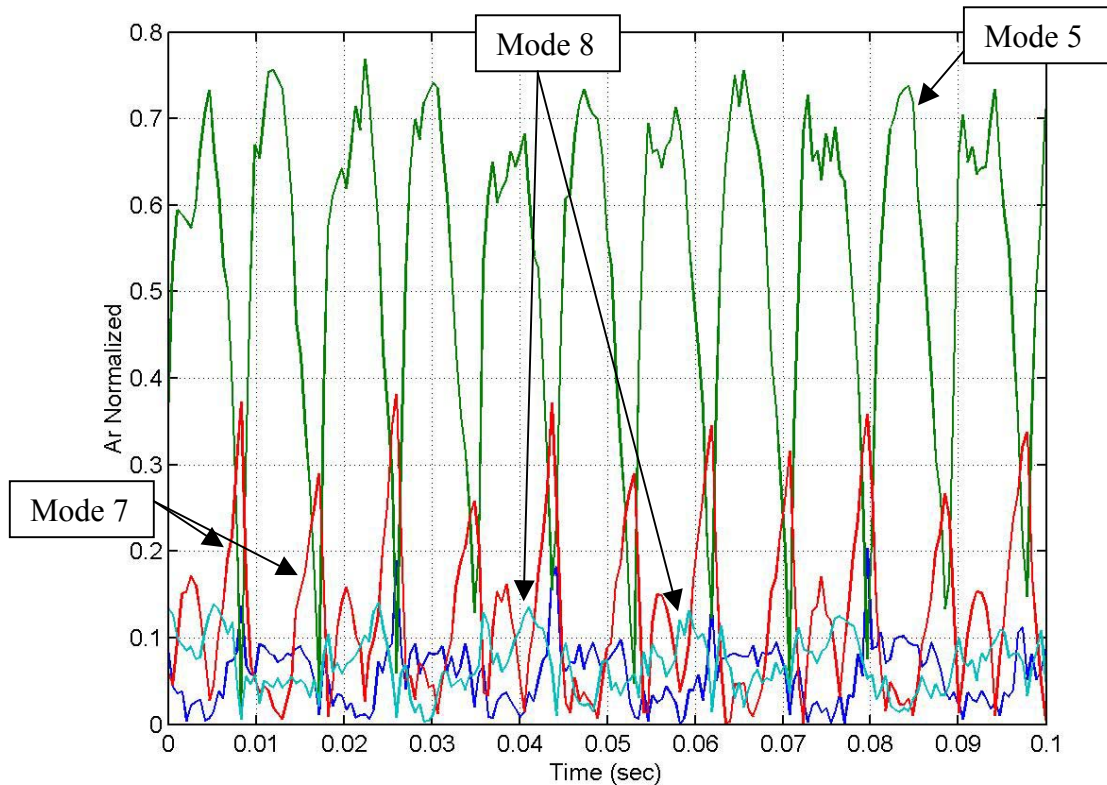
Figure 7.12: Modal coefficients versus time for mode 5 excitation

7.4 Modal Influence Determination using the Pseudo-Inverse Method

As stated in Section 7.1, the number of data points included in the modal coefficient analysis must be equivalent to the number of modes of interest for the inverse of the **H** matrix to be determined. This section examines increasing the number

of data points from the experimental shape data used in the modal analysis method for a limited number of modes using a pseudo-inverse technique. If the number of data points used to determine the modal coefficients for an m number of modes is represented by n, then Equation 7.8 is written as:

$$[H]_{n \times m} [A]_{m \times 1} = [Y]_{n \times 1} \tag{7.11}$$

A pseudo-inverse method may be employed to determine the A_r values from the case of n>m. Both sides of Equation 7.11 are multiplied by the transpose of the **H** matrix.

$$[H]^T [H][A]_{m \times 1} = [H]^T [Y]_{n \times 1} \tag{7.12}$$

The combination $[H]^T [H]$ is a square matrix (m x m) and the inverse can be determined in the usual way. This leads to the determination of the modal coefficients as

$$[A]_{m \times 1} = \left([H]^T [H]\right)^{-1}_{m \times m} [H]^T_{m \times n} [Y]_{n \times 1} \tag{7.13}$$

where $\left([H]^T [H]\right)^{-1}$ is the pseudo-inverse of the H matrix.

Using the pseudo-inverse, more data points can be included in the modal coefficient determination algorithm to provide a more robust analysis. As discussed in Section 7.3.5, the end point of the experimentally determined shape should be included in the analysis. Hence, the points used for the pseudo-inverse calculations were uniformly distributed across the structure's span and included the end point of the structure.

7.5 Experimental Data Modal Analysis using Pseudo-Inverse

This section reexamines the experimental data presented in Section 7.3 using the pseudo-inverse method. The $error_{10}$ values obtained from the pseudo-inverse method were observed to be lower compared to the square matrix method values given in Section 7.3. For each excitation case (mode 1 through mode 5), the number of data points included in the pseudo-inverse method, was set to 10, 50, 100, and 167 (the maximum number of data points from the shape measurement algorithm for the experimental case). The results for each excitation case are provided in Table 7.1 through Table 7.5. There were small changes between the $error_{10}$ values when using different numbers of data points in the modal analysis, but because of the extremely small magnitude of these numbers the changes are considered insignificant. Typical $error_{10}$ results are provided for the mode 1 case in Table 7.1, and only a single $error_{10}$ value is provided for the remaining excitations. Figure 7.13 through Figure 7.17 display the results from the modal analysis of the each excitation case using the pseudo-inverse method with 50 data points. In all cases, the comparison between the experimental shape and the shape using the modal coefficients is improved compared to the square inverse method discussed in Section 7.3.
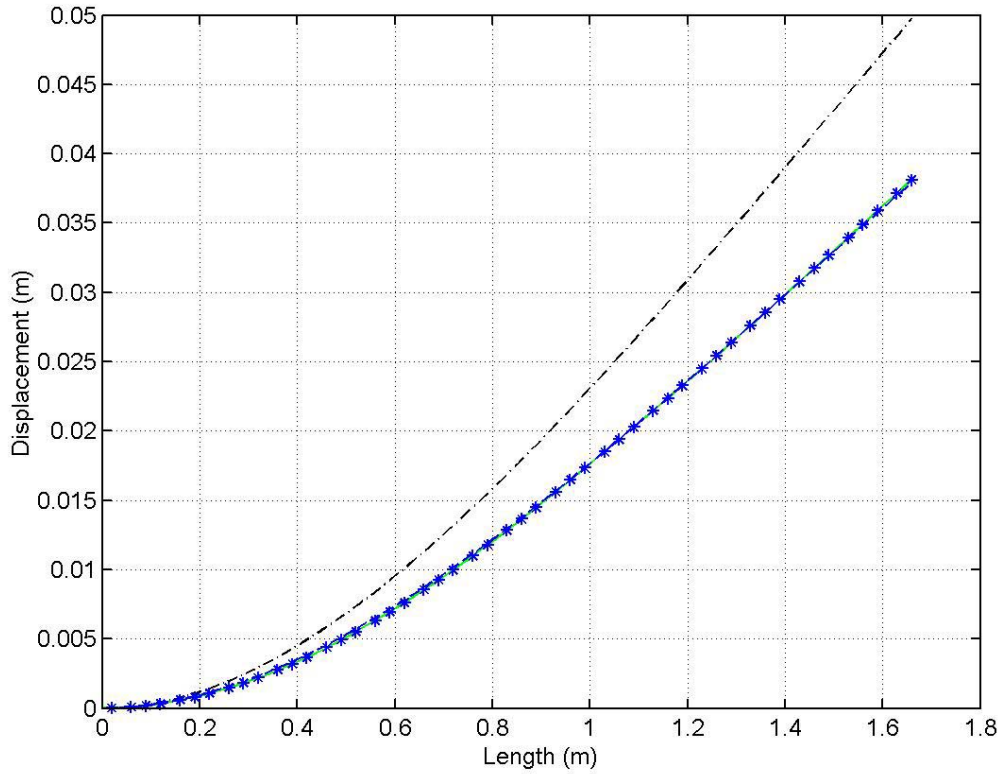
Figure 7.13: Shape comparison for pseudo-inverse modal analysis case, mode 1 excitation; reference mode 1 (-··-), experimental shape (——), shape using modal coefficients (*-)

	A_1	A_2	A_3	A_4	$error_{10}$
10 Data Points	0.9898	0.0027	0.0026	0.0049	1.301 e-4
50 Data Points	0.9900	0.0026	0.0028	0.0046	1.288 e-4
100 Data Points	0.9900	0.0026	0.0028	0.0045	1.285 e-4
167 Data Points	0.9900	0.0026	0.0028	0.0045	1.285 e-4

Table 7.1: Modal coefficients for mode 1 excitation using pseudo-inverse technique

The error$_{10}$ value for the mode 2 excitation case was determined to be 2.64 e-5, which is lower than the value determined from the square inverse method.
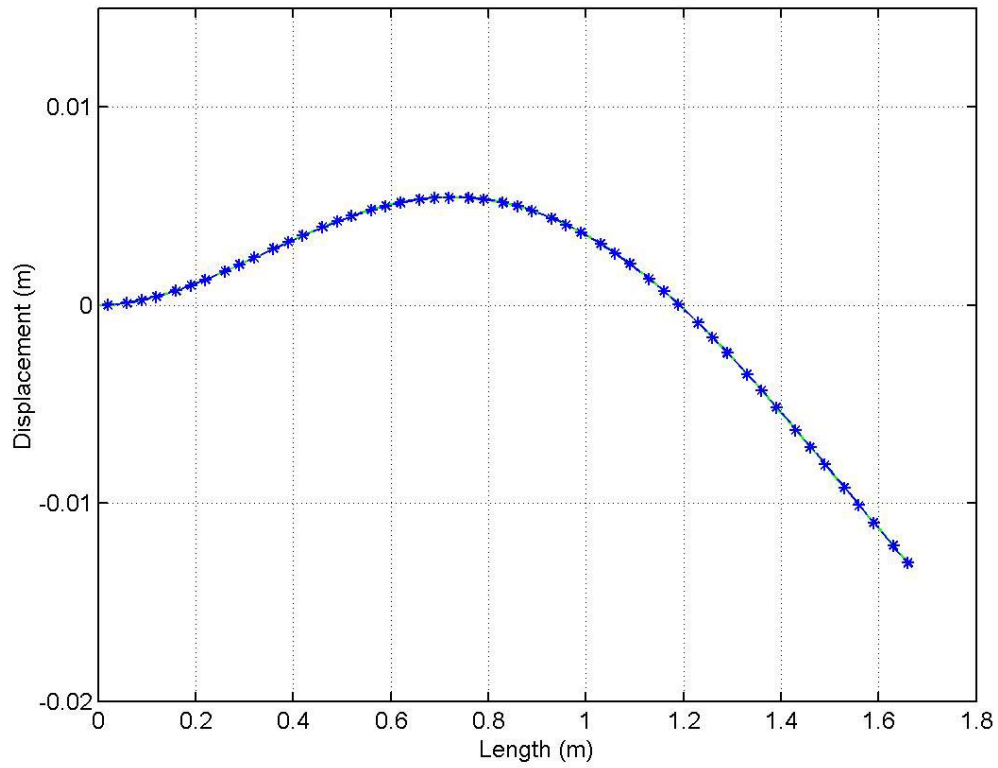
Figure 7.14: Shape comparison for pseudo-inverse modal analysis case, mode 2; experimental shape (——) and shape using modal coefficients (*-)

	A_1	A_2	A_3	A_4
10 Data Points	0.0645	0.9175	0.0065	0.0116
50 Data Points	0.0644	0.9151	0.0039	0.0167
100 Data Points	0.0643	0.9147	0.0034	0.0175
167 Data Points	0.0643	0.9145	0.0033	0.0179

Table 7.2: Modal coefficients for mode 2 excitation using pseudo-inverse technique

The $error_{10}$ value for the mode 3 case was determined to be 4.51 e-5, which is lower than the value determined from the square inverse method. The shape comparison shown in Figure 7.15 demonstrates the increased accuracy of the comparison, especially at the beam tip region.
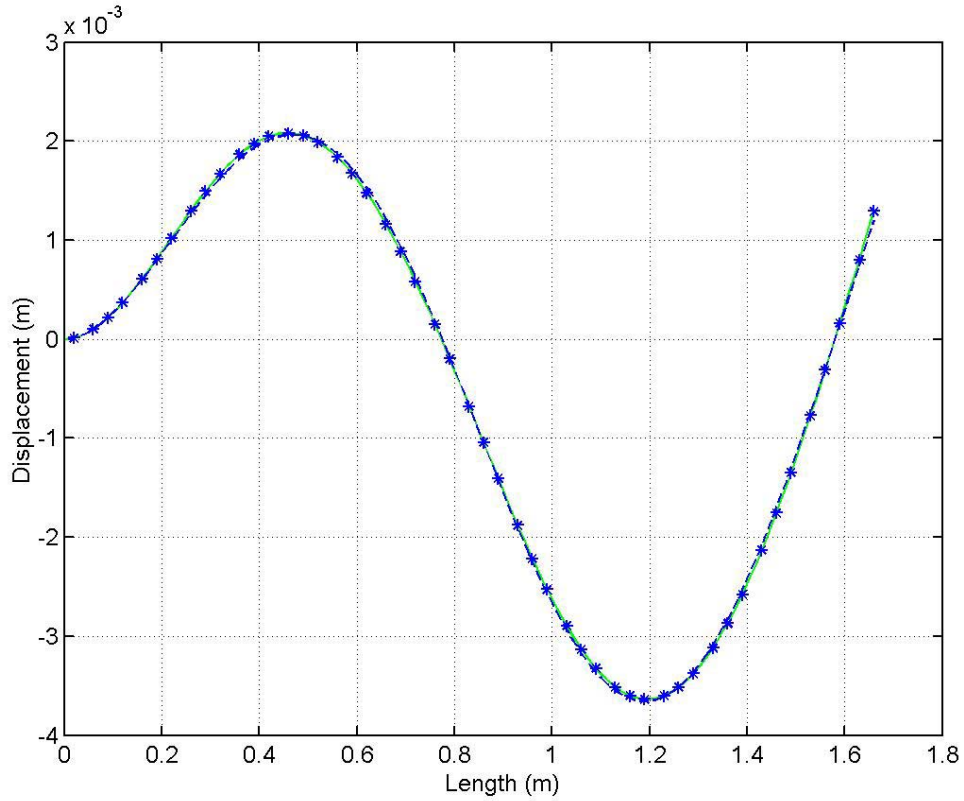
Figure 7.15: Shape comparison for pseudo-inverse modal analysis case, mode 3;

experimental shape (—) and shape using modal coefficients (*-)

	A_1	A_2	A_3	A_4
10 Data Points	0.0341	0.0152	0.8676	0.0831
50 Data Points	0.0347	0.0142	0.8743	0.0768
100 Data Points	0.0348	0.0140	0.8755	0.0757
167 Data Points	0.0348	0.0140	0.8759	0.0753

Table 7.3: Modal coefficients for mode 3 excitation using pseudo-inverse technique

156

The error$_{10}$ value for the mode 4 case was determined to be 5.09 e-5, which is a lower value compared to the square inverse method. As with the mode 3 case, the shape comparison is improved along the end of the beam as compared to the square inverse method shown in Section 7.3.
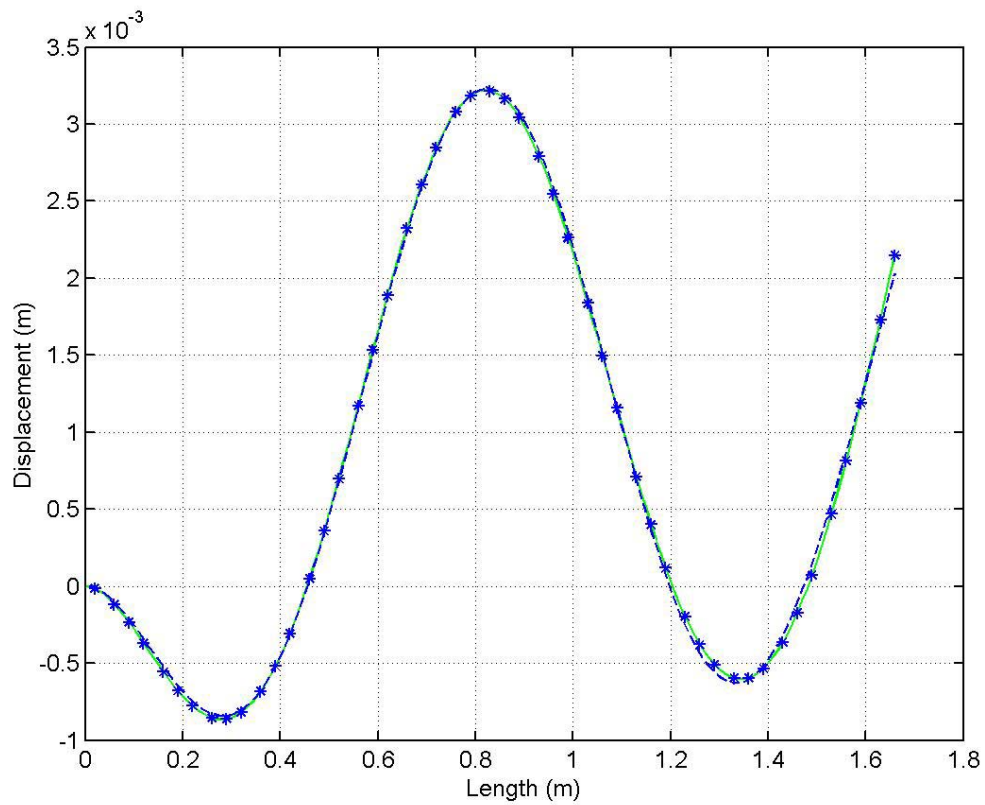

Figure 7.16: Shape comparison for pseudo-inverse modal analysis case, mode 4; experimental shape (——) and shape using modal coefficients (*-)

	A_1	A_2	A_3	A_4
10 Data Points	0.0151	0.1172	0.0708	0.7969
50 Data Points	0.0151	0.1196	0.0679	0.7974
100 Data Points	0.0150	0.1200	0.0675	0.7975
167 Data Points	0.0150	0.1201	0.0673	0.7976

Table 7.4: Modal coefficients for mode 4 excitation using pseudo-inverse technique

The $error_{10}$ value for the mode 5 case was determined to be 1.6 e-6, which is one-half the value determined from the square inverse method. The lower $error_{10}$ values for the mode 5 case ($\sim 10^{-6}$) are partially attributed to the low amplitude of the structure's vibration. The maximum amplitude for this case is approximately 1 mm, where for mode 4 it is approximately 3 mm and higher for the lower order modes. The modal coefficients for modes 7 and 8 are significant compared to the other neighboring modes as expected from the FFT data presented in Section 6.5.
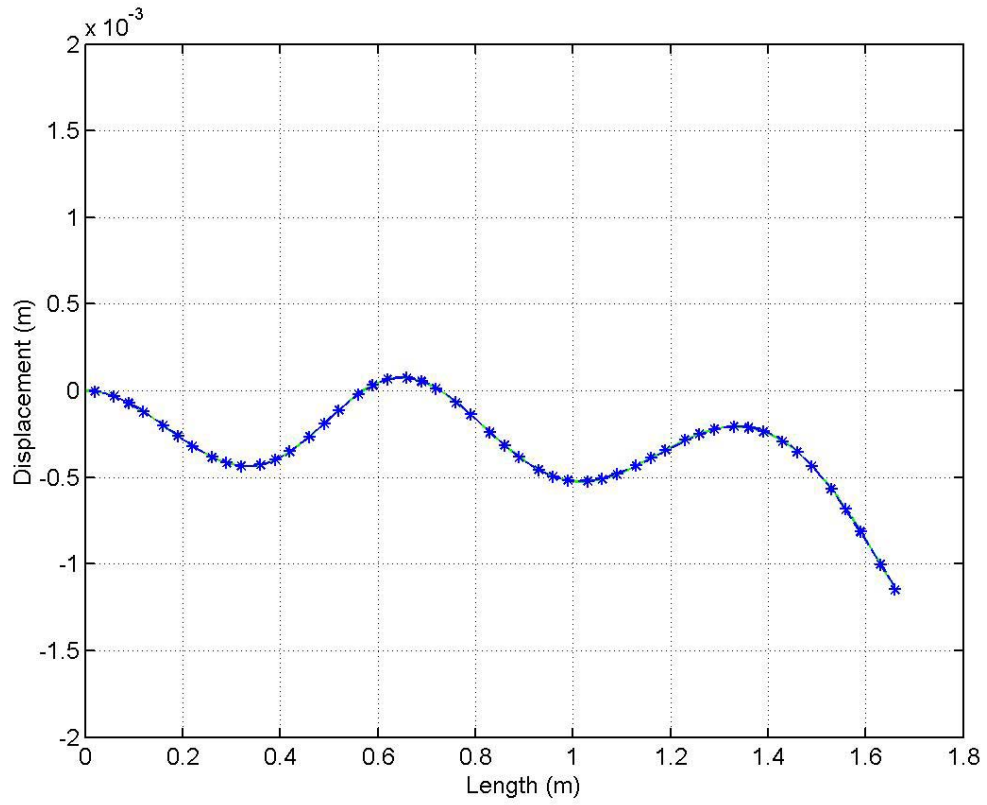
Figure 7.17: Shape comparison for pseudo-inverse modal analysis case, mode 5;

experimental shape (——) and shape using modal coefficients (*-)

	A_1	A_2	A_3	A_4	A_5	A_6	A_7	A_8
10 Data Points	0.0180	0.0038	0.0729	0.0180	0.6126	0.0149	0.1025	0.1573
50 Data Points	0.0180	0.0041	0.0724	0.0193	0.6137	0.0119	0.1053	0.1552
100 Data Points	0.0180	0.0042	0.0724	0.0197	0.6141	0.0112	0.1065	0.1540
167 Data Points	0.0180	0.0042	0.0723	0.0198	0.6142	0.0109	0.1068	0.1537

Table 7.5: Modal coefficients for mode 5 excitation case using pseudo-inverse technique

7.6 Summary of Modal Analysis

This chapter analyzed the experimental shape data discussed in Chapter 6 using modal analysis techniques. Both a square inverse method, where the number of input data points equaled the number of modes of interest, and a pseudo-inverse method, where the number of data points exceeded the number of modes of interest, were investigated. The pseudo-inverse method demonstrated a higher accuracy in matching the experimental shape data with the shape formed using the modal coefficients. Increased accuracy was also obtained when more modes were included in the analysis, as demonstrated with the mode 4 and mode 5 cases. These analysis methods demonstrate a novel use of FBG sensors to monitor continuous changes in the modal response characteristics of a structure with respect to time.

8 Conclusions

This research has investigated the shape measurement of dynamic systems. The

shape measurement system developed herein consists of a multiplexed fiber optic

sensor system, a shape determination algorithm based on Frenet frames, and a signal

processing method based on modal analysis techniques. Distributed strain

measurements were obtained from a vibrating structure via a multiplexed FBG sensor

system. These strain measurements were used to determine the curvature of the

structure at the FBG sensor locations, and the curvature values were processed with a

Frenet frame algorithm to determine the shape of the structure. In the experimental

setup, a cantilever structure ($65.625 \times 2.0 \times 0.125$ inches, 6061 aluminum) was

subjected to a base excitation force input by using a mechanical shaker. The base of the

structure was mounted on a linear translation stage to allow motion in the transverse

direction. Strain data was recorded from 8 surface mounted FBG sensors distributed

along the length of the structure. Strain data from these sensors were collected up

through the first seven modal components of the cantilever beam. Processing of the

strain data using the Serret-Frenet frame shape measurement method showed a good

qualitative match between the experimental shape and the theoretical mode shape for

excitation frequencies up to the fifth modal component. Differences between the experimental and theoretical mode shapes are explained by influences of neighboring modes. Modal analysis techniques were used to examine the shape measurement data to determine the influence of the various resonant modes on the vibration of the cantilever beam; these techniques were demonstrated as a unique tool for analyzing the temporally resolved dynamic response of a structure.

The conclusions drawn from this multidisciplinary research concern the fiber optic sensor system, the shape measurement algorithm, and the results from the modal analysis method used to examine the data. The research demonstrated that the design of the FBG sensor requires knowledge of the expected strain range, the available optical bandwidth, and effective methods for processing the FBG sensor signals. Careful planning of the FBG center wavelengths is important to avoid sensor overlap or sensor crosstalk in the fiber optic sensor system. The Taylor series approximation used in the shape measurement algorithm is inaccurate at high strain gradients, which become critical for higher modes. This effect was not observed for the excitation cases considered in the research. An error experienced in this research effort was due to an inadequate number of sensors available for sensing higher modes.

A primary contribution of this research is the demonstration of the shape measurement technique for determination of the modal influence coefficients related to the characteristic modal properties of a vibrating structure. The framework for the investigations leading to this contribution is illustrated in Figure 8.1. The cantilever

beam demonstrated that the modal coefficients vary with respect to time for the resonant excitation cases examined. The modal analysis technique provides a measure of the relative influence of each mode for each instant of time during the recorded data set. Results from the modal analysis method depend on the selection of input values; in particular, for the square inverse method. For the modal analysis, it must be ensured that an adequate sampling of deflection points along the structure is used to recreate the deflection using modal analysis. Also, an appropriate number of neighboring modes must be included in the modal analysis to determine an accurate representation of the modal characteristics of the structure. The pseudo-inverse modal analysis method provides more accurate results than the square inverse method due to the inclusion of more points along the structure.
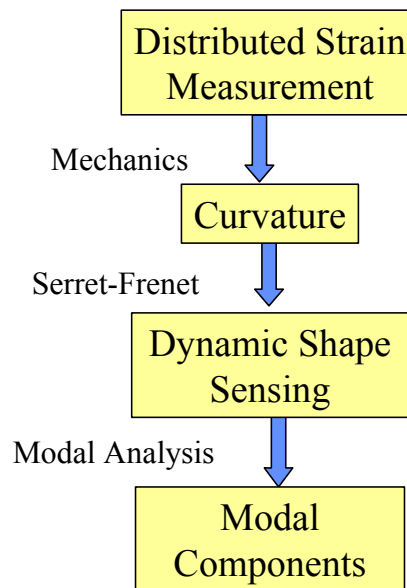
Figure 8.1: Framework for the investigations discussed in this dissertation

It is recognized that there are other methods for performing shape measurement from distributed strain measurements, such as double integration of the strain mode shape data. A goal of this research was to demonstrate the effectiveness of the Serret-Frenet frame methodology for the cantilever structure case, not to justify its accuracy compared to another method. The Serret-Frenet frame technique is considered to be useful when examining more complex structures such as cables (or hoses) which need to be modeled as space curves.

Future research concerning the shape measurements may be expanded to the analysis of more complex structures, such as cables and plates. Cables can be viewed as space curves, which should fit well into the Serret-Frenet frame formularization. Plates are not as amenable to Serret-Frenet analysis because they do not resemble a space curve. The shape measurement method has been applied for measuring the static deflections of plate structures by analyzing the plate as multiple beams placed side-by-side [Baldwin, Salter, and Kiddy, 2004].

The shape measurement system demonstrated in this dissertation provided a post-processing method of obtaining the modal coefficients for a dynamically moving structure by using modal analysis techniques. A possible future improvement would be real-time data processing to provide real-time determination of a structure's dynamic shape. This type of real-time analysis may be useful for applications of health monitoring where changes in the modal coefficients may lead to indications of damage to the structure.

Appendix A: Deriving Curvature from Vector Relations

The shape calculation is based on curvatures values derived from the recorded strain data. It was shown in Section 3.2 how the curvature data is used to map the deflection of the cantilever structure using the curvature data and Frenet frames (vector relations). This appendix demonstrates the equivalent relationship between mechanics-based curvature relations and vector calculus curvature relations.

Curvature in the mechanics sense is a function of the shape of a surface. If the surface is flat the radius of curvature is infinite and the curvature value is zero (curvature is the reciprocal of radius of curvature). The well known relationship between curvature (κ) and the shape of the surface defined by the variable 'y' is given as [Beer and Johnston, 1981]:

$$\kappa = \frac{y''}{\left(1 + y'^2\right)^{3/2}}$$
(A.1)

This relationship is often simplified for small deflections of relatively flat surfaces as $\kappa = y''$.

Curvature in terms of vector calculus is often discussed in terms of velocity ($\mathbf{v}$) and acceleration ($\mathbf{a}$) of space curves [Thomas Finney, 1992].

$$\kappa = \frac{|\mathbf{v} \times \mathbf{a}|}{|\mathbf{v}|^3} = \frac{|\mathbf{r}'(t) \times \mathbf{r}''(t)|}{|\mathbf{r}'(t)|^3}$$
(A.2)

where $\mathbf{r}$ is the space vector following the space curve as a function of the parametric variable time (t). The differentials in Equation A.2 can be written as spatial derivatives

of the x, y, and z components of **r**, where $\mathbf{r}'(t) = \left[x_p, y_p, z_p \right]$ and $\mathbf{r}''(t) = \left[x_{pp}, y_{pp}, z_{pp} \right]$

where the subscript p represents differentiation to a common spatial variable. Thus Equation A.2 becomes:

$$\kappa = \frac{\left| \left[x', y', z' \right] \times \left[x'', y'', z'' \right] \right|}{\left| \left[x', y', z' \right] \right|^3} \tag{A.3}$$

Performing the vector calculations in Equation A.3 leads to:

$$\kappa = \frac{\sqrt{\left(y'z'' - y''z' \right)^2 + \left(x'z'' - x''z' \right)^2 + \left(x'y'' - x''y' \right)^2}}{\left(x'^2 + y'^2 + z'^2 \right)^{3/2}} \tag{A.4}$$

For the case of a cantilever beam, $x' = 1$, $x'' = z' = z'' = 0$, leading to:

$$\kappa = \frac{y''}{\left(1 + y'^2 \right)^{3/2}} \tag{A.5}$$

which is the same equation as given by the mechanics based model in Equation A.1.

Appendix B: Additional Data from Chapter 6 Evaluations

B.1 Mode 6 Testing: Excitation Frequency Close to the Sixth Natural Frequency

Figure B.1 displays the comparison between the reference mode 6 shape and the experimentally determined shape. The experimentally determined shape does not resemble a mode 6 shape and an $error_{10}$ value of 0.0075 was determined for this comparison.
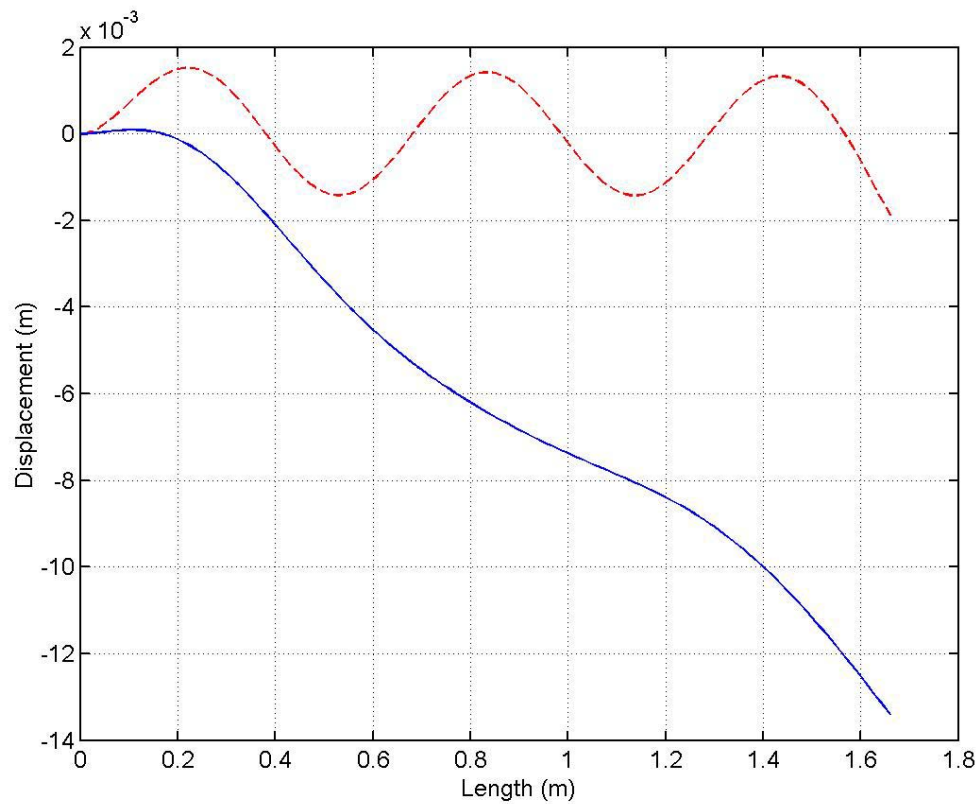

Figure B.1: Mode 6 reference mode shape (--) and experimental shape (—) at a maximum deflection point
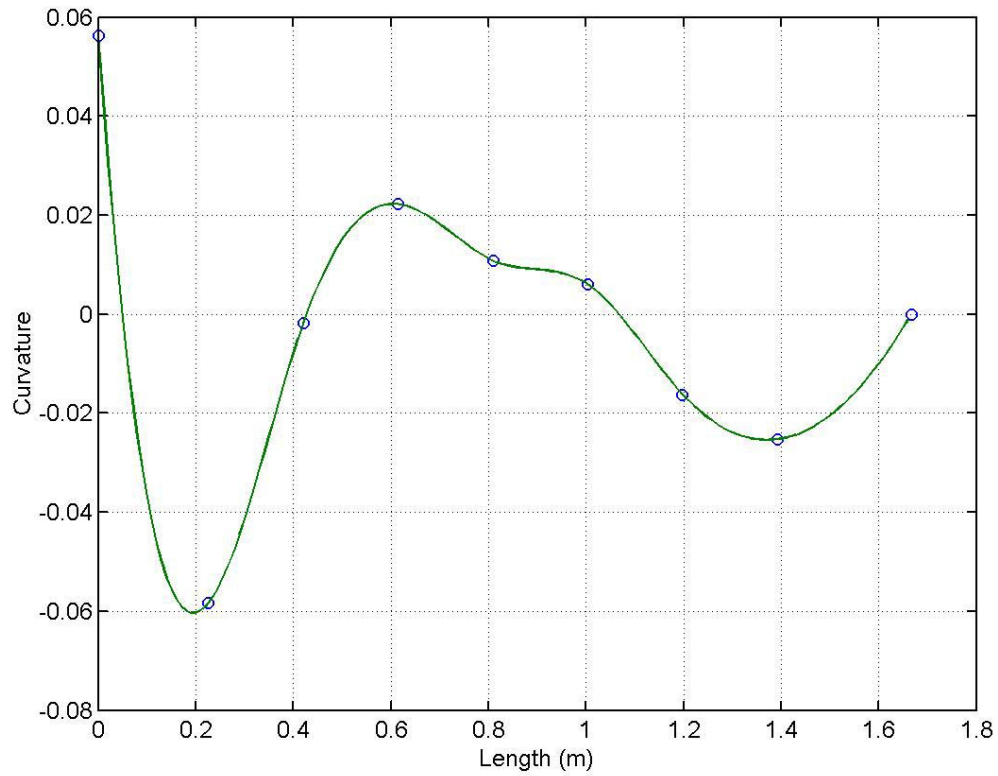
Figure B.2: Mode 6 curvature data and positions of FBG sensors

The curvature data for the mode 6 test shown in Figure B.2 does not resemble a mode 6 curvature function. Examining the strain data for sensor #1 in Figure B.3 and Figure B.4 demonstrates that the beam was not experiencing a mode 6 vibration state during this test. Many other modal components were evident, as will be shown in the FFT data.
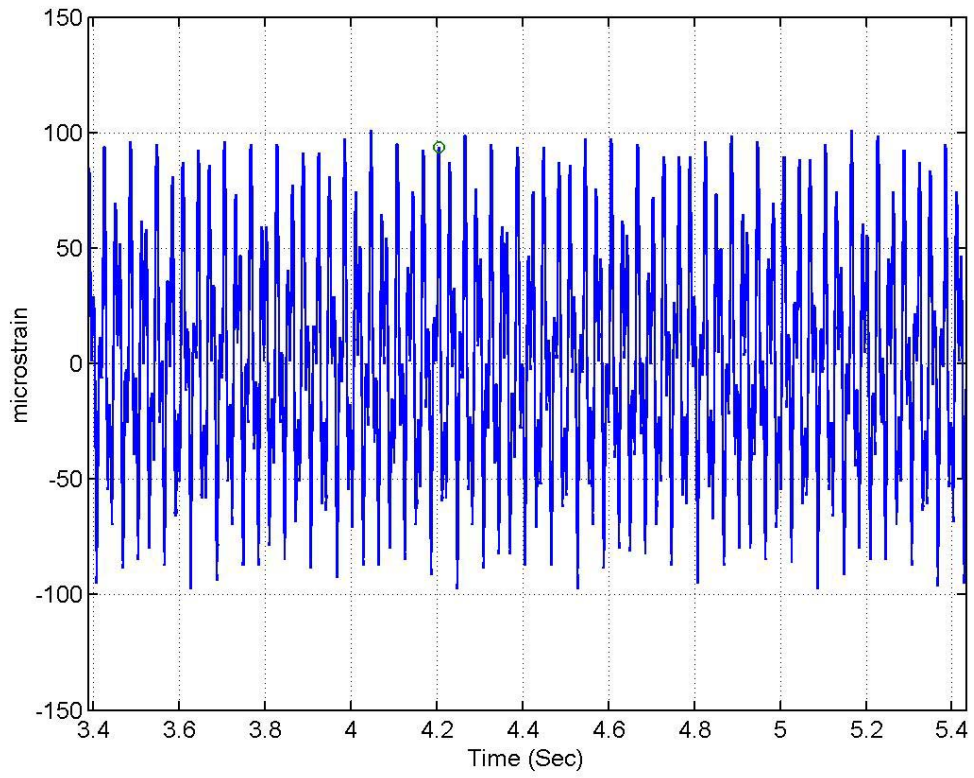
Figure B.3: Time trace for a FBG sensor during the mode 6 excitation
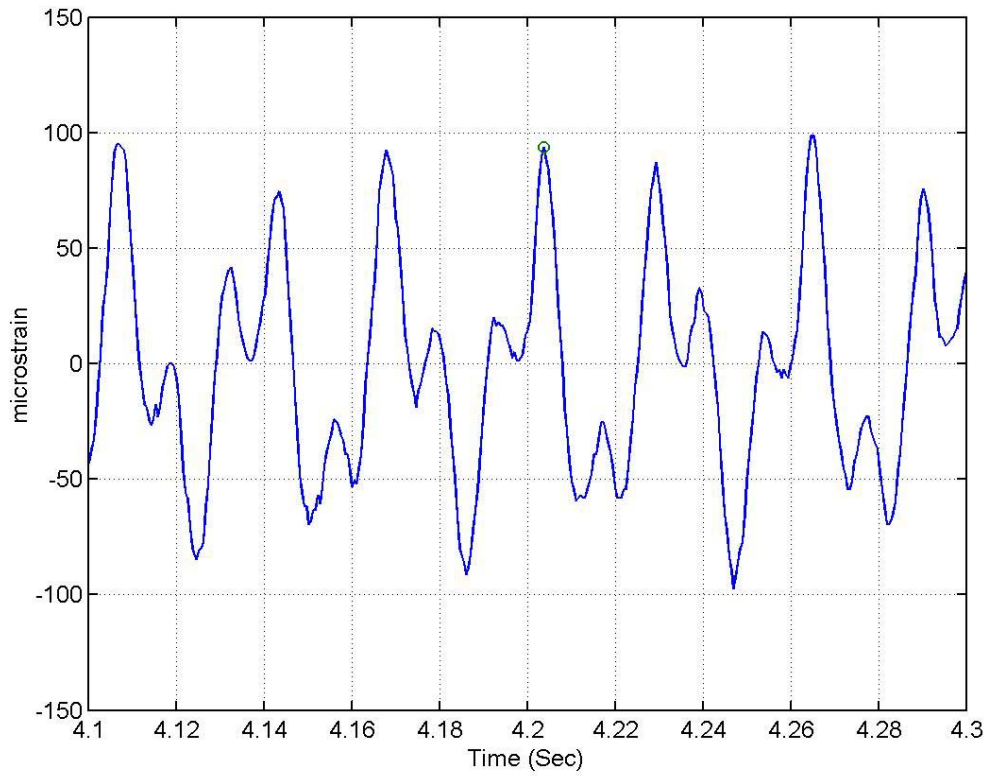
Figure B.4: Time trace for the same FBG sensor as shown in Figure B.3 with a shorter

time scale
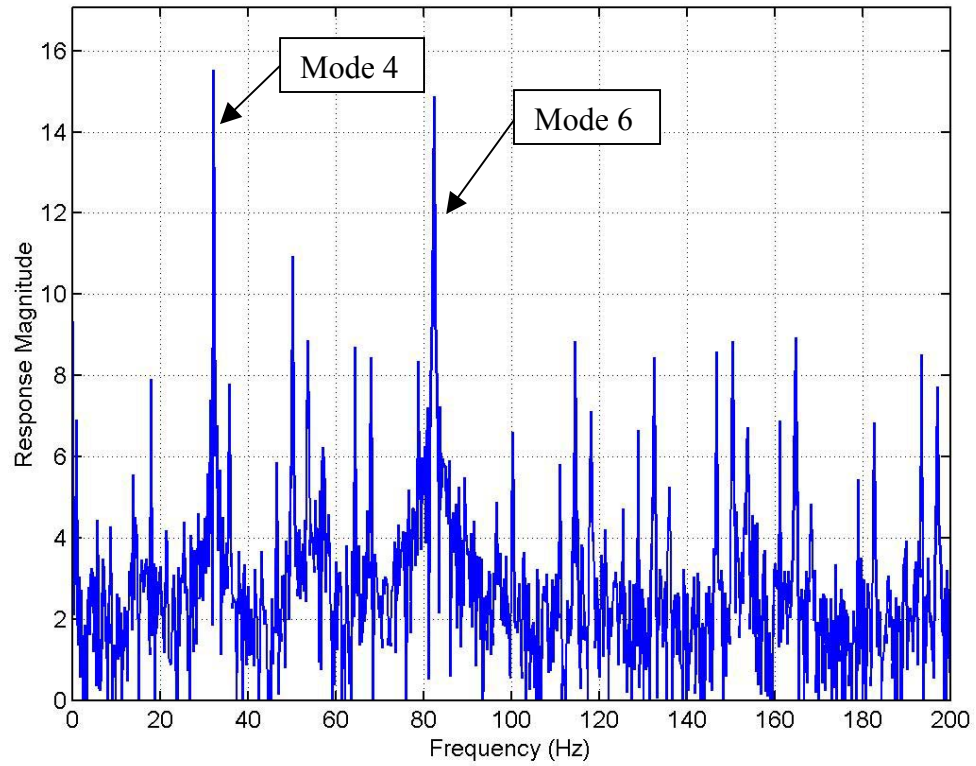
Figure B.5: FFT plot for sensor #1 (mode 6 excitation)

The FFT response for sensor #1 shows multiple peaks at many modes including mode 1 (~ 1 Hz), mode 3 (~ 17 Hz), mode 4 (~ 33 Hz), and mode 6 (~82 Hz). These influences are expected based on the strain data shown in Figure B.4. Figure B.6 and Figure B.7 show similar results for the FFT responses of sensor #6 and sensor #7, respectively.
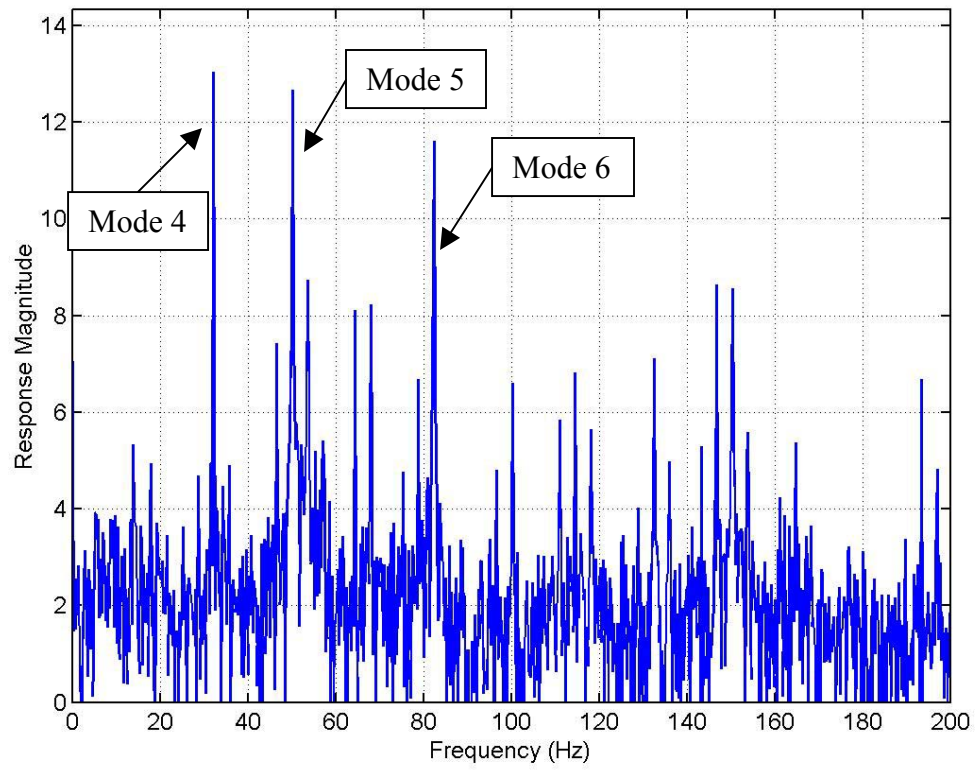
Figure B.6: FFT plot for sensor #6 (mode 6 excitation)
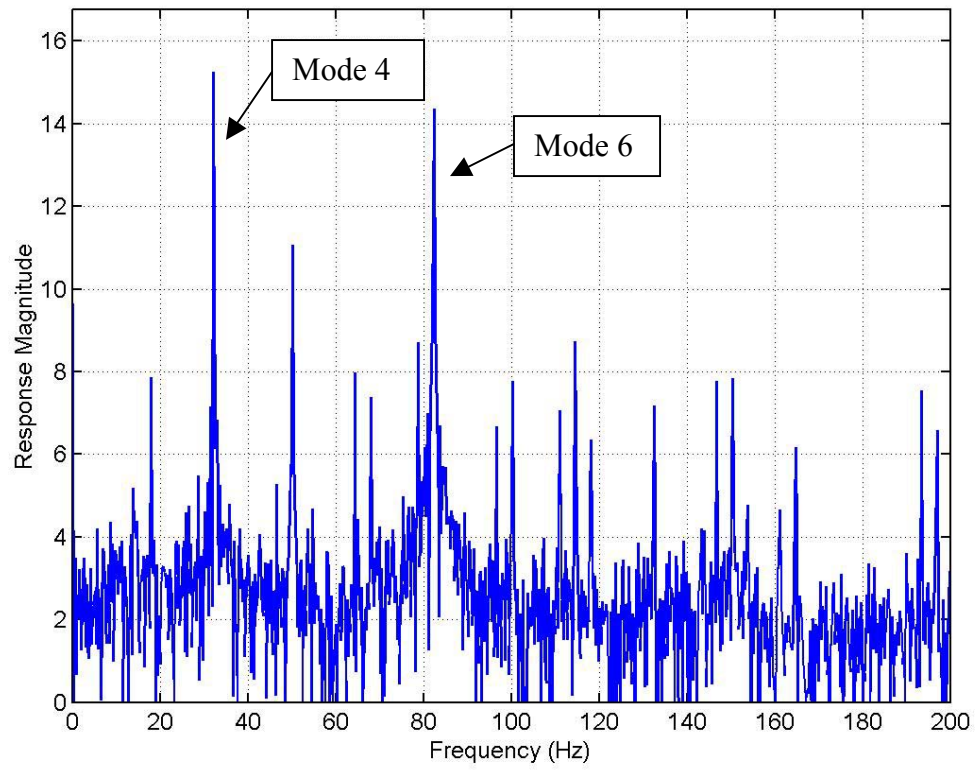
Figure B.7: FFT plot for sensor #7 (mode 6 excitation)

**B.2 Mode 7 Testing: Excitation Frequency Close to the Seventh Natural Frequency**
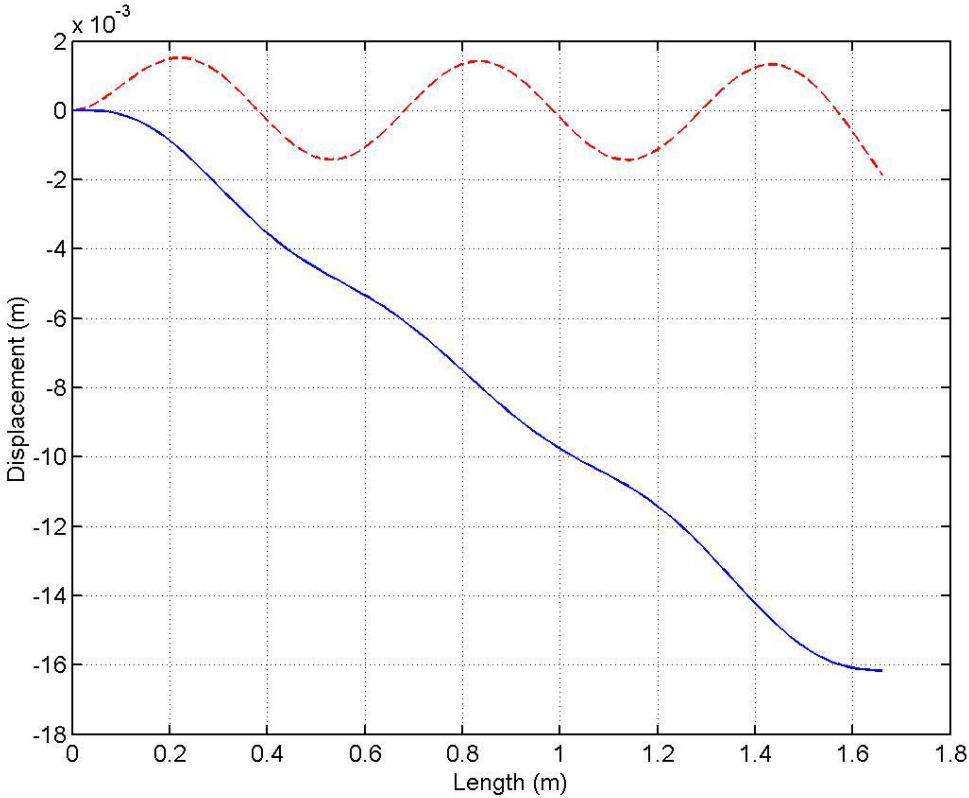
Figure B.8: Mode 7 reference mode shape (--) and experimental shape (—) at a

maximum deflection point

Figure B.8 displays the comparison between the reference mode 7 shape and the experimentally determined shape. It is difficult to tell, but the experimentally determined shape has the characteristics of a mode 7 shape based on the number of deflection points, but obviously does not follow the reference shape. From near the root location of the beam, the experimental shape proceeds to the negative direction away from the theoretical shape. This will be shown to be a result of an inadequate sensor spacing, and not extraneous modes as displayed for the other shape results.
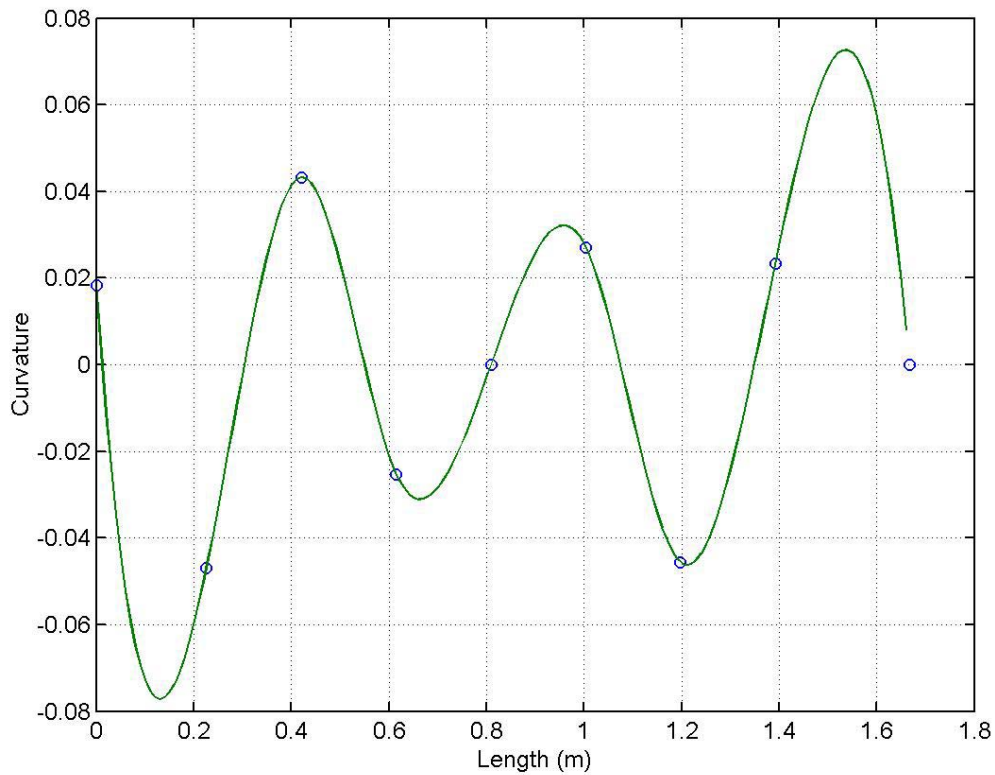
Figure B.9: Mode 7 curvature data and positions of FBG sensors

The curvature data obtained for the mode 7 test is displayed in Figure B.9. This data does show a good representation of mode 7 with six inflection points. The interpolation of the curvature values between the "root" sensor and sensor #2 drops to excessively low negative values. A similar case is observed between sensor #8 and the beam tip, with the curvature values going to higher values. These effects are because of the sensor spacing (and lack of an adequate number of sensors). The eight sensors used on the beam could provide a better shape measurement if they were located in positions to provide better interpolations around the maximum curvature values.

176
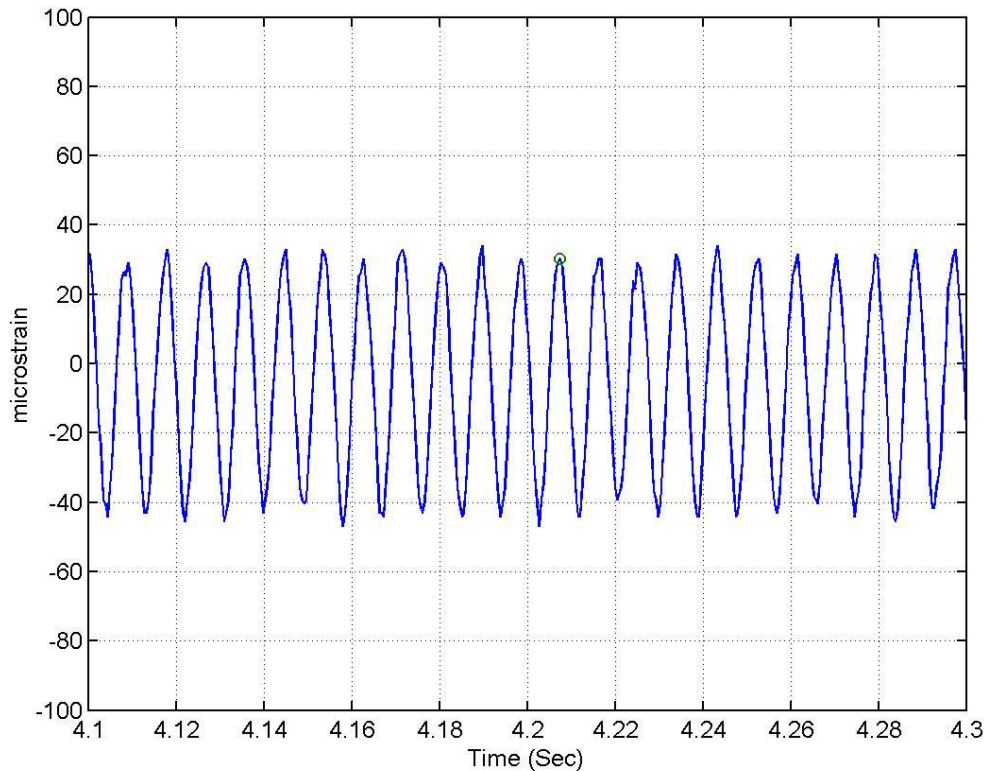
Figure B.10: Time trace for a FBG sensor during the mode 7 excitation

The strain data for sensor #1 during the mode 7 test is shown in Figure B.10. This data displays some lower frequency variation in the amplitude of the peaks. The sensor response is much improved over the mode 6 data presented in the previous section. The amplitude of the excitation was reduced in order to prevent extraneous vibrations in the beam, hence the reduced strain amplitudes and "cleaner" FFT response graphs below.

The FFT responses shown in Figure B.11 through Figure B.13 are for the sensor #1, #3, and #7, respectively. Each of these graphs displays a response peak near 115 Hz

corresponding to the mode 7 resonant frequency. No other modes appear as compared to the other test data. As stated earlier the difference between the experimental shape data and the theoretical shape data is the use of insufficient sensor spacing on the cantilever beam for this vibration state.
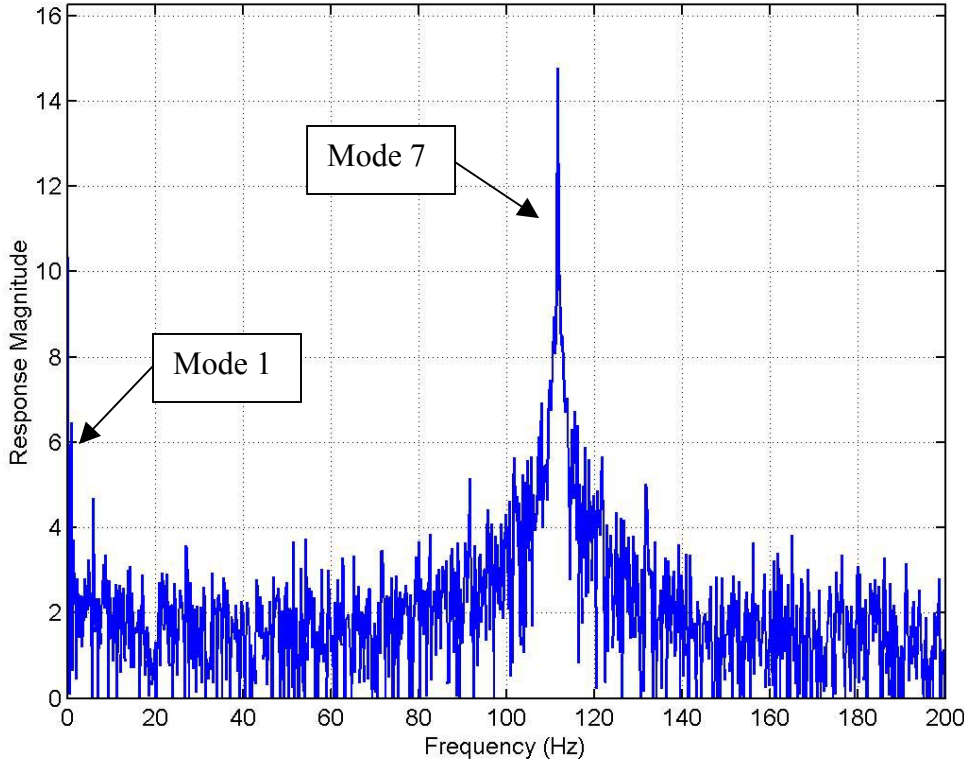

Figure B.11: FFT plot for sensor #1 (mode 7 excitation)
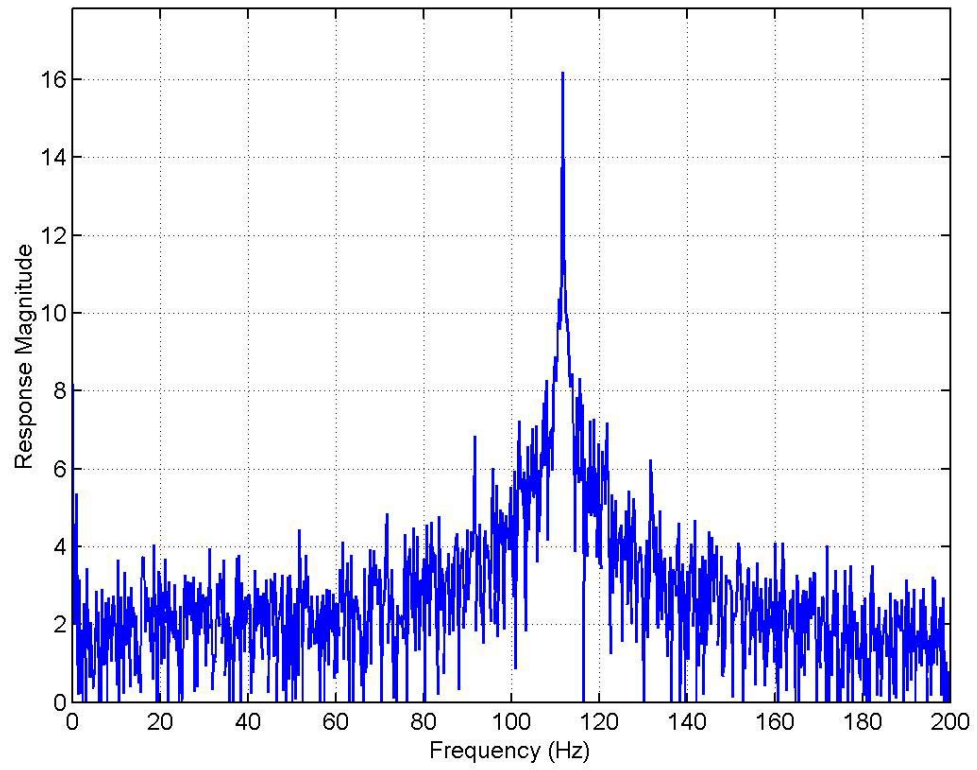
Figure B.12: FFT plot for sensor #3 (mode 7 excitation)
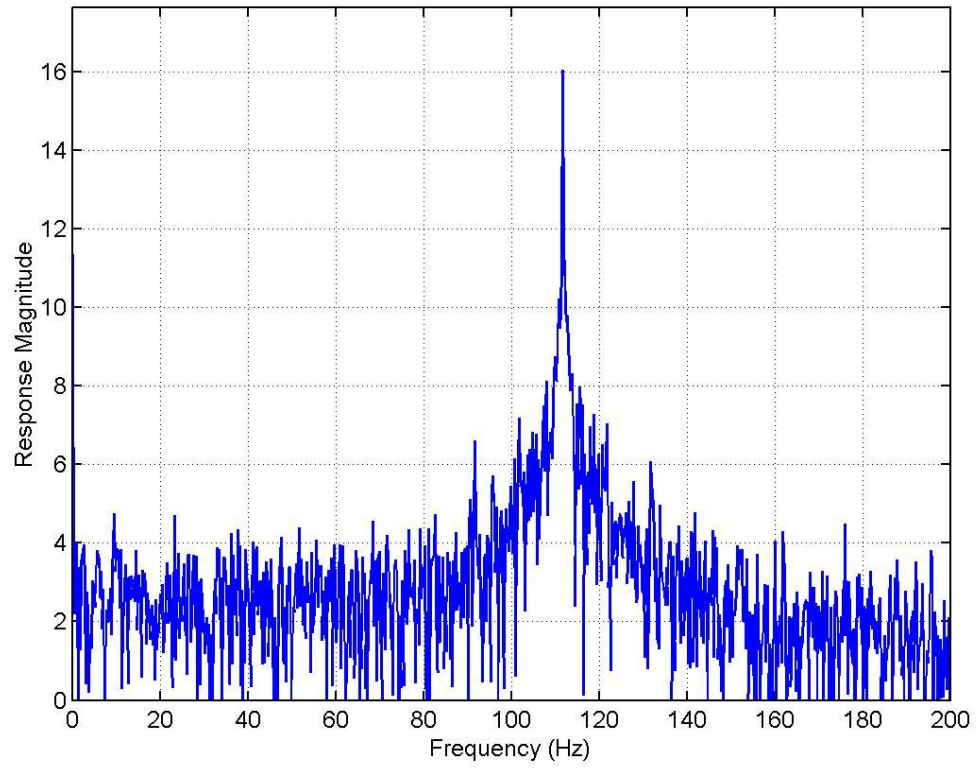
Figure B.13: FFT plot for sensor #7 (mode 7 excitation)

References

Aikimo, M., T. Vaarala, and H. Keranen, "Intelligent Prism-Grating-Prism Spectrograph for Multipoint Fiber Optic Remote Spectroscopy", Proceedings 12th International Conference on Optical Fiber Sensors, pp. 552-555, 1997.

Austin, F., M. Rossi, W. Van Nostrad, G. Knowles, and A. Jameson, "Static Shape Control for Adaptive Wings," AIAA Journal, Volume 32, No. 9, pp. 1895-1901, 1994.

Balachandran, B., A. Sampath, and J. Park, "Active control of interior noise in a three-dimensional enclosure," Smart Materials and Structures, Volume 5, pp. 89-97, February 1996.

Baldwin, C., T. Salter, and J. Kiddy, "Static shape measurements using a multiplexed fiber Bragg grating sensor system." To be published in Proceedings: Smart Structures and Materials: Smart Sensor Technology and Measurement Systems, March 2004.

Baldwin, C., T. Salter, J. Niemczuk, P. Chen, and J. Kiddy, "Structural monitoring of composite marine piles using multiplexed fiber Bragg grating sensors: In-field applications," Proceedings: Smart Structures and Materials: Smart Systems for Bridges, Structures, and Highways, Vol. 4696, pp. 82-91, March 2002.(a)

Baldwin, C, J. Niemczuk, J. Kiddy, P. Chen, M. Christiansen, and S. Chen, "Structural testing of Navy vessels using Bragg gratings and a prototype Digital Spatial Wavelength Domain Multiplexing (DSWDM) system," Naval Engineers Journal, American Society of Naval Engineers, Vol. 114, No. 1, pp. 63-70, 2002.(b)

Baldwin, C., P. Chen, J. Kiddy, J. Niemczuk, M. Christiansen, K. Vaithyanathan, and S. Chen, "Structural testing of an LPD-17 propulsion propeller using Bragg gratings and Digital Spatial Wavelength Domain Multiplexing (DSWDM)," Proceedings: Smart Structures and Materials: Industrial and Commercial Applications of Smart Structures Technologies, Vol. 4332, pp. 124-132, March 2001.(a)

Baldwin, C., T. Poloso, P. Chen, J. Niemczuk, J. Kiddy, and C. Ealy, "Structural monitoring of composite marine piles using fiber optic sensors," Proceedings: Smart Structures and Materials: Smart Systems for Bridges, Structures, and Highways, Vol. 4330, pp. 487-497, March 2001.(b)

Baldwin, C. Ratiometric demodulation of short and long period Bragg grating sensors, Masters Thesis, University of Maryland, College Park, 1996.

Beer, F. and E. Johnston, Mechanics of Materials, McGraw-Hill, New York, 1981.

Behbahani-Nejad, M. and N. Perkins, "Harmonically forced wave propagation in elastic cables with small curvature," ASME Journal of Vibration and Acoustics, Vol. 119, No. 3, pp. 390-397, 1997.

Blue Road, "High Speed Detector, HSD 002," Product Catalog, www.bluerr.com/hsd.htm, 2001.

Bramwell, A.R.S., Helicopter Dynamics. Edward Arnold Ltd. Victoria, 1986.

Chen, P. and J. Sirkis, "Method and Apparatus for Determining the Shape of a Flexible Body," United States Patent, No. 6,256,090 B1, July 2001.

Chen, S. and Y. Hu, "Large-Scale High-Speed Multiplexed Optical Fiber Sensor Network," United States Patent, No. 6492636, December 2002.

Christiansen, M., S. Chen, C. Baldwin, J. Niemczuk, J. Kiddy, P. Chen, H. Kopola, M. Aikio, P. Suopajarvi, and S. Buckley, "Digital spatial wavelength domain multiplexing (DSWDM) using a prism-grating-prism (PGP) and a CMOS imager: implementation and initial testing," Proceedings: Smart Structures and Materials: Sensory Phenomena and Measurement Instrumentation for Smart Structures and Materials, Vol. 4328, pp. 88-95, March 2001.

Davis, M. A., A. Kersey, J. Sirkis, and E. Frieble, "Shape and vibration mode sensing using a fiber optic Bragg grating array," Smart Materials and Structures Journal, Vol. 5, No. 6, pp. 759-765, December 1996.

Excel 97, *Help Topics*, Microsoft, 1997.

Foedinger, R., D. Rea, J. Sirkis, C. Baldwin, J. Troll, R. Grande, C. Davis, and T. VanDiver, "Embedded fiber optic sensor arrays for structural health monitoring of filament wound composite pressure vessels," Proceedings: Smart Structures and Materials: Sensory Phenomena and Measurement Instrumentation for Smart Structures and Materials, SPIE Vol. 3670, pp. 289-301; 1999.

Gray, D., B. Anderson, and R. Bitmead, "Towed Array Shape Estimation Using Kalman Filters – Theoretical Models." IEEE Journal of Oceanic Engineering, Volume 8, No. 4, pp. 543-556, October 1993.

Greene, J., K. Murphy, B. Fogg, R. Claus, and A. Vengsarkar, "Optical fiber, vibration-mode filters incorporating photoinduced refractive-index gratings." Smart Materials and Structures, Volume 1, pp. 243-249, 1992.

Haaslach, H. and J. Sirkis, "Interferometric strain measurement by arbitrarily configured, surface mounted, optical fibers," Journal of Lightwave Technolofy, Vol. 8, pp. 1497-1503, October 1990.

Hill, K., Y. Fujii, D. Johnson, and B. Kawasaki, "Photosensitivity in optical waveguides: Application to reflection filter fabrication," Applied Physics Letters, Volume 32, No. 10, pp. 647, 1978.

Hill, K., B. Malo, F. Bilodeau, D. Johnson, and J. Albert, "Bragg gratings fabricated in monomode photosensitive optical fiber by UV exposure through a phase mask," Applied Physics Letters, Volume 62, pp. 1035-1037, 1993.

Howard, B. and J. Syck, "Calculation of the Shape of a Towed Underwater Acoustic Array." IEEE Journal of Oceanic Engineering, Vol. 17, No. 2, April 1992.

James, M., G. Smith, J. Wolford, and P. Whaley, Vibration of Mechanical and Structural Systems, Harper Colins, New York, 1994.

Kashyap, R., Fiber Bragg Gratings, Academic Press, San Diego, 1999.

Kiddy, J., C. Baldwin, T. Salter, and P. Chen, "Structural load monitoring of RV Triton using Fiber Optic Sensors," Proceedings: Smart Structures and Materials: Industrial and Commercial Applications of Smart Structures Technologies, Vol. 4698, pp. 462-472, March 2002.

Li, Y., Spatially weighted fiber-optic sensors for vibration modal filters, Ph.D. Dissertation, University of Maryland, College Park, 1998.

Luo, F., J. Liu, and S. Chen, "Fiber optic distributed sensing scheme for monitoring structural strain and deformation," Optical Engineering, Vol. 36, No. 5, pp. 1548-1551, May 1997.

MATLAB, Using MATLAB, Version 6, The Mathworks, Inc., 2000.

Micron Optics, Inc., "Fiber Bragg Grating Interrogation System," Product Catalog, www.micronoptics.com, 2001.

Measures, R., Structural Monitoring with Fiber Optic Technology, Academic Press, San Diego, 2001.

Melle, S., K. Liu, and R. Measures, "A passive wavelength demodulation system for guided-wave Bragg grating sensors," IEEE Photonics Technology Letters, Volume 4, pp. 516-518, May 1992.

Melle, S., K. Liu, and R. Measures, "Practical fiber-optic Bragg grating strain gauge system," Applied Optics, Volume 32, pp. 3601-3609, July 1993.

Meltz, G., W. Morey, and W. Glenn, "Formation of Bragg gratings in optical fibers by a transverse holographic method," Optics Letters, Volume 14, pp. 823-825, August 1989.

Nikitakkos, N., A. Leros, and S. Katsikas, "Towed Array Shape Estimation Using Multimodel Partitioning Filters," IEEE Journal of Oceanic Engineering, Volume 23, No. 4, October 1998.

Othonos, A. and K. Kyriacos, <u>Fiber Bragg Gratings, Fundamentals and Applications in Telecommunications and Sensing,</u> Artech House, Boston, 1999.

Pandey, A., M. Biswas, and M. Samman, "Damage Detection from Changes in Curvature Mode Shapes," Journal of Sound and Vibration, Vol. 145, No. 2, pp. 321-332, 1991.

Reich, G. and B. Sanders, "Structural shape sensing for morphing aircraft," Proceedings, Smart Structures and Materials, Smart Structures and Integrated Systems, Volume 5056, pp. 134-141, March 2003.

Sampath, A. and B. Balachandran, "Studies on performance functions for interior noise control," Smart Materials and Structures, Volume 6, pp. 315-332, June 1997.

Sevenhuijsen, P., J. Sirkis, and F. Bremand, "Current Trends in Obtaining Deformation Data from Grids," Experimental Techniques, Vol. 17, No. 3, pp. 22-26, May 1993.

Sivanesan, P. <u>Optical fiber sensor for simultaneous measurement of distributed strain and temperature</u>, Ph.D. Dissertation, University of Maryland, College Park, 2002.

Smith, J., Y. Leung, and A. Cantoni, "The Cramer-Rao Lower Bound for Towed Array Shape Estimation with a Single Source," IEEE Transactions on Signal Processing, Volume 44, No. 4, pp. 1033-1036, April 1996.

Snyder, A. and J Love, Optical Waveguide Theory, Chapman & Hall, New York, 1983.

Thomas, G. and R. Finney, Calculus and Analytic Geometry, 8th ed., Addison-Wesley, Reading, 1992.

Udd, E., ed., Fiber Optic Smart Structures. John Wiley & Sons, 1995.

Ventsel, E., Thin plates and shells: theory, analysis, and applications, Marcel Dekker, New York, 2001.

Wahl, D. E., "Towed Array Shape Estimation Using Frequency-Wavenumber Data," IEEE Journal of Oceanic Engineering, Volume 18, No. 4, October 1993.

Wang, G., G. Havsgard, E. Urnes, K. Pran, S. Knudsen, A. Kersey, M. Davis, T. Berkoff, A. Dandridge, and R. Jones, "Digital demodulation and signal processing applied to fiber Bragg grating strain sensor arrays in monitoring transient loading effects on ship hulls," 12th International Conference on Optical Fiber Sensors, OSA 1997 Technical Digest Series Vol. 16, pp. 612- 615, October 1997.

Yu, M. and B. Balachandran, "Acoustic measurements using a fiber optic sensor system," Journal of Intelligent Material Systems and Structures, Vol. 7, No. 14, pp. 409-414, 2003.

Yu, M., <u>Fiber optic sensor systems for acoustic measurements</u>, Ph.D. Dissertation, Department of Mechanical Engineering, University of Maryland, College Park, MD, 2002.